Lappeenrannan teknillinen yliopisto
Lappeenranta University of Technology

Teemu Turunen-Saaresti

COMPUTATIONAL AND EXPERIMENTAL ANALYSIS OF FLOW FIELD IN THE DIFFUSERS OF CENTRIFUGAL COMPRESSORS

Thesis for the degree of Doctor of Science (Technology) to be presented with due permission for public examination and criticism in the Auditorium of the Student Union House at Lappeenranta University of Technology, Lappeenranta, Finland on the 26th of November, 2004, at noon.

Acta Universitatis
Lappeenrantaensis
192

ISBN 951-764-962-2
ISBN 951-744-969-X (PDF)
ISSN 1456-4491

Lappeenrannan teknillinen yliopisto
Digipaino 2004

Suville ja tytöille

Abstract

Teemu Turunen-Saaresti
Computational and Experimental Analysis of Flow Field in the Diffusers of Centrifugal Compressor
Lappeenranta 2004
103 p.
Acta Universitatis Lappeenrantaensis 192
Diss. Lappeenranta University of Technology
ISBN 951-764-962-2, ISBN 951-744-969-X (PDF), ISSN 1456-4491

Centrifugal compressors are widely used for example in process industry, oil and gas industry, in small gas turbines and turbochargers. In order to achieve lower consumption of energy and operation costs the efficiency of the compressor needs to be improve.

In the present work different pinches and low solidity vaned diffusers were utilized in order to improve the efficiency of a medium size centrifugal compressor. In this study, pinch means the decrement of the diffuser flow passage height. First different geometries were analyzed using computational fluid dynamics. The flow solver Finflo was used to solve the flow field. Finflo is a Navier-Stokes solver. The solver is capable to solve compressible, incompressible, steady and unsteady flow fields. Chien's $k-\epsilon$ turbulence model was used.

One of the numerically investigated pinched diffuser and one low solidity vaned diffuser were studied experimentally. The overall performance of the compressor and the static pressure distribution before and after the diffuser were measured. The flow entering and leaving the diffuser was measured using a three-hole Cobra-probe and Kiel-probes.

The pinch and the low solidity vaned diffuser increased the efficiency of the compressor. Highest isentropic efficiency increment obtained was 3% of the design isentropic efficiency of the original geometry. It was noticed in the numerical results that the pinch made to the hub and the shroud wall was most beneficial to the operation of the compressor. Also the pinch made to the hub was better than the pinch made to the shroud. The pinch did not affect the operation range of the compressor, but the low solidity vaned diffuser slightly decreased the operation range.

The unsteady phenomena in the vaneless diffuser were studied experimentally and numerically. The unsteady static pressure was measured at the diffuser inlet and outlet, and time-accurate numerical simulation was conducted. The unsteady static pressure showed that most of the pressure variations lay at the passing frequency of every second blade. The pressure variations did not vanish in the dif-

fuser and were visible at the diffuser outlet.

Keywords: centrifugal compressor, diffuser, computational fluid dynamics, low solidity vane, pinch

UDC 533.6.011 : 519.6 : 621.45.037

Acknowledgements

I would like to express my sincere thanks to professor Jaakko Larjola my supervisor and leader of high speed technology research group for his interest to my research work.

I would also like to thank all team members of high speed technology research group. Especially comments and expertise of Dr. Arttu Reunanen have been for great assistance. I also want to thank Dr. Jari Backman. The laboratory staff, Petri Pesonen, Jouni Ryhänen and Erkki Nikku need to be mentioned (they insisted). The experimental work would be far more difficult without their assistance.

I express my sincere thanks for the reviewers professor Abraham Engeda of Michigan State University and Dr. Andrew R. Martin of Kunliga Tekniska Högskolan, for their valuable comments. They greatly helped me to improve the quality of this work.

The financial support of High Speed Tech Ltd, the National Technology Agency (TEKES), South Carelia regional fund of the Finnish Cultural Foundation and the Research Foundation of the Lappeenranta University of Technology is gratefully acknowledged. The computational resources for the numerical work have been provided by CSC-Scientific Computing Ltd.

I owe the dearest thanks to my wife Suvi and our daughters Sointu and Linnea for their loving support. They gave me a sense of proportion during the research work and they drifted my thoughts away from the scientific world when I most needed it.

Lappeenranta, November 2004

Teemu Turunen-Saaresti

Contents

Nomenclature

Upper case

A	area, m^2
C_μ	coefficient in the $k-\epsilon$ turbulence model
C_1	coefficient in the $k-\epsilon$ turbulence model
C_2	coefficient in the $k-\epsilon$ turbulence model
C_{pr}	static pressure rise coefficient
E	total energy per volume, J/m^3
F, G, H	flux vectors in x-, y- and z-directions
K_p	total pressure loss coefficient
N	rotational speed, $1/\mathrm{s}$
N	number of vanes
N_s	specific speed
P	production of kinetic energy of turbulence per volume, W/m^3
Q	source term vector
R	specific gas constant, $\mathrm{J}/(\mathrm{kg}\cdot\mathrm{K})$
R_H	humidity, %
S	area of cell face , m^2
T	temperature, K
T	rotation matrix
T_u	turbulence intensity
U	vector of conservative variables
V	volume, m^3
$\vec{V}$	velocity vector

Lower case

b	diffuser height, m
c	absolute velocity, m/s
c_p	specific heat capacity in constant pressure, $\mathrm{J}/(\mathrm{kg}\cdot\mathrm{K})$
c_v	specific heat capacity in constant volume, $\mathrm{J}/(\mathrm{kg}\cdot\mathrm{K})$
d	diameter, m
e	specific internal energy, J/kg
h	specific enthalpy, J/kg
i	incidence angle, $^\circ$
k	kinetic energy of turbulence, J/kg
l	length, m
$\vec{n}$	unit normal vector
p	pressure, Pa
q_i	heat flux in i direction, kg/s

q_m	mass flow rate, $\mathrm{kg/s}$
q_v	volume flow rate, $\mathrm{m^3/s}$
r	radius, m
s	specific entropy, $\mathrm{J/(kgK)}$
t	time, s
u_τ	friction velocity, $\mathrm{m/s}$
u, v, w	velocity components in x-, y- and z-directions, $\mathrm{m/s}$
u_i	velocity component in i-direction, $\mathrm{m/s}$
x, y, z	Cartesian co-ordinates
y_n	normal distance from the wall, m
y^+	non-dimensional normal distance from the wall

Greek letters

α	absolute flow angle measured from radial direction, $^\circ$
γ	ratio of specific heats
δ	Kronecker's delta function
ϵ	dissipation of the kinetic energy of turbulence, $\mathrm{W/kg}$
$\tilde{\epsilon}$	dissipation of the kinetic energy of turbulence in Chien's model, $\mathrm{W/kg}$
η	efficiency
θ	turning angle of the diffuser vanes, $^\circ$
μ	dynamic viscosity, $\mathrm{kg/(ms)}$
μ_T	turbulent viscosity, $\mathrm{kg/(ms)}$
μ_k	diffusion coefficient of k, $\mathrm{kg/(ms)}$
μ_ϵ	diffusion coefficient of ϵ, $\mathrm{kg/(ms)}$
π	pressure ratio
π	ratio of circumference and diameter of a circle $\pi \approx 3.14$
ρ	density, $\mathrm{kg/m^3}$
σ	solidity
σ_k	coefficient in the $k-\epsilon$ turbulence model
σ_ϵ	coefficient in the $k-\epsilon$ turbulence model
τ	shear stress, $\mathrm{N/m^2}$
Ω	angular velocity, $\mathrm{rad/s}$

Subscripts

1	compressor inlet
2	rotor outlet / diffuser inlet
2'	leading edge of the diffuser vanes
3	trailing edge of the diffuser vanes
4	diffuser outlet
5	compressor outlet
i	index

i, j, k	grid co-ordinate directions
ij	ij-component of a matrix
in	inlet
k	kinetic energy of turbulence
n	component normal to the surface
out	outlet
r	radial component
ref	reference state
s	isentropic
sensor	distance sensor
T	turbulent
t	total state
t	tangential component
t-t	total to total
w	wall
v	viscous
x, y, z	direction of the x-, y- and z-axes
ϵ	dissipation of the kinetic energy of turbulence

Superscript

^	convective value
”	fluctuating component
$\bar{}$	averaged quantity
$\vec{}$	vector

Abbreviations

ASME	The American Society of Mechanical Engineers
CFD	computational fluid dynamics
CTA	constant temperature anemometry
DDADI	diagonally dominant alternating direction implicit
des	design operation point
DIN	Deutsches Institut für Normung e.V.
DNS	direct numerical method
FVM	finite volume method
HUT	Helsinki University of Technology
ISA	International Federation of the National Stardardizing Associations
ISO	International Standardization Organization
LES	large eddy simulation
LUT	Lappeenranta University of Technology
LSVD	low solidity vaned diffuser
MUSCL	monotone upwind schemes for conservation laws
PC	personal computer
RANS	Reynolds-averaged Navier-Stokes
VDI	Verein Deutscher Ingenieure

1 Introduction

A centrifugal compressor pressurizes gas continuously to higher pressure. It is used for example in process industry, refrigeration plants, in small gas turbines, turbochargers and oil and gas industry, where the use of pressurized gas is needed. Centrifugal compressors provide more pressure rise per stage than axial compressors. Therefore, centrifugal compressors are a better option if a small number of stages is required. It is easy to obtain a pressure ratio up to four per stage with a centrifugal compressor. In axial compressors the pressure ratio per stage is usually below 1.2. Also the lower cost of a centrifugal compressor than multistage axial compressor is an advantage when the size of the machine is small enough. In larger applications (usually over 10 MW) the axial compressor has better efficiency, and it is used in e.g. larger gas turbines.

A centrifugal compressor consists of two parts, an impeller and a diffuser. In addition, the diffuser may follow a volute or a collecting chamber, which leads pressurized fluid to the pipe system. The energy is transferred to the fluid in the impeller, and the fluid leaving the impeller contains a high amount of kinetic energy, approximately 30% - 40% of the total work input. To achieve a good efficiency it is necessary to convert as much as possible of this kinetic energy into static pressure rise. However, the flow leaving the impeller is highly three-dimensional and complex, and therefore the maximum pressure rise achieved in a centrifugal compressor diffuser is lower than that achieved in an axial diffuser.

To convert the kinetic energy to static pressure rise, two different methods can be used:

1. Increasing the flow area, which reduces the velocity and increases the static pressure

2. Changing the mean flow path radius, which decreases the tangential velocity and increase the static pressure

One or both these methods are used in the diffuser of a centrifugal compressor. The diffusers of centrifugal compressors can be of two different types, vaneless and vaned. Vaned diffusers can be further divided into different classes based on the vane geometry and solidity. Vaneless diffusers are used when large operation range and inexpensive design are primary goals. This type of diffuser is usually used in process, refrigeration and turbocharger compressors. The vaned diffuser achieves a better pressure rise and efficiency than the vaneless diffuser. On the other hand, the vaned diffuser has a narrower operation range and more complex geometry, which leads to a more expensive design. Vaned diffusers are used in high pressure ratio stages, where it is not reasonable to use a vaneless diffuser, large turbochargers and gas turbine compressors.

In this study two industrial one-stage centrifugal compressors are studied numerically and experimentally. Computational fluid dynamics (CFD) is used to investigate the effect of the pinch in the diffuser and the effect of the low solidity vaned diffuser (LSVD). The effect of the pinch made to the hub wall or shroud wall, and both walls is studied. In this study, the pinch means the decrement of the diffuser flow passage height. The effect of the vane shape and the vane number in a low solidity vaned diffuser is investigated. In addition, time-accurate, fully-viscous, three dimensional computation is performed to investigate unsteady effect in the vaneless diffuser.

One of the pinched and one of the low solidity vaned diffusers are also investigated experimentally. The results are compared to the results of the vaneless diffuser. The static pressures are measured at the inlet and outlet at four different circumferential positions, and in addition, in one circumferential position three different radius ratios between the inlet and the outlet are measured. The total pressure and temperature are measured using Kiel-probes with thermocouples at the inlet and outlet in four different circumferential positions. Also the flow angle is measured with a three-hole Cobra-probe in one circumferential position at the inlet and the outlet. In addition, the unsteady static pressure is measured to study the flow field further and to validate the computational results.

The objectives of this study are:

1. To achieve further understanding on the effect of different kinds of pinches
2. To achieve information on the effect of different kinds of vane shapes in low solidity vaned diffuser
3. To achieve further knowledge on unsteady phenomena in the vaneless diffuser
4. To improve the efficiency of the centrifugal compressor

The diffusers of centrifugal compressors have been studied for many decades, and comprehensive literature on the design and construction of different kinds of diffusers is available. The contribution of this work to current knowledge is the comprehensive study of different kind of pinches and low solidity vaned diffusers. The time-accurate numerical investigation of the whole compressor gives additional value to the study.

This work consists of three parts, a literature survey, a numerical study and an experimental study. The literature survey is presented in chapter 2. Chapters 3 and 4 describe the used numerical methods and numerical results. Also some of the experimental results are presented in order to verify the numerical results. However, the experimental setup and results are discussed in detail in chapters 5 and 6.

2 Diffuser of a centrifugal compressor

2.1 Introduction

In a centrifugal compressor the fluid first enters the impeller. The energy is transferred to the process in the impeller. A complicated flow field will develop in the impeller and strong fluctuations in the velocity and flow angle can be seen at the circumferential and axial direction (Dean and Senoo 1960, Eckardt 1975, Krain 1980; 1988). A jet-wake (or primary and secondary) flow pattern exist at the outlet of the impeller. The wake (secondary) flow position is at the suction surface or at the shroud depending on the flow rate and the impeller geometry. The flow field entering the diffuser is unsteady and distorted, and it has a significant amount of kinetic energy to transfer to the static pressure. The pressure non-uniformity caused by the volute at the off-design condition further influences the flow field in the diffuser (Fatsis et al. 1997, Sorokes et al. 1998, Hillewaert and Van den Braembussche 1999). The diffuser is between two components which influence the flow field in it, and therefore the diffuser has a major task in matching different parts of the compressor together. Poor design of the diffuser can have a bad effect on the overall efficiency of the compressor. Therefore it is important for the designer to know the effect of the different parameters to the operation of the compressor to be able to design a compressor with good performance.

The diffusers of centrifugal compressors can be divided to two classes: vaneless and vaned diffusers (see figure 1). Vaneless diffusers have a wider flow range but lower pressure recovery and efficiency, whereas vaned diffusers have higher pressure recovery and efficiency, but narrower flow range.

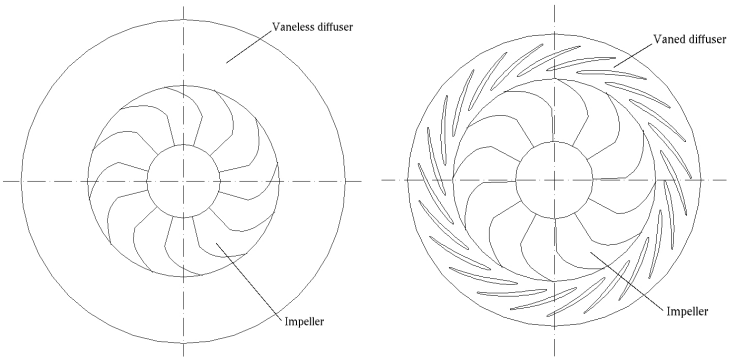

Figure 1: Vaneless and vaned diffusers.

2.2 Vaneless diffuser

2.2.1 Geometry of the vaneless diffuser

The geometry of the vaneless diffuser is very simple. It consists of parallel or almost parallel walls which form a radial annular passage from the impeller outlet radius to some outlet radius of the diffuser. The diffuser is usually followed by a volute or a collecting chamber which leads the flow to one single exit. The different inlets of the vaneless diffuser are shown in figure 2. A small pinch is usually used to stabilize the flow entering the diffuser. Ludtke (1983) has tested four types of vaneless diffusers, one with parallel walls, one highly tapered, one with constant area, and one with parallel walls but reduced width. The width was reduced 52.7% from the original width. The diffuser with the parallel walls showed best efficiency. The diffuser with the constant area diffuser has a slightly lower efficiency but the operation range was larger. The narrowed diffuser decreased the efficiency. The highly tapered diffuser showed improvement in surge margin but the efficiency was decreased. Yingkang and Sjolander (1987) have tested vaneless diffusers with various taper angles. They found that a small amount of wall convergence was beneficial and yielded better static pressure recovery at the intermediate flow rate than a parallel wall diffuser. The parallel wall diffuser showed better static pressure recovery at the high flow rate. Also Engeda (1995) has investigated the beneficial effect of the pinch on diffusion process. A streamline curvature code was used to predict the diffuser flow field. Liberti et al. (1996) have tested two vaneless diffusers with different widths. They found that a narrower diffuser showed better efficiency and total-total pressure ratio than a wider diffuser.

The walls of the vaneless diffuser are usually straight. Lee et al. (2001) have optimized the vaneless diffuser of the centrifugal compressor using the direct method of optimization (DMO). In their optimization method the height of the diffuser was altered by moving the shroud wall. The original geometry had a flat hub wall and a curved shroud which decreased the height of the diffuser when the radius ratio increased. The new optimized geometry had a minimum height at the middle of the diffuser passage. The optimized geometry was manufactured and tested. It showed 2-3% increase of efficiency at the design point and 1-5% increase of efficiency at the off-design point.

The flow path in the vaneless diffuser has the shape of a logarithmic spiral. The velocity vectors and flow path are shown in figure 3. The performance of the vaneless diffuser can be described in the simplest way by the following equations:

$$rc_t \approx constant \tag{1}$$

$$q_m = \rho c_r 2\pi r b \tag{2}$$

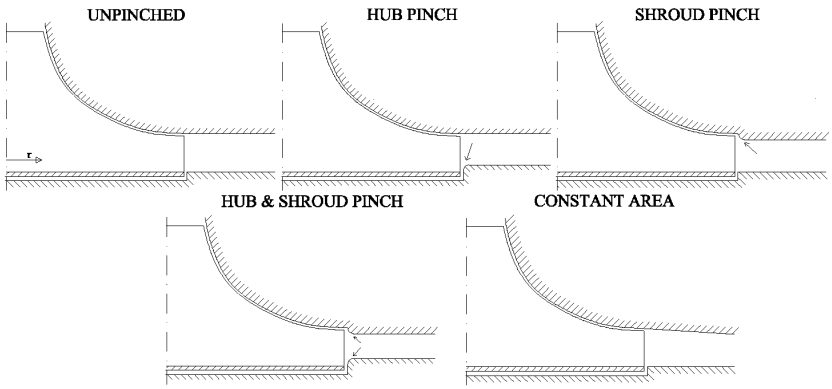

Figure 2: Vaneless diffuser inlet constructions.

$$\tan \alpha = \frac{c_t}{c_r} \tag{3}$$

where r is radius, c_t is tangential velocity, q_m is mass flow, c_r is radial velocity, b is the width of the diffuser and α is the flow angle from the radial direction. The above equations specify the conservation of the tangential momentum and continuity. It can be seen that the flow angle increases (from radial direction) when the radius of the diffuser increases. It can also be seen that the flow angle is approximately a function of the diffuser width b and the density of the fluid ρ. Stable operation of the diffuser requires that the flow angle at the diffuser outlet does not exceed $90°$. Many authors (e.g. Jansen 1964, Senoo and Kinoshita 1977 and Van den Braembussche et al. 1980) have studied the stability of the vaneless diffuser and the critical flow angle α_{2c} as a function of the diffuser width and the outlet radius. They have shown that the critical flow angle (from radial direction) is higher for the narrowed diffuser and lower for the increased outlet radius ratio.

2.2.2 Flow field in vaneless diffuser

Haupt et al. (1988) have measured unsteady static pressure at the inlet of the centrifugal compressor, at the impeller range, and at the diffuser radius ratios 1.225 and 1.825. Vaneless and vaned diffusers were used. The unsteady static pressure in the vaneless diffuser showed no pressure variations at the blade passage frequency at the radius ratio 1.225, but small variation was seen at the radius ratio 1.825. The results were obtained at low rotational speed and low flow rate.

Hathaway et al. (1993) have made a computational and experimental study of a NASA low-speed centrifugal compressor. The study focussed on the flow field in the impeller, but the mixing phenomena downstream of the impeller were

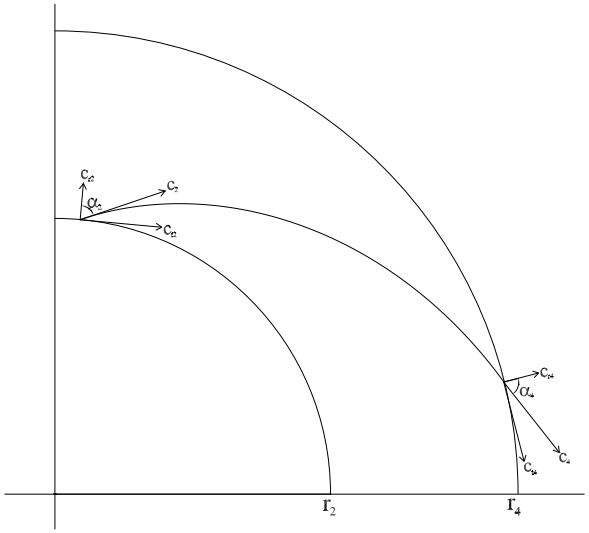

Figure 3: Velocity vectors and flow path in the vaneless diffuser.

also investigated. Laser anemometry measurements were made in the vaneless diffuser at radius ratios of 1.01, 1.02, 1.04 and 1.06. Flow angle variation at the circumferential direction was shown in the middle of the span and near the shroud wall. It was noticed that the viscous blade wake, which is clearly seen in the middle of the span and at radius ratios 1.01 and 1.02, decreased rapidly but was still visible at the radius ratio 1.06. The viscous blade wake was weaker near the shroud than in the middle of the span. A passage wake was also seen near the shroud. It was noticed that the passage wake mixed out more slowly than the blade wake. Calculated results about the mixing were not presented in the study.

Jin et al. (1994) have investigated unsteady static pressures in a vaneless and vaned diffuser of a centrifugal compressor during surge. The measurements were made at the radius ratios 1.23 and 1.83. Before the surge period, static pressure fluctuations were seen in the vaneless diffuser. Higher pressure at the pressure side of the impeller blade and lower pressure at the suction side of the impeller blade caused these fluctuations. The pressure fluctuations were attenuated in the diffuser but were still visible at the radius ratio 1.83.

Pinarbasi and Johnson (1994) have studied the flow field in a vaneless diffuser. In their compressor the impeller had 30° backswept blades, and the vaneless diffuser had straight walls and a constant cross-section area. Pinarbasi and Johnson used constant-temperature hot-wire anemometer (CTA) to measure radial, axial and tangential velocity components in the vaneless diffuser with different radius ratios. At the radius ratio $\frac{r}{r_2} = 1.02$ a passage wake was seen on the shroud wall and close to the pressure side. The blade wake was clearly seen at the suction side

of the blade. At the radius ratio $\frac{r}{r_2} = 1.08$ the blade wake was greatly diminished. The passage wake was carried along the shroud and it spread further along the shroud surface. The mixing out of this wake was not significantly visible. At the radius ratio $\frac{r}{r_2} = 1.15$ the blade wake was hardly visible, but the passage wake was moving along the shroud surface. The passage jet was moving slower than the passage wake. This was due to the flow angles of the jet and the wake. Measurements made further downstream showed that the variations in the circumferential direction were gradually mixed out and the passage wake spread out to the shroud surface. At the radius ratio $\frac{r}{r_2} = 1.02$ high turbulence kinetic energy was plotted in the area of the blade wake. In this area the value of the kinetic energy rapidly decreased at the radius ratio $\frac{r}{r_2} = 1.08$.

Pinarbasi and Johnson (1995) have also made CTA measurements in the vaneless diffuser of a centrifugal compressor. The Reynolds stress tensors were plotted at the off-design operation conditions 16% below and 11% above the design flow. It was found out that the blade and the passage wakes contained high levels of turbulent kinetic energy. These high kinetic energies contained high Reynolds stresses only in the blade wakes. Because of this the blade wakes mixed out quicker than the passage wakes. It was also found that the passage wake spread over a larger area of the shroud in the operation point below design point than the operation point above the design point at radius ratio 1.02.

Arnulfi et al. (1995) have done hot-wire anemometry measurements in the vaneless diffuser of a four-stage centrifugal blower. Eight different operation points were used, four of which were in stable operation conditions and the other four in unstable operation conditions. The rotational speed 3000 rpm was used in all operation conditions. The flow angle, velocities and Reynold stress components were measured. At the outlet of the first-stage impeller very uniform velocity and turbulence field were observed from hub to shroud. It was noticed that the relative velocity increased in the circumferential direction from the suction side to the pressure side. The flow angle of the relative velocity was smallest at the hub suction side corner, but the flow angle was higher elsewhere at the suction side, and decreased rapidly and remained quite constant over the blade passage but decreased again rapidly at the pressure side. The turbulence components remained quite constant and showed rather low values with high peaks at the blade area. At the outlet of the four-stage impeller the flow field was quite different. In the hub to shroud direction there was higher relative velocity, lower relative flow angle and higher turbulence components in the area near the hub. Relative velocity increased from the suction side to the pressure side and a lower relative velocity area could be seen in the suction side shroud corner. The absolute velocity and intensity of the velocity fluctuation were measured in the diffuser with various radius ratios in the middle of the diffuser passage. It could be seen that the velocity peaks from the blade passages were mixed away at the radius ratio 1.194. It could also be

seen that the mean velocity decreased and the intensity of the velocity fluctuations increased with increasing radius.

2.3 Vaned diffusers

2.3.1 Convectional vaned diffuser

Convectional vaned diffusers can be divided into two different categories on the basis of the vane type. The cascade diffuser consists of one or more rows of airfoil vanes. The channel diffuser is another type of convectional vaned diffuser. The cascade diffuser is shown in figure 4 on the left and the channel diffuser on the right.

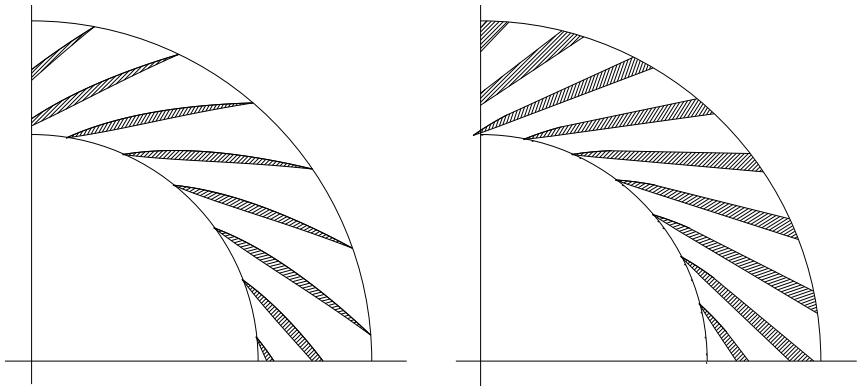

Figure 4: An example of a geometry of a cascade diffuser on the left and a channel diffuser on the right.

Both vaned diffuser types give better pressure recovery and efficiency than the vaneless diffuser, but the operation range is narrower that of the vaneless diffuser. Both types of vaned diffusers are used in centrifugal compressors and no clear indication of one being superior to the other exists.

2.3.2 Low solidity vaned diffuser

The low solidity vaned diffuser is a good compromise between the vaneless and the vaned diffuser. The low solidity vaned diffuser (LSVD) has a better peak efficiency than the vaneless diffuser and a wider flow range than the vaned diffuser. In the LSVD there are less and smaller vanes than in the vaned diffuser. The LSVD is shown in figure. 5. The distance between the vanes in the LSVD is large and no throat appears, which extends the flow range at a high flow rate. The incidence of the vanes is designed to be negative to get as good operation range as

possible also at a low flow rate. The geometry of the LSVD is mainly defined by the following parameters:

- Inlet radius of the vane
- Vane inlet angle
- Solidity
- Number of vanes
- Turning angle

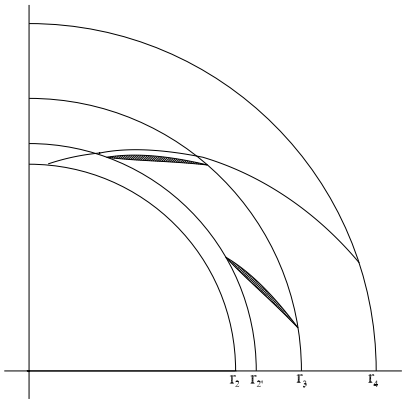

Figure 5: Layout of the LSVD and flow path in it.

In a study by Senoo et al. (1983) two types of low solidity vaned diffuser were designed, one with a single cascade row and the other with tamdem cascade rows, and installed in a centrifugal blower. The geometry of the vane was adopted from U.S.A.35-B airfoil shape and it was conformally mapped into a circular cascade. The single cascade LSVDs were designed with solidity 0.69 and 11 blades. The stagger angles 70° and 68° were used. Also solidity 0.83 was tested. It was achieved by increasing the blade number from 11 to 13. The stagger angle 68° was used in the case of solidity 0.83. In the case of the tamdem cascade LSVD front cascade was designed with solidity 0.35 and the rear cascade with solidity 0.63. Three different tamdem cascade low solidity vaned diffusers were tested, one with front cascade stagger angle 70° and rear cascade stagger angle 64°, one with the same front blades as the previous design and rear cascade with stagger angle 67°, and the third with front cascade stagger angle 72° and rear cascade with stagger angle 67°.

Senoo et al. (1983) compared the results of the LSVDs to the results of a vaneless diffuser. The LSVDs showed better pressure recovery but no reduction in flow range. In the case of the single cascade LSVD the stagger angle 70° showed slightly larger flow range and better pressure recovery at the surge than the LSVD with stagger angle 68°. By increasing the solidity to 0.83 the flow range decreased but there was no major difference at the pressure recovery. The tamdem cascade diffuser provided better pressure recovery than the single cascade. On the other hand, no major differences at the flow range were seen between different tamdem cascade LSVDs. The performance of the diffuser was well predicted by a simple method of combining a convectional theory of a circular cascade and of a vaneless diffuser.

Oil film patterns from the single row cascade showed that the side wall boundary layer moved from the suction side of the blade to the pressure side of the adjacent blade. This phenomenon delayed the separation of the boundary layer on the suction surface. Oil film patterns from the tamdem row cascade showed that the growing boundary layer from the front blade was channelled to the main flow through the slit and a new boundary layer was developed at the rear blade. Because of this phenomenon both blades could have almost independent pressure rise and therefore a good pressure rise over the whole diffuser.

Senoo (1984) presents data of a previously designed LSVD Senoo et al. (1983). Also the new LSVD with 22-vanes was designed and tested. Solidity 0.69 and stagger angle 71° were used. The result of the 22-vane LSVD was compared with the 11-vane LSVD introduced in Senoo et al. (1983). The diffuser with the higher number of blades achieved a better peak pressure recovery but at the low flow rate the pressure recovery was smaller. On the other hand, both diffusers had equally large flow range. When the solidity was decreased the pressure recovery did not change at the high and at the medium flow but decreased at the low flow. Also the flow range was decreased at the low flow. The lower stagger angle of the vane gave better pressure recovery at the high low but lower at the low flow. The influence to the flow range was quite minimal. The oil trace along the side walls demonstrated that a high lift coefficient was possible when the boundary layer on the vane suction surface was removed by the secondary flow along the side walls. The pressure distribution near the blade by potential flow analysis showed that the number of vanes, solidity and stagger angle are important parameters to control the secondary flow along the side wall.

In Hayami et al. (1990), two different low solidity vaned diffusers were designed for a refrigeration centrifugal compressor. The flow in the outlet of the impeller and at the leading edge of the diffuser vanes was supersonic. The impeller had 15 full and splitter blades with the back sweep of 40°. The exit blade width was 8.9 mm. The low solidity vaned diffuser vanes had a double circular arc shape with stagger angles 72° and 69°. The leading edge radius ratio was 1.1

and the vanes had a 10° turning angle. The width of the diffuser vanes was 9.4 mm. The results of the LSVD were compared with a constant area vaneless diffuser. The higher stagger angle showed better results at the high rotational speed and at the lower flow rate. The lower stagger angle showed better results at the lower speed and the higher flow rate. The efficiency and the pressure recovery of the LSVDs were superior compared to the vaneless diffuser. Also the flow range at low flow was found to be better with the LSVD. The maximum efficiency was reached at the incidence angle -2° to -3°.

In Sorokes and Welch (1992), four different rotatable low solidity vaned diffusers were measured. They studied the effect of a vane leading edge radius ratio and the chord length of the vane. Vane inlet radius ratios 1.08 and 1.15 and 10 long vanes and 20 short vanes were used. The vane setting angle was set to 68° and it was possible to move the vanes $\pm 10^\circ$ with rotatable diffuser vanes to study the effect of stagger angle. Flat plate vanes with slightly thinner leading edge were used. It was concluded that the longer chord length at reduced leading edge radius ratio yielded the best diffuser recovery. The LSVD limited the overload capacity when the vanes were most tangential (the stagger angle was largest). This happened especially with the 20-vane construction. It was noticed that the decrease of the stagger angle reduced the flow range at the low flow and vice versa. The decrease of the flow range was more dramatic when the stagger angle was decreased. Sorokes and Welch (1992) noticed that the effect of different LSVDs to the overall stage efficiency of the head coefficient was minimal, even though the LSVD with long vanes showed better pressure recovery. They concluded that the LSVD influenced the performance of the downstream component.

Hohlweg et al. (1993) have compared low solidity vaned diffusers against the conventional vaned diffuser and the vaneless diffuser. The comparisons were made with an air compressor and a process compressor where the working gas was nitrogen. Three different LSVDs were designed for the air compressor with incidence angles -4.1°, -1.9° and $+0.3^\circ$. All the LSVDs had solidity 0.7. The largest negative incidence yielded the largest flow range, almost as large as with the vaneless diffuser. The efficiency was little bit lower than with the vaned diffuser. The flow range was decreased at the low flow rate when the incidence was increased. The best efficiency was attained with the incidence angle -1.9°, but it was lower than the efficiency attained with the vaned diffuser. It was concluded that a positive incidence is not a good choice when designing LSVDs.

Engeda (1996), Aminemi et al. (1996), Amineni and Engeda (1997), Kim and Engeda (1997), Engeda (1997) and Engeda (1998) have tested LSVDs with different solidities and blade numbers. Incidence angle -2° and flat plate vanes were used in all configurations. It was shown that higher solidity decreased the operation range. On the other hand, higher solidity yielded better pressure recovery. The increase of the vane number yielded a lower turning angle of the vane when

the solidity was kept constant. The surge margin was improved by increasing the blade number. It was explained that the shorter vanes allow a higher positive incidence angle because of the smaller turning angle. The fewer number of vanes yielded better efficiencies at high rotational speeds. This was explained to be caused by the higher turning angle, which yielded a shorter flow path.

Eynon and Whitfield (1997) have investigated five different LSVDs with the same solidity 0.69. The number of vanes (6, 8 and 10) and the vane turning angle ($10°$, $15°$ and $20°$) were varied. No large changes were seen when the number of the vanes was varied. On the other hand, more vanes led to a slightly narrower operation range at the high flow area. When the turning angle was increased the efficiency was increased. This was seen especially at the higher rotational speeds. The higher turning angle also led to a wider operation range at the high flow area but decreased the flow range at the low flow, especially at the high rotational speeds. The increase of the turning angle increased the pressure recovery at the diffuser. However, it reduced the volute pressure recovery and therefore there was no or little improvement in pressure recovery over the diffuser/volute system.

Sorokes and Koch (2000) have studied the influence of the LSVD on static pressure non-uniformity caused by the volute. The LSVD was placed on the process compressor, and the static pressure along a circumference at the impeller inlet, outlet and diffuser outlet were measured. Also dynamic pressure probes were used, and strain gages were used to measure forces acting on the impeller. The diffuser and the volute were modelled numerically. It was noticed that the LSVD decreased the influence of the pressure non-uniformity caused by the volute to the impeller compared to the vaneless diffuser case. This was also confirmed with the strain gage measurements. Also the numerical calculation showed the same trend.

Bonaluti et al. (2002) have investigated the flow field in a low solidity vaned diffuser using steady and unsteady calculation. The calculated results were compared to previously made measurements by Hayami et al. (1990). The steady calculation showed good agreement with the measured values. The work factor, the pressure ratio and the adiabatic efficiency were studied. Also the flow condition at the diffuser inlet and the distribution of the isentropic Mach number along the cascade vane were studied. Special attention was paid the secondary flow in the diffuser cascade. The unsteady results confirmed the flow structure found with the steady calculation and a high level of unsteadiness was associated with the recirculating zones.

2.3.3 Impeller-diffuser interaction

The interaction between an impeller and a convectional vaned diffuser has been studied by many authors. Krain (1981) has measured the unsteady pressure and the flow angle fluctuation at the semi-vaneless space between the vaned diffuser and the impeller.

Justen et al. (1999) have measured the unsteady static pressure in a flat wedge vaned diffuser. The leading edge radius ratios 1.10 and 1.06 and two different vane angles were used. It was found that the reduced vane angle did not change the basic-structure of the time-dependent flow in the diffuser at low flow. Enlargement of the vaneless space decreased the unsteadiness and reduced the fluctuation level at the diffuser leading edge. Also the peak efficiency of the compressor was higher with the larger leading edge radius ratio. The pressure measurements revealed that the semi-vaned space mainly into the region near the vane suction side was influenced by the unsteady impeller-diffuser interaction. The unsteadiness did not decay in the diffuser channel.

Koumoutsos et al. (2000) have done an unsteady numerical simulation of the centrifugal compressor and of the vaned diffuser previously measured by Krain (1981). There was a fairly good agreement between the measured and the calculated data. Koumoutsos et al. also compared the results between the steady-state and the time-averaged results, and differences between the results were noticed.

Shum et al. (2000) have studied the impeller-diffuser interaction numerically. To model the influence of unsteadiness to the diffuser flow, calculations were conducted also without unsteadiness and circumferential non-uniformity and without unsteadiness and axial non-uniformity. The effect of the impeller unsteadiness had the same order of magnitude impact on the diffuser pressure recovery and loss as the axial distortion. This impact was small compared to the impact of the inlet flow angle of the diffuser. It was concluded that the impeller-diffuser interaction had a pronounced effect on the impeller tip clearance flow and as a consequence an impact on loss, blockage, slip and stage pressure rise. The reduced radial gap influenced more the impeller operation than the diffuser operation. There is an optimum radial gap between the impeller and the diffuser blades because when the radial gap is reduced the penalty of increased loss overcomes the benefits of the reduced blockage and the slip.

Ziegler et al. (2003a) and Ziegler et al. (2003b) have made an extensive study on impeller-diffuser interaction. They changed the leading edge radius ratio from 1.04 to 1.18. It was noticed that the smaller radial gap increased the total pressure ratio, and the maximum increase of the isentropic efficiency was 0.9 points. On the other hand, the smaller radial gap decreased the operation range of the compressor. It was also noticed that the changed of the radial gap hardly changes the efficiency of the impeller. In most cases the flow field in the diffuser vane exit was

more homogenous with the smaller radial gap, indicating better diffusion. The reason for this was the unloading of the typically highly loaded pressure side of the vane. A significant reduction of the wake region at the impeller exit was found with the vaned diffuser compared to the vaneless diffuser. The smaller radial gap further reduced the wake region. It was also found that the non-uniformities in the flow angle mixed out more rapidly than the non-uniformities in the velocities. The diffuser vane had a time and area averaged suction side incidence about 5° already in the best point, which indicated generally high loaded pressure side of the vane. At the small radial gap this high loading was reduced by the pressure sided incidence of the impeller wake fluid. At the large radial gap the wake flow had a more radial direction and this minimized its the positive effect. Generally a small radial gap is recommended if a wide flow rate is not the main target.

3 Numerical procedure

3.1 Introduction

The tested compressors and different geometries were analyzed numerically. Also numerical simulations were done to analyze further the effect of different pinches and different low solidity vaned diffusers. The quasi-steady approach was utilized to study the effect of different geometries. The inlet cone, rotor and stator were modelled. The periodicity of the geometry was used in the case of the vaneless diffuser and only two rotor passages were modelled. In the cases of low solidity vaned diffusers the whole rotor and stator were modelled. The volute was not modelled. On the other hand, most of the cases were simulated only at the design point were the upstream effect of the volute is minimal. Time-accurate simulations were conducted to study the unsteady phenomena in the vaneless diffuser. The whole compressor stage was modelled. The computational domain consisted of the inlet pipe, inlet cone, full impeller, vaneless diffuser, volute, exit cone and exit pipe.

The flow solver Finflo was used to solve the flow field. Finflo is a Navier-Stokes solver developed at Helsinki University of Technology (HUT). The solver is capable to solve compressible, incompressible, steady and unsteady flow fields. An overview of the solved equations and the methods used in Finflo are described in the next chapters. More details can be found for example in Siikonen (1995), Rautaheimo et al. (1999) and Siikonen et al. (2001).

3.2 Governing equations

The Reynolds averaged Navier-Stokes (RANS) equations are solved using the Finite Volume Method. The Cartesian coordinates are used. The RANS equations and the equations describing turbulence can be written in a conservative form

$$\frac{\partial U}{\partial t} + \frac{\partial (F - F_v)}{\partial x} + \frac{\partial (G - G_v)}{\partial y} + \frac{\partial (H - H_v)}{\partial z} = Q \tag{4}$$

where U is the vector of the conservative variables

$$U = \left[\begin{array}{ccccccc} \rho & \rho u & \rho v & \rho w & E & \rho k & \rho \epsilon \end{array} \right]^T \tag{5}$$

and where F, G and H are inviscid fluxes, F_v, G_v and H_v are viscous fluxes and Q is the source term. The inviscid fluxes are

$$F = \begin{pmatrix} \rho\hat{u} \\ \rho u\hat{u} + p + \frac{2}{3}\rho k \\ \rho v\hat{u} \\ \rho w\hat{u} \\ E\hat{u} + pu + \frac{2}{3}\rho k\hat{u} \\ \rho\hat{u}k \\ \rho\hat{u}\epsilon \end{pmatrix} G = \begin{pmatrix} \rho\hat{v} \\ \rho u\hat{v} \\ \rho v\hat{v} + p + \frac{2}{3}\rho k \\ \rho w\hat{v} \\ E\hat{v} + pv + \frac{2}{3}\rho k\hat{v} \\ \rho\hat{v}k \\ \rho\hat{v}\epsilon \end{pmatrix}$$

$$H = \begin{pmatrix} \rho\hat{w} \\ \rho u\hat{w} \\ \rho v\hat{w} \\ \rho w\hat{w} + p + \frac{2}{3}\rho k \\ E\hat{w} + pw + \frac{2}{3}\rho k\hat{w} \\ \rho\hat{w}k \\ \rho\hat{w}\epsilon \end{pmatrix} \tag{6}$$

Here ρ is density, u, v and w are the absolute velocities in the x-, y- and z-direction in the Cartesian coordinate system, p is the pressure, E is the total energy, k is the kinetic energy of the turbulence and ϵ is the dissipation of the kinetic energy of the turbulence. In quasi-steady simulations the coordinate system rotates around the x-axis with the angular velocity Ω. The convective, i.e. relative speeds shown in equation (6) are given as

$$\hat{u} = u \tag{7}$$

$$\hat{v} = v + \Omega z \tag{8}$$

$$\hat{w} = w - \Omega y \tag{9}$$

The total energy E is defined as

$$E = \rho e + \rho\frac{u^2 + v^2 + w^2}{2} + \rho k \tag{10}$$

where e is the specific internal energy. The equation of state of perfect gas is used to calculate pressure

$$p = (\gamma - 1)\rho e \tag{11}$$

where γ is the ratio of specific heats c_p/c_v. The source term Q in equation (4) is a vector of conservative variables and has non-zero components for the equation for y- and z-momentum and turbulence

$$Q = \begin{bmatrix} 0 & 0 & \rho\Omega w & -\rho\Omega v & 0 & Q_k & Q_\epsilon \end{bmatrix}^T \tag{12}$$

The terms Q_k and Q_ϵ are the source terms of the turbulence model and are described in the next chapter. The viscous fluxes in equation (4) are described as

$$F_v = \begin{pmatrix} 0 \\ \tau_{xx} \\ \tau_{xy} \\ \tau_{xz} \\ u\tau_{xx} + v\tau_{xy} + w\tau_{xz} - q_x \\ \mu_k(\frac{\partial k}{\partial x}) \\ \mu_\epsilon(\frac{\partial \epsilon}{\partial x}) \end{pmatrix} G_v = \begin{pmatrix} 0 \\ \tau_{xy} \\ \tau_{yy} \\ \tau_{yz} \\ u\tau_{xy} + v\tau_{yy} + w\tau_{yz} - q_y \\ \mu_k(\frac{\partial k}{\partial y}) \\ \mu_\epsilon(\frac{\partial \epsilon}{\partial y}) \end{pmatrix}$$

$$H_v = \begin{pmatrix} 0 \\ \tau_{xz} \\ \tau_{yz} \\ \tau_{zz} \\ u\tau_{xz} + v\tau_{yz} + w\tau_{zz} - q_z \\ \mu_k(\frac{\partial k}{\partial z}) \\ \mu_\epsilon(\frac{\partial \epsilon}{\partial z}) \end{pmatrix} \tag{13}$$

where q_i is the heat flux, μ_k is the diffusion coefficient of k, μ_ϵ is the diffusion coefficient of ϵ and the viscous stress tensor is

$$\tau_{ij} = \mu\Big[\frac{\partial u_j}{\partial x_i} + \frac{\partial u_i}{\partial x_j} - \frac{2}{3}(\nabla \cdot \vec{V})\delta_{ij}\Big] - (\overline{\rho u_i'' u_j''} - \frac{2}{3}\rho k\delta_{ij}) \tag{14}$$

Here μ is molecular viscosity, $\overline{\rho u_i'' u_j''}$ are Reynolds stresses and δ_{ij} is the Kronecker's Delta function defined as

$$\begin{cases} \delta_{ij} = 0 & \text{if } i \neq j \\ \delta_{ij} = 1 & \text{if } i = j \end{cases} \tag{15}$$

Reynolds stresses are modelled using the turbulence model described in the next chapter. The heat flux in equation (13) is written as

$$\vec{q} = -(k + k_T)\nabla T = -\left(\mu\frac{c_p}{Pr} + \mu_T\frac{c_p}{Pr_T}\right)\nabla T \tag{16}$$

where μ_T is the turbulent viscosity defined by the turbulence model and Pr is the Prandtl number. The diffusion coefficients of turbulence quantities in equation (13) are approximated as

$$\mu_k = \mu + \tfrac{\mu_T}{\sigma_k} \quad \mu_\epsilon = \mu + \tfrac{\mu_T}{\sigma_\epsilon} \tag{17}$$

where σ_k and σ_ϵ are Schmidt's numbers defined by the turbulence model.

Equation (4) is written in an integral form for the finite volume method

$$\frac{d}{dt}\int_V UdV + \int_S \vec{F}(U)\cdot d\vec{S} = \int_V QdV \tag{18}$$

where U is defined in equation (5) and $\vec{F}(U)$ is the flux vector. A discrete form of equation (18) is achieved by integrating over the control volume and surface for a computational cell i

$$V_i\frac{dU_i}{dt} = \sum_{faces} -S\hat{F} + V_iQ_i \tag{19}$$

where the sum is taken over the faces of the computational cell i and S is the area of the cell face. The flux $\hat{F}$ is defined for each face

$$\hat{F} = n_x(F - F_v) + n_y(G - G_v) + n_z(H - H_v) \tag{20}$$

where n_x, n_y and n_z are the unit normal vectors at the x-, y- and z-directions, F, G and H are the inviscid and F_v, G_v and H_v are the viscous fluxes defined in equations (6) and (13).

Inviscid fluxes are evaluated using Roe's method (Roe 1981). The flux is calculated as

$$\hat{F} = T^{-1}F(TU) \tag{21}$$

where T is a rotation matrix transforming the variables to a local coordinate system normal to the cell surface. A MUSCL-type approach has been adopted for primary flow variables and conservative turbulent variables.

The viscous fluxes are evaluated using thin-layer approximation. The discretized equations are integrated in time by using the DDADI-factorization (Lombard et al. 1983). DDADI-factorization is based on the approximate factorization and on the splitting of the Jacobians of the flux terms.

3.3 Turbulence modelling

Accurate modelling of turbulence is difficult and computationally very time consuming. Therefore direct numerical simulation (DNS) and large-eddy simulations (LES) are generally not used in engineering problems. Also Reynolds stress models are hard to use and require fairly large computational resourses. Turbulence models based on Boussinesq approximation are widely used because they are computationally less expensive and relatively accurate to model the main stream flow. On the other hand, if the anisotrophy of the turbulence is important, the Reynolds stress turbulence models should be used.

Kunz and Lakshminarayana (1992) have calculated a centrifugal compressor rotor using a coupled $k-\epsilon$ turbulence model. They have compared the results

to measured values and the computational results are good. On the other hand, the computational grid at the shroud was not properly modelled because of a too coarse grid. Hathaway et al. (1993) have calculated a NASA low-speed centrifugal compressor rotor and a vaneless diffuser using the Baldwin-Lomax turbulence model. The calculated results were compared to laser anemometry results. It was noticed that the CFD calculations underpredicted the maximum velocity deficit in the wake and spanwise extent of the wake. Rautaheimo et al. (1999) have compared three different turbulence models in a simulation of the NASA low-speed centrifugal compressor. A comparison was made between an algebraic model of Baldwin and Lomax (1978), $k-\epsilon$ model of Chien (1982) and a full Reynolds stress closure by Speziale et al. (1991). Rautaheimo et al. (1999) concluded that the Baldwin-Lomax and Chien's $k-\epsilon$ models predicted the overall performance of the compressor well, while the Reynolds stress model slightly under-predicted the efficiency and pressure ratio. On the other hand, detailed flow phenomena were best captured by the Reynolds stress model. Rautaheimo et al. (1999) also concluded that Chien's $k-\epsilon$ model predicted well the overall performance of the compressor with a very coarse grid. Turunen-Saaresti (2001) has calculated the whole centrifugal compressor stage using the Baldwin-Lomax and Chien's $k-\epsilon$ turbulence models. It was found that Chien's $k-\epsilon$ turbulence model showed better results than the Baldwin-Lomax turbulence model. It was also found the Baldwin-Lomax turbulence model was more sensitive to the grid size.

On the basis of the literature survey made on turbulence models and the available computational resources, Chien's $k-\epsilon$ turbulence model is used in the numerical calculations in this thesis. Chien's $k-\epsilon$ turbulence model is a low Reynolds number turbulence model, which means that no wall functions are used, and the boundary layer is calculated if the grid size is sufficient. Therefore, the grid size near the walls should be dense enough. The Boussinesq approximation is made for the Reynolds stresses defined as

$$-\overline{\rho u_i'' u_j''} = \mu_T \left[\frac{\partial u_j}{\partial x_i} + \frac{\partial u_i}{\partial x_j} - \frac{2}{3}(\nabla \cdot \vec{V})\delta_{ij} \right] - \frac{2}{3}\rho k \delta_{ij} \tag{22}$$

The source terms in equation (12) are defined in Chien's model as

$$Q_k = P - \rho\tilde{\epsilon} - 2\mu\frac{k}{y_n^2} \tag{23}$$

$$Q_\epsilon = C_1\frac{\tilde{\epsilon}}{k}P - C_2\frac{\rho\tilde{\epsilon}^2}{k} - 2\mu\frac{\tilde{\epsilon}}{y_n^2}e^{\frac{-y^+}{2}} \tag{24}$$

where y_n is the normal distance from the wall and y^+ is defined as

$$y^+ = y_n\frac{\rho u_T}{\mu_w} = y_n\frac{\sqrt{\rho\tau_w}}{\mu_w} \tag{25}$$

Here u_T is the friction velocity, μ_w is the molecular viscosity on the wall and τ_w is the shear stress on the wall. $\tilde{\epsilon}$ is solved instead of ϵ in Chien's turbulence model. It obtains zero value at the wall and the normal dissipation can be solved as

$$\epsilon = \tilde{\epsilon} + 2\frac{\mu k}{\rho y_n^2} \tag{26}$$

The production of the turbulent kinetic energy is modelled as

$$P = \left(-\overline{\rho u_i'' u_j''}\right) \frac{\partial u_i}{\partial x_j} \tag{27}$$

where the Boussinesq approximation (22) is used. The turbulent viscosity μ_T is calculated in the $k-\epsilon$ model as

$$\mu_T = C_\mu \frac{\rho k^2}{\tilde{\epsilon}} \tag{28}$$

The production of the turbulent kinetic energy P is limited as suggested by Menter (1994) in order to avoid unphysical growth of the turbulence viscosity

$$P = min(P, 20\rho\tilde{\epsilon}) \tag{29}$$

The empirical coefficient used in the equations for k and ϵ are

$$\begin{array}{ll} C_1 = 1.44 & \delta_k = 1.0 \\ C_2 = 1.92\left(1 - 0.22e^{-Re_T^2/36}\right) & \sigma_\epsilon = 1.3 \\ C_\mu = 0.09\left(1 - e^{-0.0015y^+}\right) & \end{array} \tag{30}$$

where the turbulent Reynolds number is defined as

$$Re_T = \frac{\rho k^2}{\mu\epsilon} \tag{31}$$

3.4 Boundary conditions

The inflow boundary conditions were given at the beginning of the inlet cone 249 cm above the impeller leading edge. Total entalphy and momentum distribution were given as the boundary conditions and the static pressure was extrapolated from the computational domain. Intensity of the turbulence and the non-dimensional turbulent viscosity μ_T/μ were defined at the inflow boundary condition. The flow was assumed to be fully axial and a constant distribution of the momentum and turbulence quantities was applied. On the other hand, the

momentum and turbulence quantities will develop before the flow enters the impeller. The outflow boundary condition was defined at the end of the diffuser at the radius ratio $r/r_2 = 1.67$. A constant distribution of the static pressure was given and the velocity gradients were assumed to be zero. This kind of boundary condition at the end of the diffuser is physically adequate at the design operation point of the compressor where the circumferential static pressure distribution is constant. The circumferentially varying pressure field due to the volute at the off-design operation point is not taken into account when using this kind of boundary condition.

For the time-accurate simulations the inflow boundary conditions for the numerical simulation were given in the beginning of the inlet pipe, which was located 1.05 metres above the impeller leading edge. The outflow boundary conditions were given in the end of the outlet pipe, 1.60 metres downstream of the end of the volute. The same boundary conditions were used as quasi-steady calculations at the inlet and outlet.

The time-accurate simulation was based on the three-level fully implicit second order time-integration method. This method is described in Hoffren (1992). Inner iterations are made at every time step. The number of inner iterations is chosen to get convergence for each time step. In the present case 25 seemed to be enough. In this case the time step is $1\mu s$, which has been found to be small enough to get a solution. The rotor of the compressor is rotated 0.13° at every time step. The connection between the stationary and the rotating part of the mesh is handled by using a sliding mesh technique. The grid lines between the impeller blocks and the stator block are discontinuous, thus a mass conserving interpolation is made at every time step Rai (1986).

4 Numerical results

4.1 Numerical cases

The calculations were conducted at low, design and high flow at the design rotation speed. The original geometry with an unpinched diffuser and different kinds of pinches were tested. The pinch amount was 5% and 10% of the height of the unpinched diffuser and the pinch was made by moving the hub or the shroud wall, or both walls. The design operation point of the compressor was modelled for every geometry. The unpinched geometry and the geometry with 10% pinch from the hub and the shroud was also modelled at low and high flow. The design rotation speed was used. The low, design and high flow correspond to 0.56, 1.00 and 1.34 times the design volume flow of the compressor. The surface grid of the unpinched geometry is shown in figure 6 and details on the pinched diffuser in figure 7.

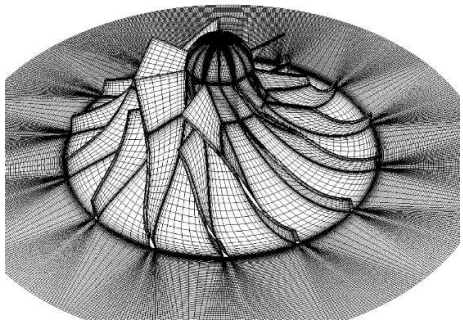

Figure 6: Surface grid of unpinched diffuser. Every second grid line is visible.

The effect of the number of vanes was tested by modelling the low solidity vaned diffuser with 7, 9 and 11 vanes. The effect of the shape of the vane was also tested. Flat plate vanes, vanes with a circular arc chamber line and constant thickness distribution, and vanes with a circular arc chamber line and a NACA thickness distribution were modelled. 9 vanes were used with different kinds of vane geometries. The geometrical parameters of the modelled low solidity vaned diffuser are shown in table 1 and the surface grids of the modelled low solidity vaned diffusers in figure 8. The NACA 65-(10)10 thickness profile was used (Herrig et al. 1958). The design operation point was modelled with every geometry and the geometry with 9 vanes and the NACA thickness profile was also modelled at low and high flow.

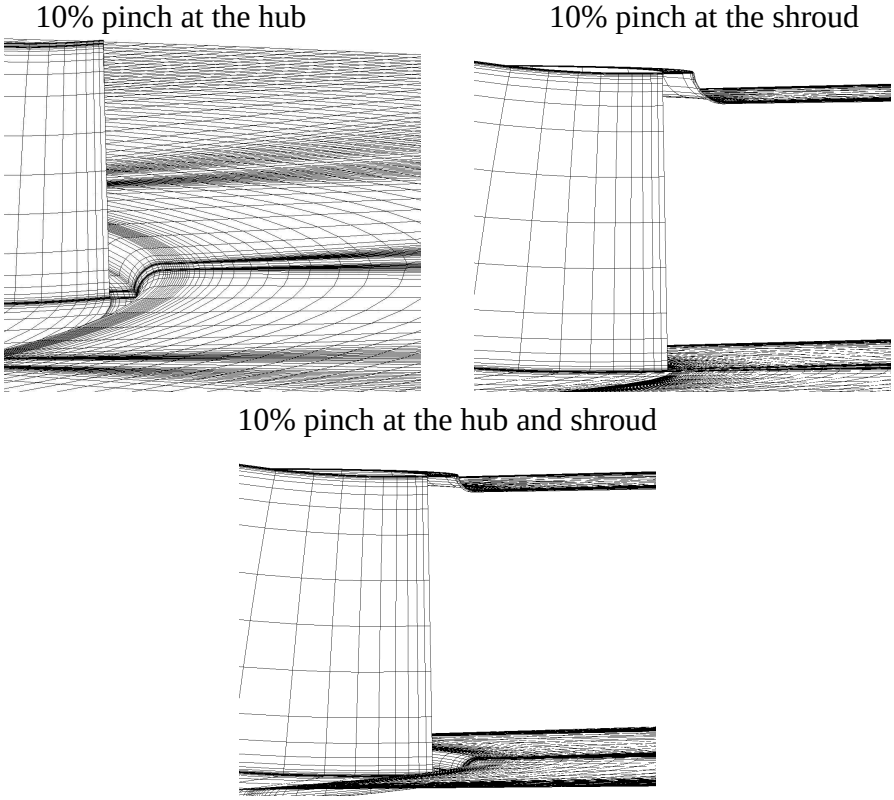

Figure 7: Details of pinched diffusers.

Table 1: Geometrical parameters of the modelled LSVD

name	$\frac{b_{2'}}{b_2}$	σ	$\frac{r_{2'}}{r_2}$	$\frac{r_3}{r_2}$	$\frac{r_4}{r_2}$	N	θ	i
LSVD 9 flatplate	1.00	0.65	1.1	1.355	1.681	9	$19.68°$	$-2°$
LSVD 9 const. prof.	1.00	0.65	1.1	1.319	1.681	9	$10°$	$-2°$
LSVD 7 NACA	1.00	0.65	1.1	1.355	1.681	7	$10°$	$-2°$
LSVD 9 NACA	1.00	0.65	1.1	1.319	1.681	9	$10°$	$-2°$
LSVD 11 NACA	1.00	0.65	1.1	1.279	1.681	11	$10°$	$-2°$

The entire compressor was modelled in order to conduct time-accurate numerical simulations. The time-accurate simulations were conducted to another compressor than quasi-steady simulations. The compressors are described in chapter 5.1. The computational grid of the compressor was divided to 33 blocks and the number of computational cells is 618 496. The surface grid of the compressor is shown in figure 9. Every second grid line is visible. Tip clearance was not modelled. The topology of the grid has been made in such a way that all the blocks

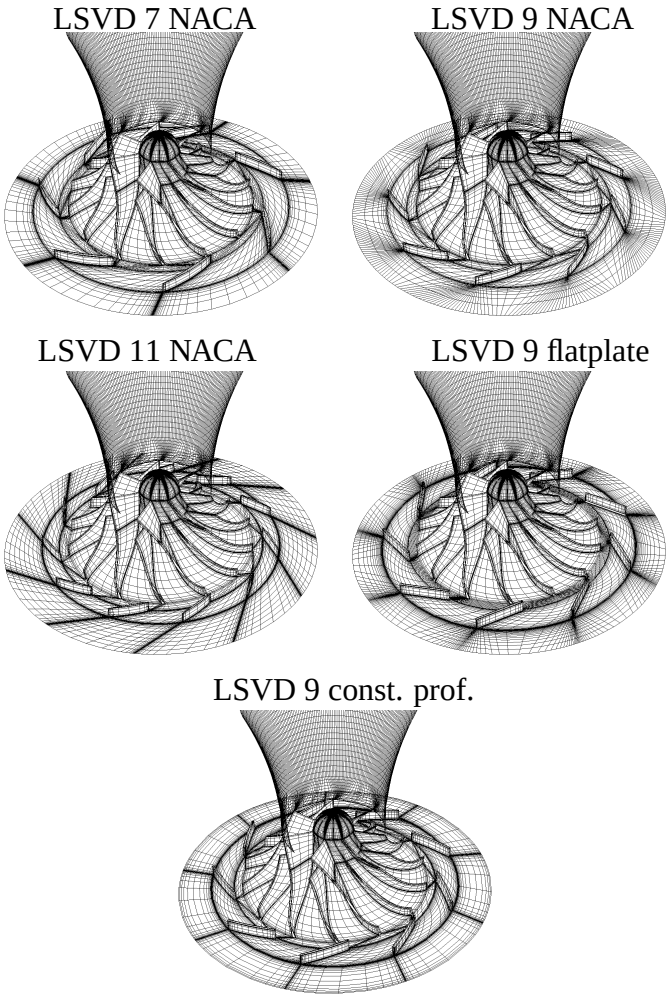

Figure 8: Surface grids of low solidity vaned diffusers. Every second grid line is visible.

except the ones in the volute and in the exit cone contain clustering to the walls (figure 10).

Tip clearance was not modelled in the numerical calculations. This causes some uncertainty to the numerical results. However, the effect of the tip clearance to the efficiency can be calculated from the studies provided by Japikse and Goebel (1979) and Dibelius et al. (1984). The decrement of the efficiency due to the tip clearance is about 2.5% of the design efficiency of the original geometry. In the study of Farge et al. (1989) the effects of the tip clearance have been studied. They noticed that the static pressure was only slightly affected by the tip leakage. Farge et al. (1989) also noticed that the wake at the shroud was much

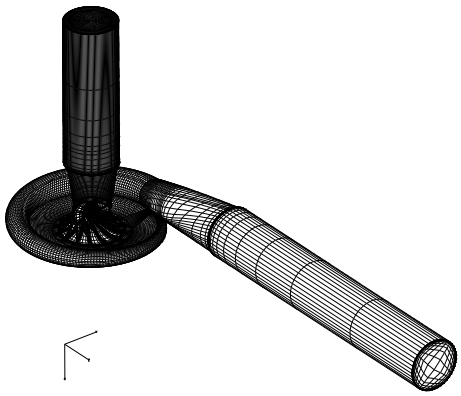

Figure 9: The surface grid of the compressor. Every second grid line is visible.

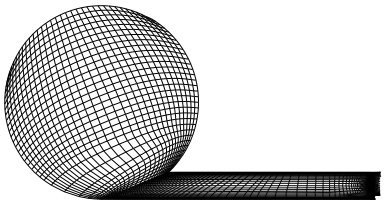

Figure 10: The computational grid of the volute and the diffuser at the 360-degree circumferential position.

closer to the pressure surface when the tip clearance was present. The effect of the tip clearance was more pronounced in the circumferential direction than in the axial direction. However, e.g. Pinarbasi and Johnson (1994) have shown that non-uniformities in the circumferential direction mixed out rapidly in the diffuser, and therefore omitting the tip clearance does not significantly affect to the prediction of the flow field in the diffuser. The tip clearance was not modelled because it would have required more computation time and capacity.

The convergence of the simulations was monitored. The convergence criteria was based on the mass flow difference between inlet and outlet, L_2-norm of residuals of density, averaged pressure and temperature. The measured results were used in order to further verify the numerical results.

4.2 Overall performance of the compressor

The overall performance of the compressor is evaluated using the isentropic efficiency and total-total pressure ratio. The isentropic efficiency is defined as

$$\eta_{st-t} = \frac{h_{t4s} - h_{t1}}{h_{t4} - h_{t1}} \approx \frac{T_{t4s} - T_{t1}}{T_{t4} - T_{t1}} \tag{32}$$

where h is the specific enthalpy and T the temperature with subscript t referring the total state and subscript s referring to the isentropic compression. The total-total pressure ratio is defined as

$$\pi_{t-t} = \frac{p_{t4}}{p_{t1}} \tag{33}$$

where p is the pressure.

The calculated and measured isentropic efficiency and the total-total pressure ratio of the different constructions are shown in table 2. The values have been calculated to the diffuser outlet and the isentropic efficiency has been made non-dimensional by dividing it with the isentropic efficiency of the original geometry at the design point. The measured values are presented here in order to verify the numerical results. The experimental setup is discussed later in chapters 5.1 and 5.3. It can be seen that the total-total pressure ratio is fairly well predicted compared to the measured values at all constructions. The isentropic efficiency is clearly over-predicted in all cases. The largest difference is seen at the high flow and the lowest difference at the low flow. The improved efficiency of the pinched diffuser is captured. However, the efficiency of the LSVD (NACA 9 LSVD) is lower than the vaneless diffuser in CFD calculations. This is caused by the use of the quasi-steady approach, which does not properly take into account the rotor-stator interaction. On the other hand, the difference between the calculated and the measured isentropic efficiency is smaller in the case of the low solidity vaned diffuser compared to the vaneless diffusers. The calculated efficiency values are slightly higher, which can be partly explained by the absence of the tip clearance. The volute has not modelled either, which affects the calculated results at the off-design points. The nearly correct pressure ratio and the clearly over-predicted isentropic efficiency indicates that the temperature rise is under-predicted.

The 5% pinch made to the hub wall shows only small increase in the isentropic efficiency and in the total-total pressure ratio (see table 2). The 5% pinch made to the shroud also shows a small increase in the isentropic efficiency but no increase in the total-total pressure ratio. The 5% pinch made to the hub and to the shroud walls shows a small decrease in the isentropic efficiency and a small increase in the total-total pressure ratio. It can be seen in table 2 that the 2.5% pinch is too small to make any difference in the diffuser performance, even if it is made to

Table 2: Calculated and measured total-total pressure ratio and isentropic efficiency of the compressor at various constructions.

	π_{t-t} [-]		η_{ist-t} [-]	
	CFD	Measured	CFD	Measured
VNL low flow	1.93	1.89	1.024	0.959
VNL design flow	1.84	1.76	1.099	1.026
VNL high flow	1.60	1.56	1.034	0.879
VNL pinch hub 5%	1.88	-	1.107	-
VNL pinch shroud 5%	1.84	-	1.103	-
VNL pinch hub & shroud 5%	1.86	-	1.097	-
VNL pinch hub 10%	1.93	-	1.102	-
VNL pinch shroud 10%	1.87	-	1.102	-
VNL pinch hub & shroud 10% low	1.95	1.93	1.034	0.955
VNL pinch hub & shroud 10% design	1.89	1.82	1.131	1.048
VNL pinch hub & shroud 10% high	1.63	1.62	1.038	0.933
LSVD 7 NACA	1.81	-	1.049	-
LSVD 9 NACA low flow	1.76	1.85	0.912	0.897
LSVD 9 NACA design flow	1.84	1.82	1.086	1.039
LSVD 9 NACA high flow	1.66	1.58	1.023	0.774
LSVD 11 NACA	1.86	-	1.132	-
LSVD 9 flatplate	1.85	-	1.064	-
LSVD 9 const. prof.	1.82	-	1.054	-

both walls. When the pinch is further increased to 10% to diffuser height it can be seen that the isentropic efficiency is increased slightly compared to the diffuser without the pinch in the cases where the pinch is made to the hub or to the shroud wall. On the other hand, the increase in the isentropic efficiency is slightly smaller with the 10% pinches than the 5% pinches made to the hub or to the shroud wall. This indicates that the 10% pinch to the one wall is too large step in the diffuser inlet. The total-total pressure ratio shows larger increment in the 10% pinches than the 5% pinches made to the hub or to the shroud wall. The 10% pinch made to the hub and shroud wall shows a significant increase in the isentropic efficiency. The increase of the isentropic efficiency is also seen in the measurements. The efficiency increment is larger in the numerical results than in the measured results at the low and design flow. The measured efficiency increment is larger than numerical efficiency increment at the high flow. The total-total pressure ratio is increased in the calculated and measured results at the low flow. However, the increment is larger at the measured results.

Also different kinds of low solidity vaned diffusers were analyzed numerically. The effect of the vane shape and the number of vanes were analyzed. Only the design operation point was modelled. It can be seen in table 2 that the increased number of the low solidity vanes leads to increased isentropic efficiency and total-

total pressure ratio at the design operation point. This kind of results can also be found in the literature (Senoo 1984 and Engeda 1998). The low solidity vanes with the circular arc chamber line and NACA thickness profile show the best isentropic efficiency. The results of the constant thickness profile vanes show that the circular arc chamber line has a lower isentropic efficiency than the straight line chamber line (flatplate construction). The effect of the vane shape and the number of vane to the total-total pressure ratio is minor. The 9-vane construction with the NACA thickness profile was also modelled in off-design conditions. It can be seen that the total-total pressure ratio is fairly well predicted compared to the measured values at the design and high flow, but clearly under-predicted at the low flow. The low flow operation point in the measurement is slightly higher flow rate than the simulated low flow operation point. The simulated low flow operation point could not be reached in the measurements because the compressor stalled. The numerical results also predicted narrower flow range because the predicted pressure ratio is lower at the low flow than at the design flow.

The isentropic efficiency and the pressure ratio of the impeller are shown in table 3. It can be seen in the measured results that part of the efficiency rise seen with the pinched diffuser is due to the better efficiency of the impeller. This is seen at the design and at the high flow. The efficiency of the impeller did not change at the low flow. However, this efficiency increment of the impeller is not seen in the calculated results at the design flow. It can also be seen that the larger the increment of the efficiency of the impeller, the larger the flow rate. Also the LSVD has an effect on the efficiency of the impeller but it is smaller compared to the pinch. The increment is only seen at the design and high flow in the measured values. The calculated results show that the LSVD has decreased the efficiency of the impeller. This is also seen in the efficiency in table 2. However, the calculated diffuser performance is better with the LSVD than the vaneless diffuser (discussed in chapter 4.4).

4.3 Detailed flow fields in diffusers

The spanwise total pressure, the circumferential static and total pressure, and the radial distribution of the static pressure are plotted to examine the flow field in the diffusers.

Figure 11 shows the circumferential variation of the static pressure at the diffuser inlet radius ratio $r/r_2 = 1.048$ in the vaneless diffusers at the design operation condition. A higher pressure in the impeller blade pressure sides and a lower pressure in the blade wakes are seen in the static pressure distribution at the diffuser inlet. This is not seen in the measured static pressure due to the measurements averaging the pressure in time. On the other hand, the unsteady static pressure measurements show this phenomena (see chapter 6.6). The numerical

Table 3: Calculated and measured total-total pressure ratio and isentropic efficiency of the impeller at various constructions.

	π_{t-t} [-]		η_{ist-t} [-]	
	CFD	Measured	CFD	Measured
VNL low flow	2.17	2.00	1.176	1.006
VNL design flow	2.01	1.83	1.200	1.052
VNL high flow	1.67	1.64	1.093	0.963
VNL pinch hub 5%	1.99	-	1.198	-
VNL pinch shroud 5%	1.99	-	1.200	-
VNL pinch hub & shroud 5%	1.98	-	1.187	-
VNL pinch hub 10%	2.01	-	1.198	-
VNL pinch shroud 10%	1.98	-	1.198	-
VNL pinch hub & shroud 10% low	2.15	2.04	1.178	1.006
VNL pinch hub & shroud 10% design	1.97	1.88	1.197	1.064
VNL pinch hub & shroud 10% high	1.70	1.68	1.114	0.977
LSVD 7 NACA	1.95	-	1.160	-
LSVD 9 NACA low flow	1.96	2.01	1.081	0.994
LSVD 9 NACA design flow	1.95	1.87	1.180	1.053
LSVD 9 NACA high flow	1.66	1.68	1.060	1.036
LSVD 11 NACA	1.93	-	1.188	-
LSVD 9 flatplate	1.99	-	1.190	-
LSVD 9 const. prof.	1.95	-	1.177	-

results show that the pinch decreases the pressure variation caused by the blade wakes. The pinch made to the hub wall does not decrease the pressure variation caused by the blade wakes as much as the other pinch configurations. The pressure variation is increased at the off-design conditions. The influence of the pinch is small. However, the static pressure variations are slightly smaller with the pinched diffuser at high flow.

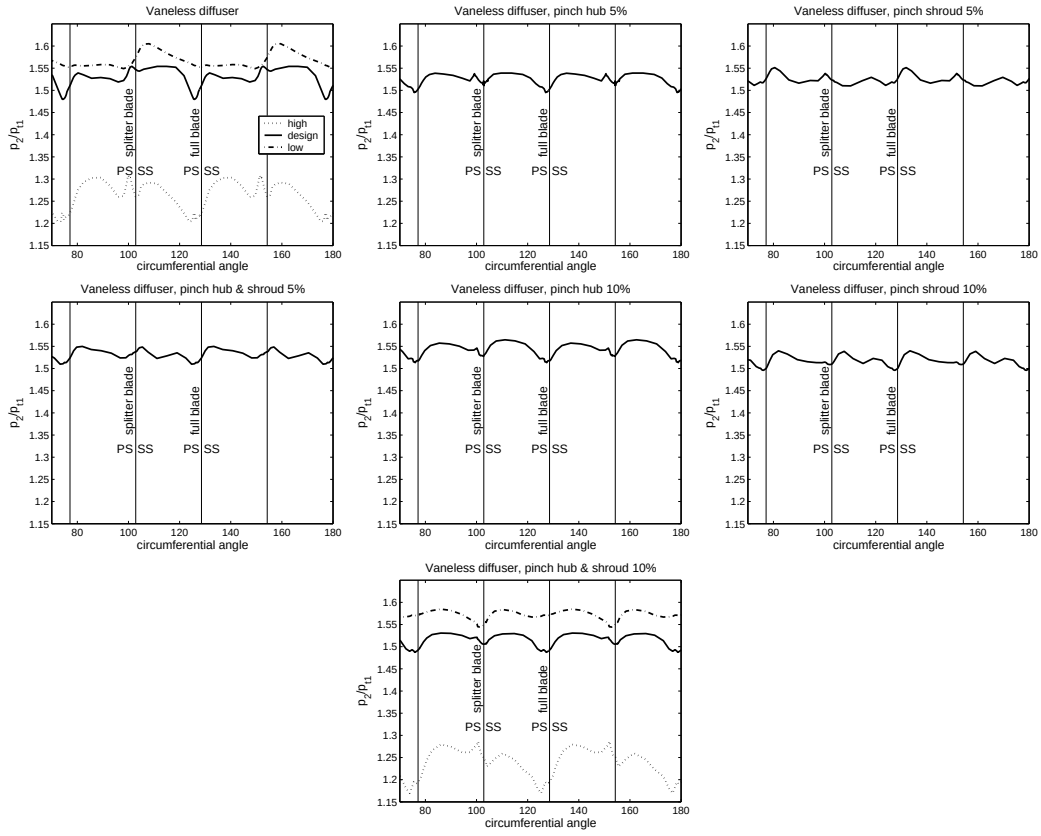

Figure 11: Circumferential variation of static pressure at the diffuser inlet in vaneless diffusers.

The circumferential static pressure distribution at the diffuser outlet at the radius ratio $r/r_2 = 1.67$ in the vaneless diffusers is shown in figure 12. A fairly constant distribution is seen at every construction. On the other hand, the largest variation is seen with the construction without the pinch.

The radial distribution of the static pressure in the vaneless diffusers is shown in figure 13. It can be seen that the static pressure rise is continuous with the diffusers where the pinch is made at both walls. In the other cases the static pressure rise is not continuous and there are slight variations.

The spanwise total pressure at the diffuser inlet in the vaneless diffusers is shown in figure 14. A total pressure is lower near the walls. A lower total pressure area near the hub is seen in the diffuser without the pinch. This area is larger at the low flow. This lower value of the total pressure at the hub at the low flow can also be seen in the measurements (see figures 44, 45, 46 and 47).

The pinch made to the hub wall decreases the lower total pressure area near

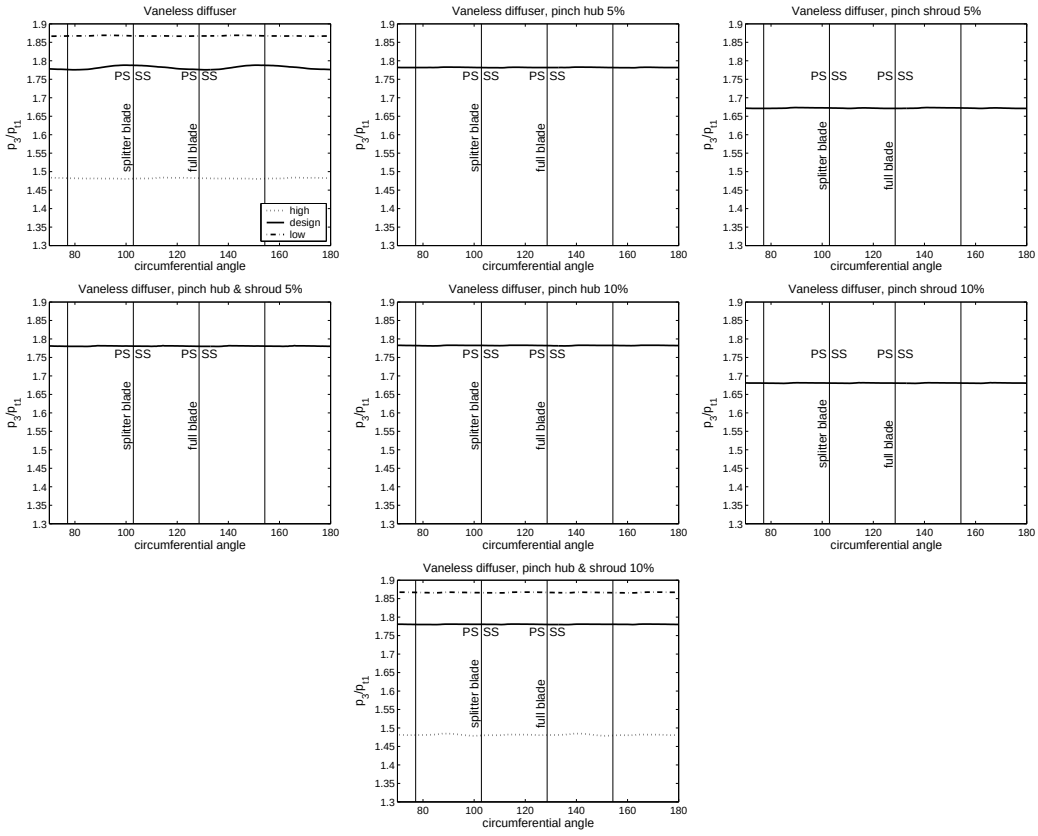

Figure 12: Circumferential variation of static pressure at the diffuser outlet in vaneless diffusers.

the hub and produces the highest value of the total pressure near the hub. An area of lower total pressure value is seen near the shroud.

The pinch made to the shroud also decreases the lower total pressure area near the hub but not as much as the pinch made to the hub. It does not produce a lower total pressure area near the shroud as the pinch made to the hub. The highest total pressure is seen near the hub. The diffuser with 5% pinch made to the hub and to the shroud wall has a similar effect to the total pressure.

A 10% pinch made to the hub and to the shroud wall decreased the lower total pressure area near the shroud. The change is similar to the pinch made to the hub wall. The total pressure is highest near the hub. A lower total pressure area is seen at the shroud at low flow.

The spanwise total pressure at the diffuser outlet at the vaneless diffusers are shown in figure 15. The total pressure is higher near the shroud in the diffuser without the pinch, with the 5% and 10% pinch made to the shroud and the 5%

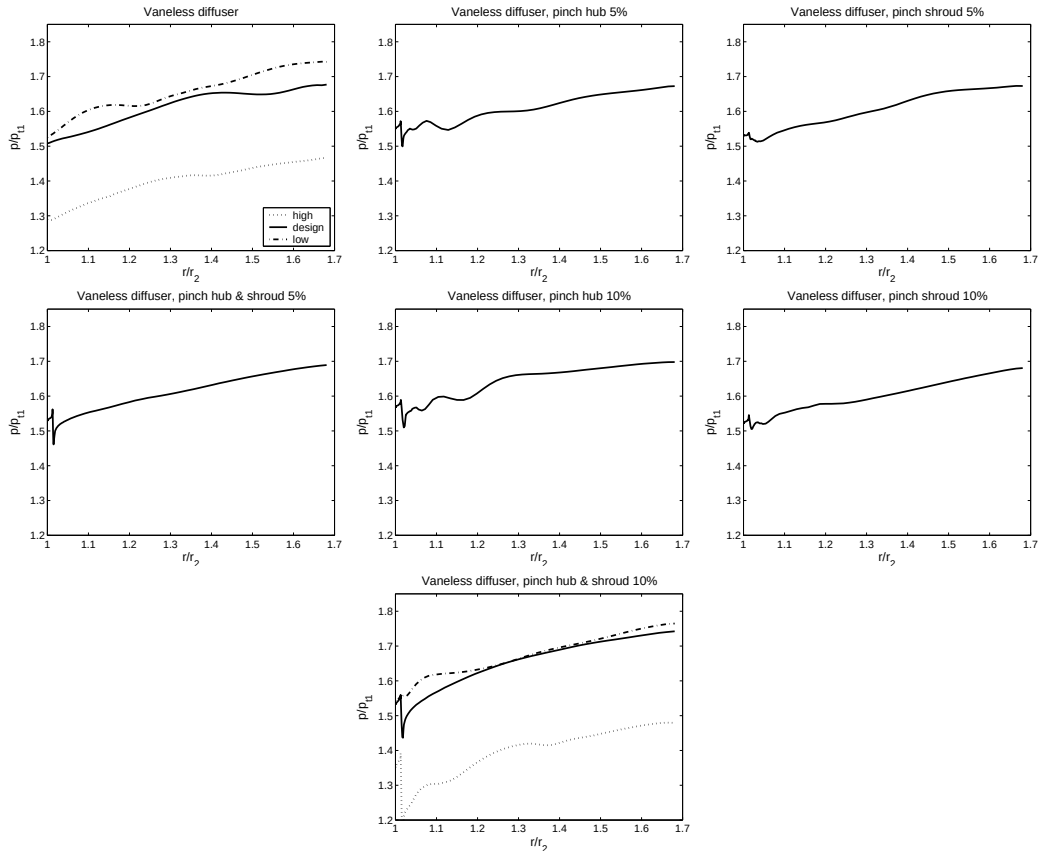

Figure 13: Radial distribution of static pressure in vaneless diffusers.

pinch made to the hub and to the shroud wall. The total pressure is higher near the hub in the diffuser with the 5% and 10% pinch made to the hub and the 10% pinch made to the hub and to the shroud. The 10% pinch made to the hub and to the shroud wall has a minor effect to the spanwise total pressure at high flow. At the low flow the higher total pressure is seen at the hub, whereas the spanwise total pressure is quite constant with the diffuser without the pinch.

Figure 16 shows the circumferential variation of the total pressure at the diffuser inlet radius ratio $r/r_2 = 1.048$ in the vaneless diffusers. It can be seen that the effect of the pinch is minor. The higher pressures caused by the rotor blades are visible in all cases. The 10% pinch made to the hub and to the shroud has a slightly different circumferential total pressure distribution than in the other cases. The total pressure has two narrower peaks compared to the other cases. This kind of difference is not seen in the off-design conditions.

Figure 17 shows the circumferential variation of the total pressure at the dif-

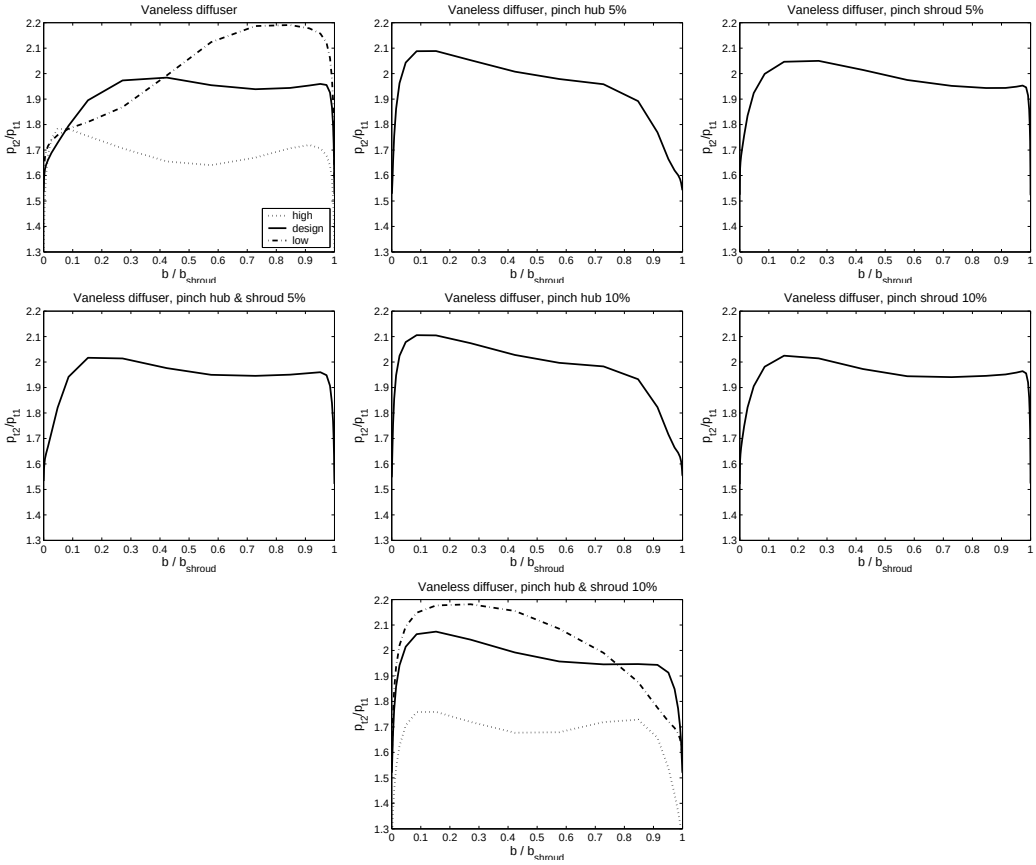

Figure 14: Spanwise distribution of total pressure at the diffuser inlet in vaneless diffusers.

fuser outlet radius ratio $r/r_2 = 1.67$ in the vaneless diffusers. The pressure variations are decreased compared to the diffuser inlet (figure 16). It can be seen that the pinch decreases the circumferential variation compared to the diffuser without the pinch. Therefore can it be concluded that the pinch increases the mixing taking place in the diffuser. The smallest variation is seen with the diffusers where the pinch is made to the hub and to the shroud walls and the 10% pinch at the shroud wall. The circumferential total pressure variation is smaller in the off-design condition in the diffuser without the pinch. The variation is smaller at high flow than low flow. The total pressure variation in the pinched diffuser is slightly higher in the off-design condition than in the design condition.

Figure 18 shows the circumferential variation of the static pressure at the diffuser inlet radius ratio $r/r_2 = 1.048$ in the low solidity vaned diffusers. Wakes and higher pressure at the impeller blades are not visible. However, the effect of

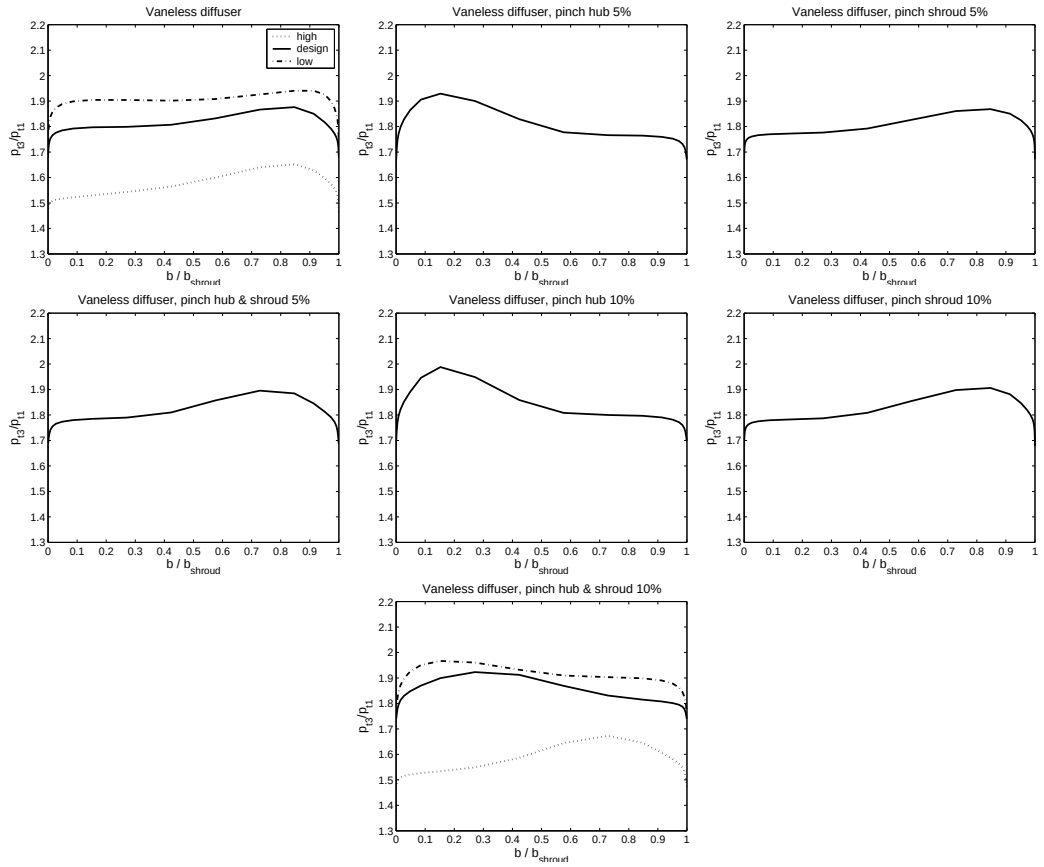

Figure 15: Spanwise distribution of total pressure in diffuser outlet at the vaneless diffusers.

the diffuser vanes is seen. This indicates that the diffuser vanes have an effect upstream. It can be seen that the circumferential variation of the static pressure is larger with the low solidity vaned diffuser with the constant thickness profile. Also the greater number of vanes slightly decreases the variation of the static pressure.

Figure 19 shows the circumferential variation of the static pressure at the diffuser outlet radius ratio $r/r_2 = 1.67$ in the low solidity vaned diffusers. The wakes from the low solidity vanes are seen. The amplitude of the static pressure variation is smaller at the diffuser outlet than at the diffuser inlet. The amplitude of the static pressure variation is smallest with the circular arc vanes and the constant thickness profile. It is also seen that the greater the number of vanes, the smaller the variation of the static pressure is.

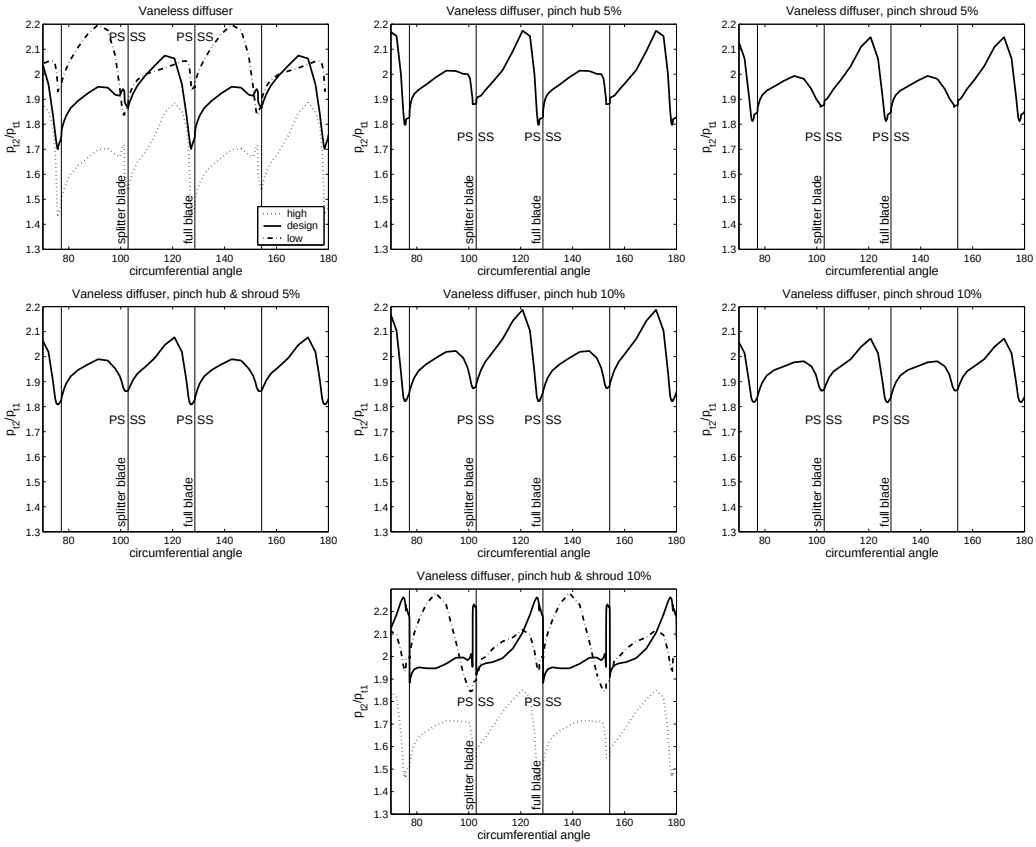

Figure 16: Circumferential distribution of total pressure at the diffuser inlet in vaneless diffusers.

Figure 20 shows the radial distribution of the static pressure in the low solidity vaned diffusers. The static pressure rise is high at the vaneless space before the diffuser vanes, and after the vane trailing edge the static pressure rise is minimal. This kind of behaviour can also be seen in the measurements (see figure 41). The static pressure decreases straight after the leading edge of the vanes in the constant thickness profile constructions.

The spanwise total pressure distribution at the diffuser inlet in the low solidity vaned diffuser are shown in figure 21. The total pressure distribution is similar in each low solidity vaned construction. The total pressure is slightly higher near the hub and lower at the walls. A higher total pressure near the hub can also be seen in the measurements at the design and high flow (see figures 44, 45, 46 and 47). The lower total pressure, which can be seen at the shroud at the low flow in the measurements, is not seen in the figure 21. This can be due to the compressor is already stalled at the low flow operation point simulated with the CFD, and

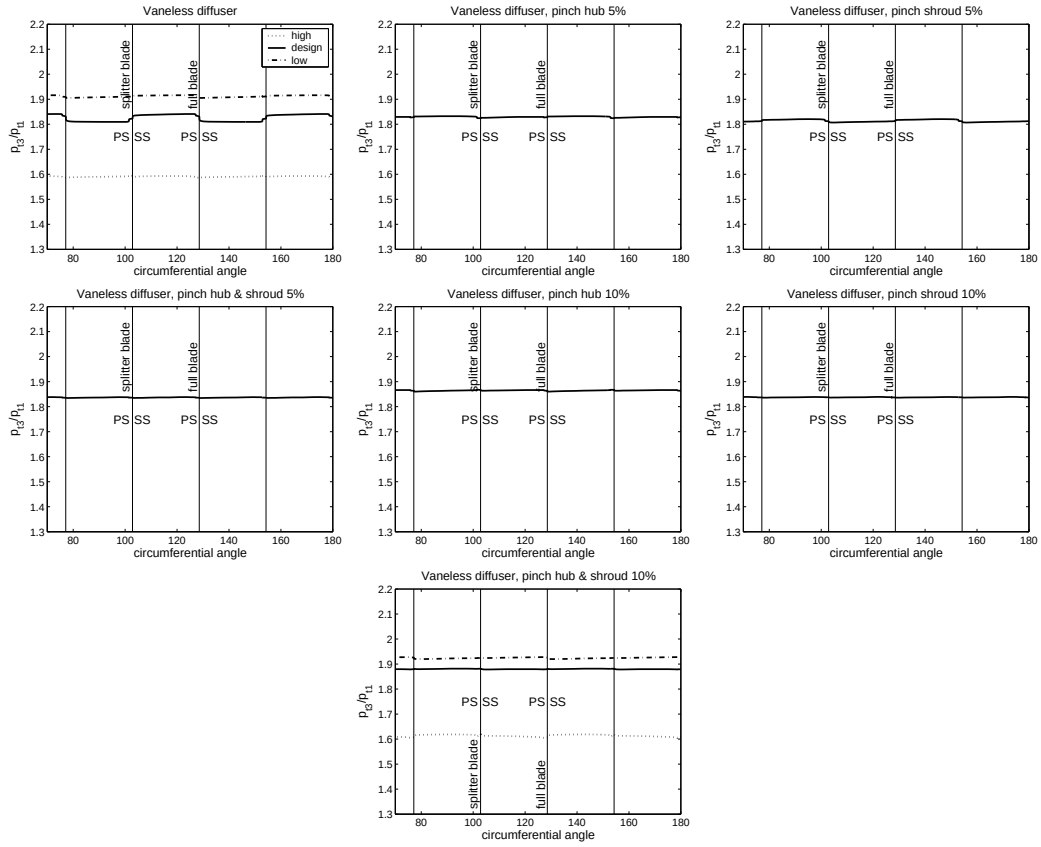

Figure 17: Circumferential distribution of total pressure at the diffuser outlet in vaneless diffusers.

therefore the flow field can not be properly modelled.

The spanwise total pressure distribution at the diffuser outlet in the low solidity vaned diffusers is shown in figure 22. The total pressure distribution is constant in the low solidity diffuser with 9 vanes and the NACA profile. The total pressure is highest near the hub in the flat plate construction. The total pressure is highest also in the other constructions at the hub but not as clearly as with the flat plate construction.

Figure 23 shows the circumferential distribution of the total pressure at the diffuser inlet in the low solidity vaned diffusers. The effect of the rotor is not seen, but the influence of the diffuser vanes is visible as it was in the static pressures (figure 18). The amplitude of the total pressure is highest in the low solidity vaned diffusers with the constant thickness distribution. It can also be seen that the greater number of vanes slightly decreases the amplitude of the total pressure variations.

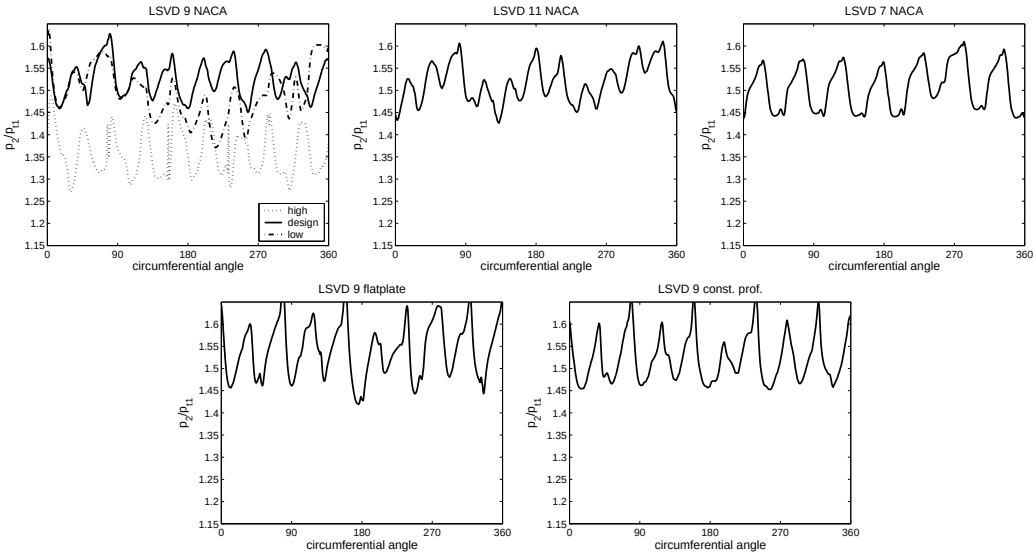

Figure 18: Circumferential distribution of static pressure at the diffuser inlet in low solidity vaned diffusers.

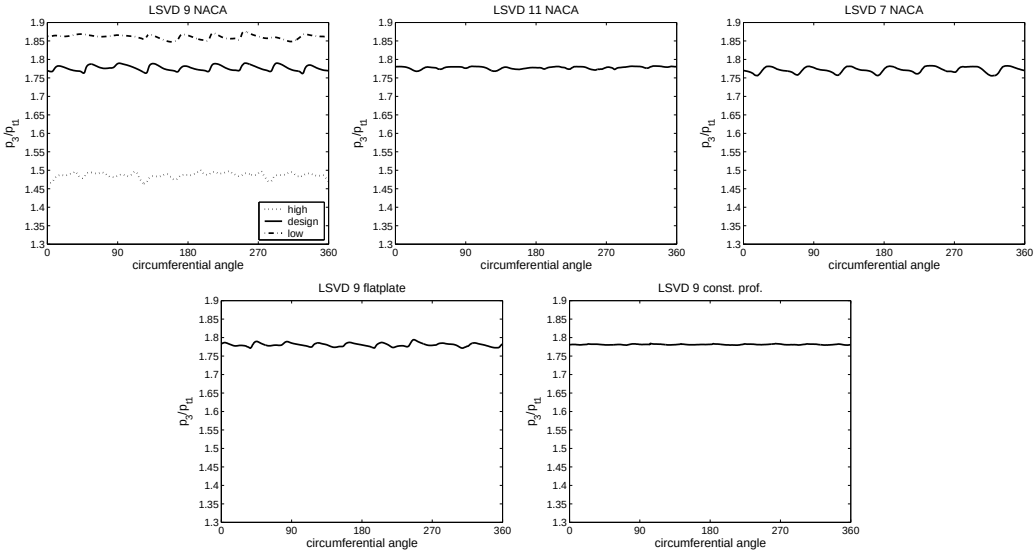

Figure 19: Circumferential distribution of static pressure at the diffuser outlet in low solidity vaned diffusers.

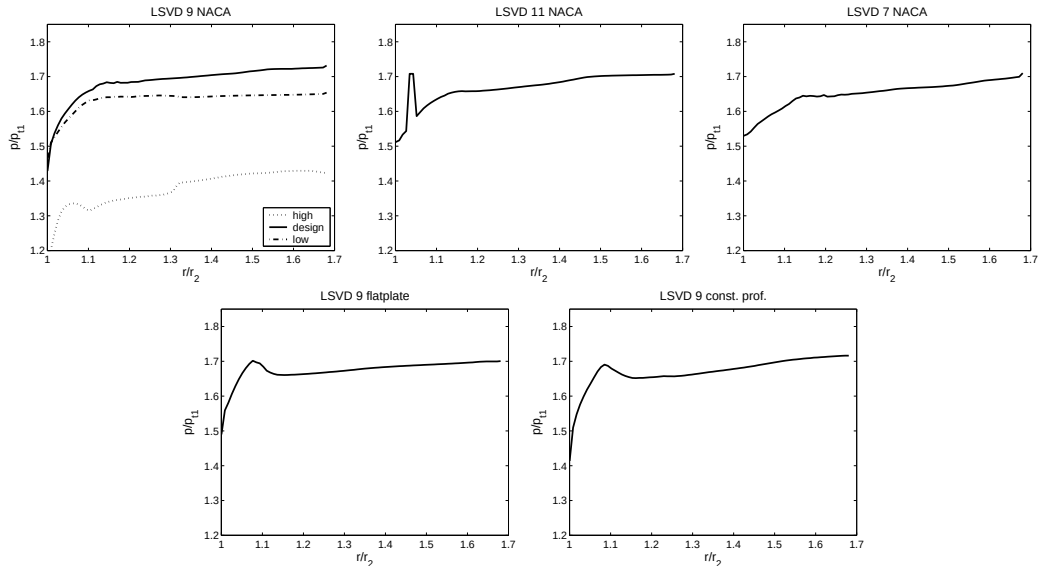

Figure 20: Radial distribution of static pressure in low solidity vaned diffusers.

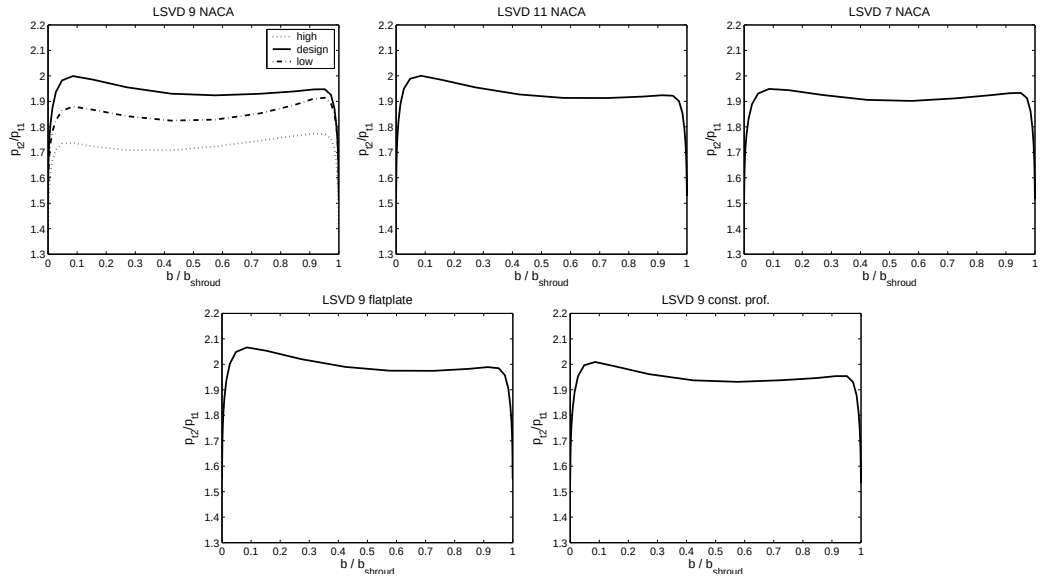

Figure 21: Spanwise distribution of total pressure at the diffuser inlet in low solidity vaned diffusers.

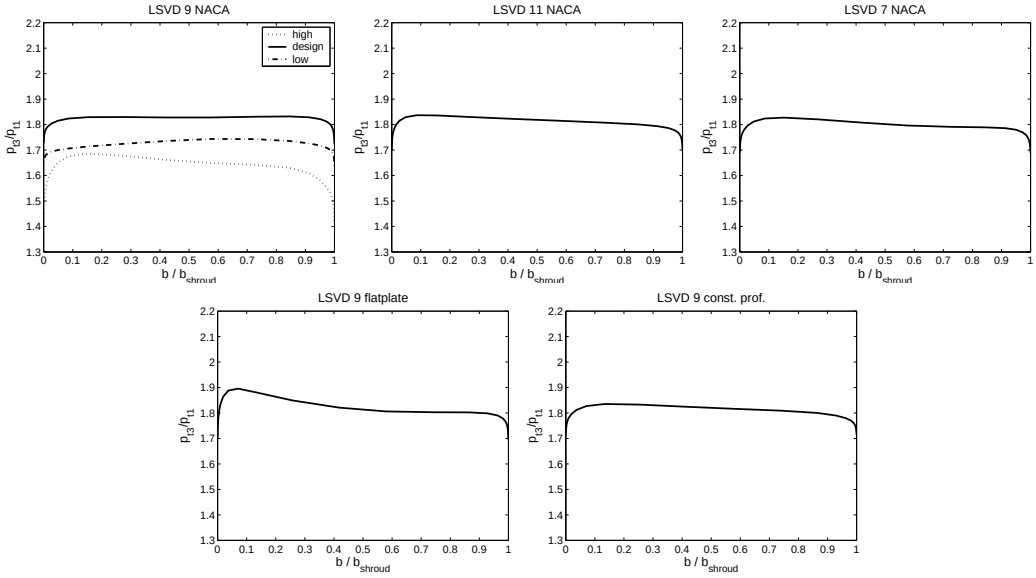

Figure 22: Spanwise distribution of total pressure at the diffuser outlet in low solidity vaned diffusers.

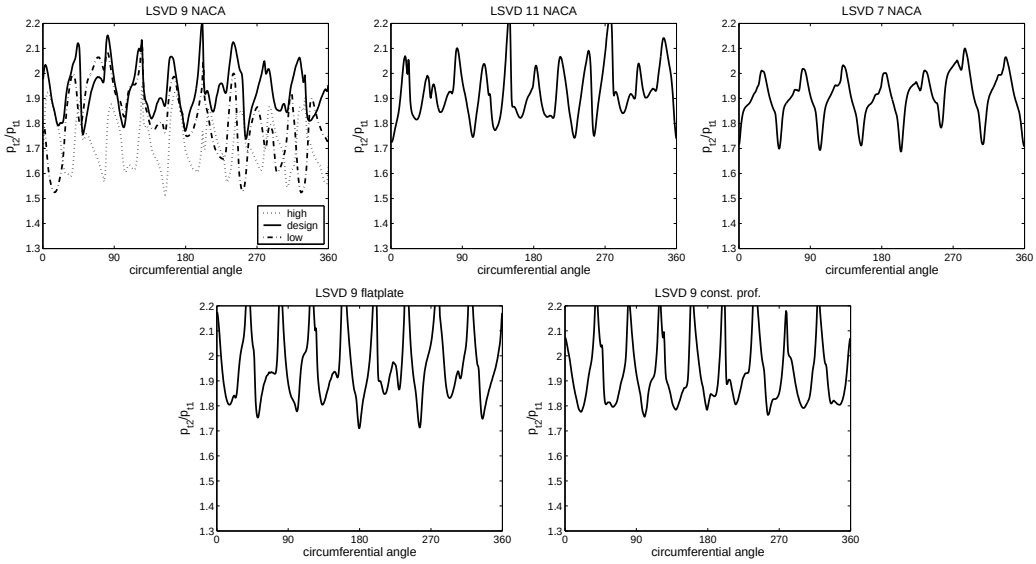

Figure 23: Circumferential distribution of total pressure at the diffuser inlet in low solidity vaned diffusers.

Figure 24 shows the circumferential distribution of the total pressure at the diffuser outlet in the low solidity vaned diffusers. The wakes from the diffuser vanes are seen as they were seen in the static pressure (see figure 19). Also in the total pressure the smallest amplitude is seen in the low solidity vaned diffuser with the circular arc vane and the constant thickness distribution.

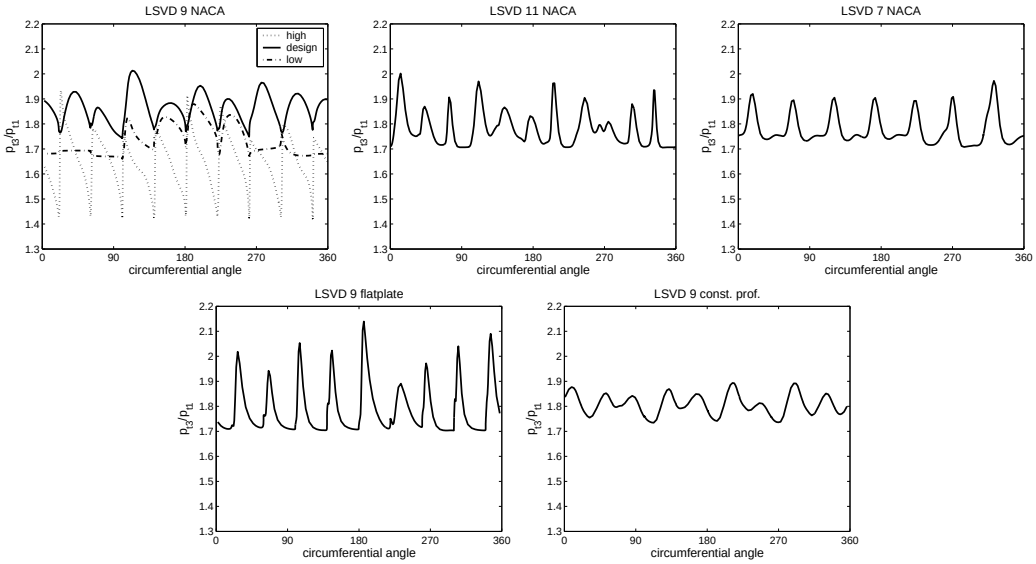

Figure 24: Circumferential distribution of total pressure at the diffuser outlet in low solidity vaned diffusers.

4.4 Overall performance of the diffusers

The overall performance of the diffusers were evaluated using the static pressure recovery coefficient and the total pressure loss coefficient. The static pressure recovery coefficient is defined as

$$C_{pr} = \frac{p_{out} - p_{in}}{p_{tin} - p_{in}} \tag{34}$$

and the total pressure loss coefficient as

$$K_p = \frac{p_{tin} - p_{tout}}{p_{tin} - p_{in}} \tag{35}$$

where p_{tin} and p_{in} are the total and the static pressures at the inlet of the component under evaluation and p_{tout} and p_{out} are the total and static pressures at the outlet of the component under evaluation.

The total pressure loss and the static pressure rise coefficients calculated from the CFD and the measured results are shown in table 4 (the measured results are discussed more detail in chapter 6.5 and are presented in order to verify CFD results). The numerical simulation under-predicts the performance at the low and design flow and over-predicts at the high flow. It can be seen that the pinch made to the hub wall renders a lower losses for the diffuser than the pinch made to the shroud wall. However, the static pressure rise is larger with the pinch made to the shroud wall. It is also seen that the pinch made to both walls renders the best performance of the vaneless diffuser. This can be seen with both 5% and 10% pinches. The larger pinch is better than the smaller one. The smallest losses are seen at the high flow in the CFD results, whereas the smallest losses are seen at the design flow in the measured results. This can be explained by the fact that the volute is not modelled in the CFD simulations.

The same kind of trend is seen in the total pressure loss and the static pressure rise coefficients as was seen in the isentropic efficiency at the low solidity vaned diffusers (see table 2). The greater number of vanes leads to a better performance of the diffuser. Also the low solidity vaned diffuser with the circular arc chamber line and the NACA thickness profile have a better performance than the constant thickness profile low solidity vaned diffusers. Contrary to the isentropic efficiency results, the low solidity vaned diffusers with the circular arc chamber line and the constant thickness profile have a better diffuser performance than the low solidity vaned diffusers with the straight line chamber line and the constant thickness profile (flatplate).

Table 4: Calculated and measured total pressure loss and static pressure rise coefficients of diffusers .

	K_p [-]		C_{pr} [-]	
	CFD	Measured	CFD	Measured
VNL low flow	0.392	0.224	0.306	0.480
VNL design flow	0.346	0.171	0.340	0.517
VNL high flow	0.148	0.201	0.538	0.436
VNL pinch hub 5%	0.244	-	0.342	-
VNL pinch shroud 5%	0.315	-	0.350	-
VNL pinch hub&shroud 5%	0.239	-	0.396	-
VNL pinch hub 10%	0.171	-	0.362	-
VNL pinch shroud 10%	0.217	-	0.387	-
VNL pinch hub&shroud 10% low	0.330	0.227	0.358	0.462
VNL pinch hub&shroud 10% design	0.163	0.145	0.526	0.504
VNL pinch hub&shroud 10% high	0.161	0.146	0.511	0.425
LSVD 7 NACA	0.273	-	0.459	-
LSVD 9 NACA low flow	0.380	0.327	0.375	0.557
LSVD 9 NACA design flow	0.236	0.123	0.494	0.641
LSVD 9 NACA high flow	0.203	0.339	0.226	0.339
LSVD 11 NACA	0.150	-	0.401	-
LSVD 9 flatplate	0.291	-	0.398	-
LSVD 9 const. prof.	0.275	-	0.491	-

4.5 Unsteady flow fields in vaneless diffusers

The unsteady study is made to the other compressor. Details of the used compressor is presented in chapter 5.1. The calculated pressure spectra at the diffuser inlet are presented in figure 25. The results from the design operation point, the operation point near the choke and the different circumferential angles are shown. The pressure variation at the blade passing frequency and at the frequency of every second blade is clearly visible at the design operation point. The amplitude of the pressure variation is largest at the circumferential angle $168°$ and at the frequency of every second blade. The magnitude of the amplitude is the same in the measured and in the calculated pressure spectrum at the frequency of every second blade. On the other hand, pressure variation is not seen in the measured spectrum at the blade passing frequency (see figure 66).

There are larger pressure variations at the multiplex frequency of the rotation speed at the operation point near the choke. The largest amplitude of pressure variations is seen at the frequency of every second blade and at the circumferential angles $78°$ and $348°$. These are not seen in the measured pressure spectra (see figure 66). A larger amplitude of the pressure variations is also seen at the blade passing frequency in the calculated spectra. This can also be seen in the measured

spectra at the circumferential angles $168°$ and $348°$. These results indicate that the pressure rise in every second blade passage is higher than in the others.

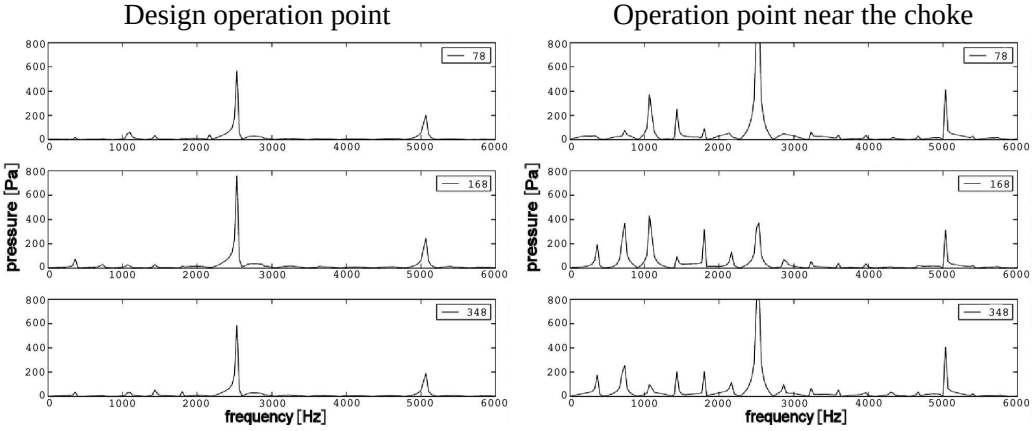

Figure 25: Calculated pressure spectra at different circumferential angles at the diffuser inlet.

The calculated pressure spectra at the diffuser outlet are presented in figure 26. The results from the design operation point, the operation point near the choke and the different circumferential angles are shown. Pressure variation can be seen at the passing frequency of every second blade at the design operation point. The amplitude of the pressure variation decreases when the circumferential angle increases. The magnitude of the pressure variation in the measured data is equal to the magnitude of the pressure variation in the calculated data at the circumferential angles $168°$ and $348°$ (for measured data see figure 67). A small amplitude of pressure variation is also seen both in the measured and in the calculated data at the blade passing frequency. The amplitude of the pressure variation is attenuated in the diffuser but the decrement is quite small compared to the decrement in the measured pressure variation.

At the operation point near the choke the behaviour of the pressure is similar to the one at the diffuser inlet. Only the amplitude of the pressure variations is smaller. The calculated data shows a large amplitude of pressure variations at the frequency of every second blade at the circumferential angles $78°$ and $348°$, which are not seen in the measured pressure spectra (see figure 67).

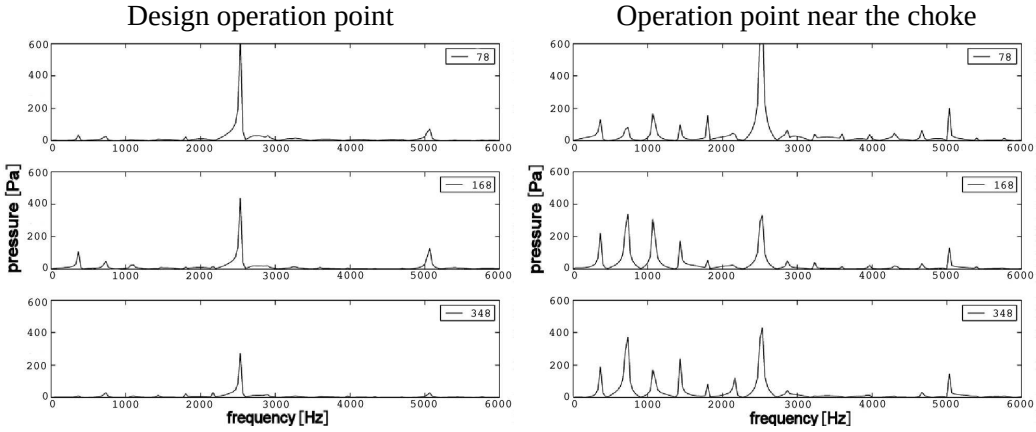

Figure 26: Calculated pressure spectra at different circumferential angles at the diffuser outlet.

4.6 Concluding remarks

Seven different vaneless diffuser geometries and five different low solidity vaned diffuser geometries were analyzed numerically. The pinches made to the hub, to the shroud, or to both walls were analyzed. The pinch was 5% and 10% of the height of the unpinched diffuser. The effect of the vane shape and the number of vanes were analyzed. Also the whole compressor was modelled with the vaneless diffuser, and a time-accurate numerical simulation was conducted in order to analyze the unsteady phenomena in the diffuser.

It was seen that the total-total pressure ratio was fairly well predicted compared to the measured values at all constructions. This was seen especially at low and high flow. The isentropic efficiency was clearly over-predicted in all cases. The magnitude of the difference was same at all operation points. Improved efficiency of the pinched. The nearly correct pressure ratio and the clearly over-predicted isentropic efficiency indicates that the temperature rise was under-predicted.

The pinch made to the hub or to the shroud affected only slightly the isentropic efficiency. The case where the 10% pinch is made to the hub and to the shroud walls showed a better isentropic efficiency. The results showed that the pinch made to one wall of the diffuser was not as efficient as the pinch made to both walls.

Also different kinds of low solidity vaned diffusers were analyzed numerically. It could be seen that the vane with the circular arc chamber line and the NACA profile showed the best isentropic efficiency.

The numerical results showed that the pinch decreased the static pressure vari-

ation caused by the blade wakes and the higher pressure from the pressure side of the blades. The differences between different pinches were minor. Wakes and higher pressure at the impeller blades were not seen with the low solidity vaned diffusers. The effect of the diffuser vanes could be seen, however.

Lower total pressure areas could be seen near the walls. A lower total pressure area near the hub was seen in the diffuser without the pinch. This area was larger at the low flow. This kind of behaviour of the total pressure was also seen in the measurements. The pinched diffusers decreased the lower total pressure areas near the diffuser walls.

The numerical simulation under-predicted the performance of the diffuser at the low and design flow and over-predicted at the high flow. The pinch made to the hub wall gave a better performance of the diffuser than the pinch made to the shroud wall. It could also be seen that the pinch made to both walls further improved the performance. The larger vane number led to a better performance of the diffuser. Also the low solidity vaned diffuser with the circular arc chamber line and the NACA thickness profile had a better performance than the constant thickness profile low solidity vaned diffusers.

The time-accurate calculations showed quite a good agreement with the measured data. The agreement was very good at the design operation point, even though the computational grid was not dense enough in the volute and in the exit cone. The time-accurate calculation over-predicted the amplitude of the pressure variations at the high flow.

5 Experimental setup

5.1 Test compressors

Two test compressors were used. Different diffuser geometries were studied with one compressor, and unsteady analysis was made with the other.

The different diffusers were studied with a centrifugal compressor designed to be used in water-treatment plants (Larjola et al. 2000 and Larjola 2000). The pressure ratio π_{t-t} of the compressor is 1.94 at the design point. A photo of the compressor is shown in figure 27. The compressor was driven directly by a

Figure 27: Test compressor used in studying different diffusers.

high speed electric motor. The electric motor was accurately controlled by an inverter. Because of the single shaft construction there is no gear box, and magnetic bearings are used, which makes the compressor totally oil-free. The unshrouded impeller has seven full and seven splitter blades with $40°$ back lean from the radial direction.

The unsteady investigation was made with a centrifugal compressor originally designed to produce a vacuum for paper and pulp mills. A photo of the compressor is shown in figure 28. The compressor produces the pressure ratio $\pi_{t-t} = 2.0$ at the design point. Single shaft construction and magnetic bearings are also used in this compressor. The electric motor is 175 kW and the inverter 200 kW. The impeller is unshrouded and has seven full and seven splitter blades with backward leaning angle $30°$ from radial direction. The diffuser of the compressor is vaneless

and there is no pinch. The radius ratio $\frac{r_4}{r_2} = 1.90$ and the height are constant. The vaneless diffuser is followed by the circular cross-section volute (Reunanen 2001).

Figure 28: Test compressor used to investigate unsteady phenomena.

5.2 Investigated diffuser geometries

5.2.1 Original diffuser

The original diffuser is a simple parallel wall vaneless diffuser. There is no pinch. The diffuser passage height is constant over the radius ratio and the height is wider than the impeller passage at the trailing edge by the amount of the tip clearance. The outlet radius ratio of the diffuser is $\frac{r_4}{r_2} = 1.68$.

5.2.2 Pinched diffuser

The pinched diffuser is pinched from the hub and the shroud walls. The height of the diffuser has been decreased by 10% from the original diffuser height. The radius ratio $\frac{r_4}{r_2}$ of the diffuser is the same as in the original diffuser. Figure 29 shows the layout of the pinched diffuser geometry.

5.2.3 Low solidity vaned diffuser

Different kinds of low solidity vaned diffusers were first tested with the help of CFD calculations. On the basis of the results of CFD the one LSVD was manu-

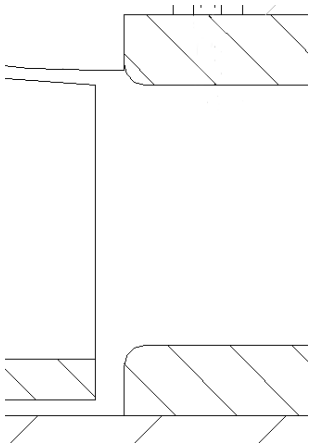

Figure 29: Layout of pinched diffuser geometry.

factured and experimentally investigated. The geometrical parameters of the designed LSVD are shown in table 5. Figure 30 shows the layout and a photo of the analyzed LSVD.

Table 5: LSVD geometrical parameters

name	$\frac{b_{2'}}{b_2}$	σ	$\frac{r_{2'}}{r_2}$	$\frac{r_3}{r_2}$	$\frac{r_4}{r_2}$	N	θ	i
LSVD 9 NACA	1.00	0.65	1.1	1.319	1.681	9	$10°$	$-2°$

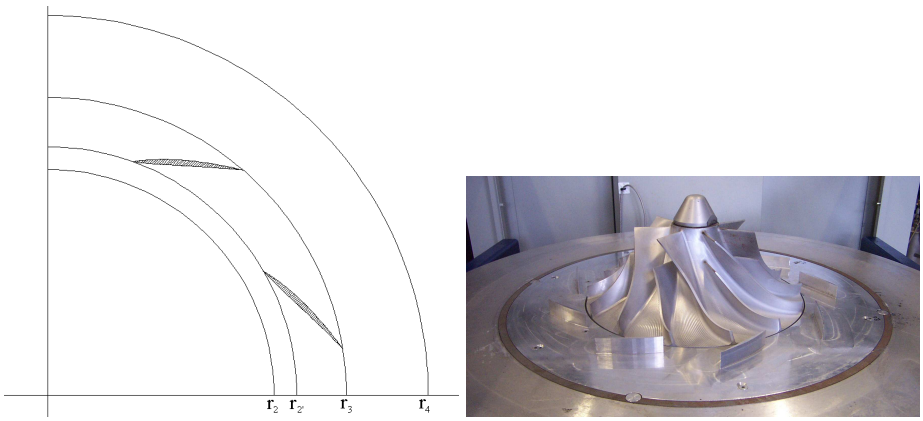

Figure 30: Layout and photo of low solidity vaned diffuser geometry.

5.3 Steady measurements and data acquisition

5.3.1 Compressor test stand

The measurements were conducted in the Laboratory of Fluid Dynamics at Lappeenranta University of Technology. Both compressors were tested at the same open air loop test stand. The layout of the compressor test stand is shown in figure 31. The air entered the test compressor through a mass flow nozzle, throttling valve A and flow straightener. The mass flow nozzle is an ISA 1932 nozzle made according to DIN 1952 and it is placed at the beginning of the inlet pipe according to VDI 2045. The inlet pressure and temperature were measured. Also ambient pressure, temperature and humidity were measured. The pressure and the temperature were measured after the compressor and the flow passes through throttling valve B and the muffler. The outlet pipe of the test stand was insulated to ensure correct temperature measurement. To measure the vacuum compressor valve B was fully open and valve A was used to throttle the compressor. To measure the overpressure compressor valve A was fully open and valve B was used to throttle the compressor.

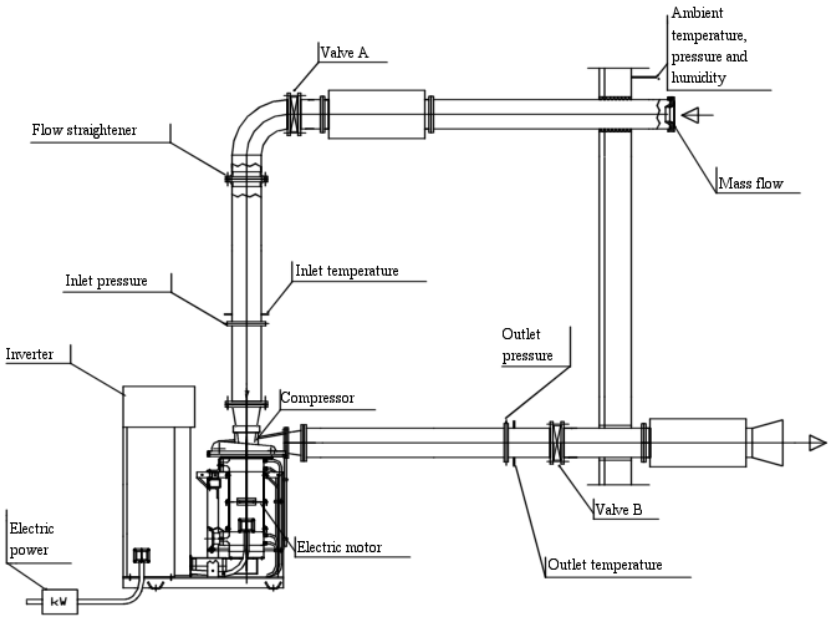

Figure 31: Layout of the test stand.

The test stand was used to measure the overall performance of the compressor. The analogue signals from the thermoelements, pressure transducers, humidity meter, tachometer and power analyzer were collected into a Fluke Hydra data

logger. The data logger was connected to a PC. The measured data were analyzed on-line with an in-house developed data acquisition program and the necessary data was recorded. The performance calculations and the instrumentation of the test stand were made according to the following standards: ISO 5389, ASME PTC 10, VDI 2045 Part 1 and VDI 2045 Part 2.

5.3.2 Pressure and temperature measurements in diffusers

A three-hole cobra-probe and Kiel-probes with thermoelements were used to measure the flow field inside the compressor. All the probes were made by the staff of the Laboratory of Fluid Dynamics. The cobra-probe was calibrated over a broad Mach number range in a free jet nozzle. Before the measurement the cobra-probe was nulled, i.e. turned towards the flow. The Kiel-probes were calibrated over a broad Mach number range and yaw-angle range in the free jet nozzle. Also the recovery factor of the temperature measurement was measured.

Static pressures were measured at four different circumferential angles ($90°$, $180°$, $270°$ and $0°/360°$) at the diffuser inlet ($\frac{d_{in}}{d_2} = 1.036$) and outlet ($\frac{d_{out}}{d_2} = 1.67$). Static pressures were also measured at three different positions ($\frac{d}{d_2} = 1.1$, $\frac{d}{d_2} = 1.26$ and $\frac{d}{d_2} = 1.47$) between the diffuser inlet and outlet at the circumferential angle $180°$. The total pressure and temperature were measured at four different circumferential ($14°$, $104°$, $194°$ and $284°$) angles at the diffuser inlet and outlet. The measurements were done with the Kiel-probes. The flow angles were also measured with the Cobra-probe at the circumferential angle $194°$ at the diffuser inlet and outlet. The locations of the static pressure taps and probe traverses are shown in figure 32 and the instrumented compressor is shown in figure 33. These measurements were done with design rotation speed and three different mass flows (see figure 35).

The axial location of the impeller was measured. The measurements were made with Micro-Epsilon's non-contact displacement-sensor ES2. It is capable to measure distances from 0 mm to 2 mm. The displacement-sensor was assembled at the circumferential angle $90°$ and under the impeller at the diameter ratio $\frac{d_{sensor}}{d_2} = 0.969$. Axial location was measured in order to define the location of the impeller versus the location of the diffuser walls.

5.4 Unsteady measurements and data acquisition

5.4.1 Unsteady pressure transducer

The unsteady static pressure measurements were made with a Kulite XTC-190 pressure transmitter. The transmitter is flush mounted to the shroud wall at the diffuser inlet and hub wall at the diffuser outlet. This is caused by the construction

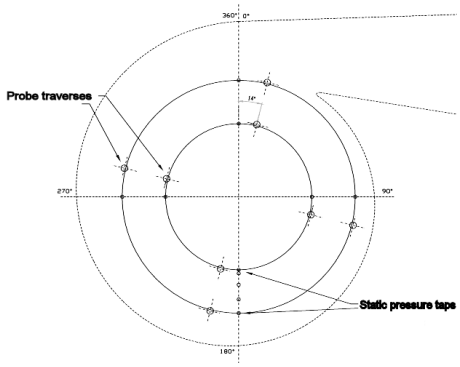

Figure 32: Location of static pressure taps and probe traverses.

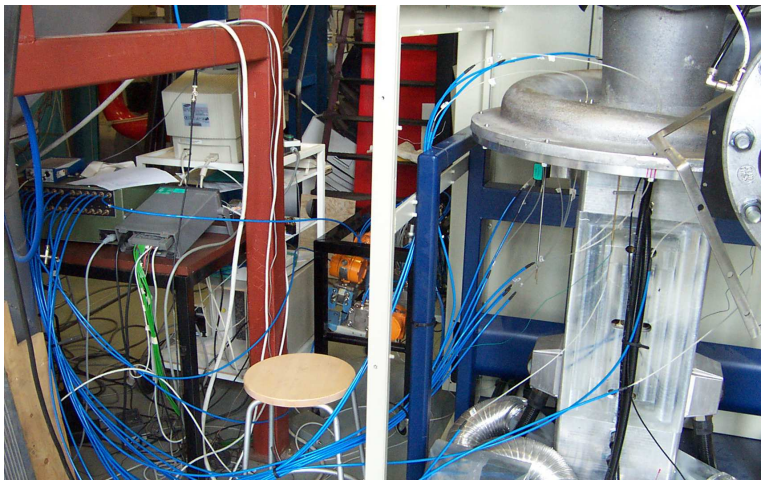

Figure 33: Instrumented compressor and data acquisition system.

of the compressor, which does not allow mounting the transmitter to the same wall at the diffuser inlet and outlet. Flush mounting is used to achieve the best possible frequency response. The unsteady static pressure was measured at three different circumferential angles ($78°$, $168°$ and $348°$) at the diffuser inlet and outlet. The circumferential location $258°$ was left out because it was impossible to measure there due to the compressor mounting. Location of the measuring positions are shown in figure 34

The Kulite transmitter uses piezo-resistors mounted on a silicon diaphragm to measure pressure variations. The diaphragm moves due to the pressure change, and the resistors mounted on the diaphragm change their resistance. The measured voltage changes while maintaining the excitation current constant. Temper-

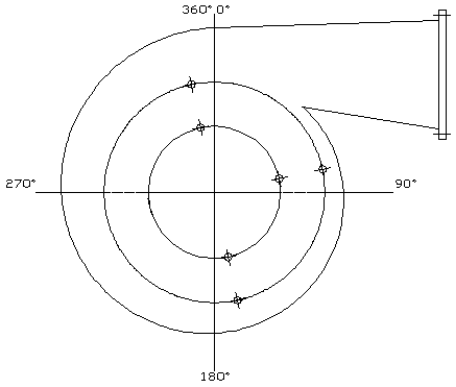

Figure 34: Unsteady pressure transmitter positions and mountings.

ature has been noticed to affect the signal of piezo-resistors (Kupferschmied et al. 2000). The transmitter has a build-in temperature compensation allowing a wide range of measuring temperatures.

Dynamic and static calibration was performed to the transmitter. Dynamic calibration was done with the calibrator described in Japikse (1986) and the static calibration with the Beamex PC 106 calibrator.

5.4.2 Data acquisition and analysis

The signal from the unsteady pressure transducer was collected with a Tektronix oscilloscope connected to a PC. The performance of the compressor, including the rotation speed of the rotor, was monitored and saved at the same time with the in-house developed program described in chapter 5.3.1. The signal was captured with the sampling rate 1 MHz. 30000 data points were collected, which corresponds to a 0.03 s period of time. This is 10.8 rotations of the impeller. Three captures of the data were made at each measuring point and at each operation condition. The measured data was phase averaged over ten rotations of the impeller, and three different measured data were compared to each other to ensure the regularity of the achieved pressure variations. In this case phase averaging means that the 10 impeller rotations-long measured data is cut ten 1-rotation-long pieces with the help of the measured rotation speed. Then the measured pressure data points are averaged at the same position of the impeller. A fast Fourier transform was made to examine the pressure fluctuations in frequency plane. The operation point near the surge, the design operation point and the operation point near the choke were measured. The design rotational speed was used.

6 Experimental results

6.1 Performance map of the compressor

The performance map of the compressor was measured. Six different rotational speeds were used. The lowest speed line was measured first. The measurements were started from the highest mass flow and ended in the lowest mass flow (stall line). After the lowest speed line was measured, the next speed line was measured starting from the highest flow until all speed lines were measured. The temperature was allowed to stabilize for a sufficiently long time at every measured operation point of the compressor. The 50% isentropic efficiency was the criteria of the starting point at the lower rotational speeds, and the power limit of the electric motor at the higher rotational speeds. The pressure ratio was increased when moving to the lower flow at the performance map until the maximum is reached. The stall line of the compressor map was determined to the point were the pressure ratio was decreased for the first time. The operation of the compressor was stable at this point. The compressor would stall if the flow were further throttled.

The reference total pressure p_{t1ref}, total temperature T_{t1ref} and humidity R_{Href} were used to make the performance maps comparable with each other, because the measurements had to be done with different ambient conditions. The reference humidity was used to calculate the specific gas constant R_{ref} at the reference condition. The reference mass flow q_{mref} and the reference rotational speed N_{ref} were calculated as

$$q_{mref} = q_m \frac{p_{t1ref}}{p_{t1}} \sqrt{\frac{T_{t1} R}{T_{t1ref} R_{ref}}} \tag{36}$$

$$N_{ref} = N \sqrt{\frac{T_{t1ref} R_{ref}}{T_{t1} R}} \tag{37}$$

where q_m is the mass flow and N is the rotational speed in actual measuring conditions, and the quantities with subscript ref are the values in the reference conditions.

The operation point of the compressor was evaluated using the reference volume flow and the reference rotation speed of the compressor. Three operation points at the design speed were selected for detailed flow analysis. These points are shown in figure 35. The volume flows of these points are 0.56, 1.00 and 1.34 times design flow and they are called low, design and high flow. It was not possible to run the compressor at the low flow with the low solidity vaned diffuser because the compressor stalled. Therefore the low flow condition with the LSVD is 0.62 times the design flow.

The mass flow, the rotational speed and the isentropic efficiency were made non-dimensional by dividing them with the mass flow, the rotational speed and the

isentropic efficiency of the original geometry at the design point. The measured compressor maps are shown in figures 35, 36 and 37.

The pinched diffuser expanded the area of 1.01 efficiency at all rotational speeds. There is a small area of 1.02 efficiency at the lower rotational speeds. The pinched diffuser increased the efficiencies at the high flow (see figures 35 and 36). The pinched diffuser stabilized flow at the rotational speeds 0.53, 0.70 and 0.82, which slightly moved the surge line to the lower flow. This kind of phenomena was not observed at the higher rotational speeds.

The low solidity vaned diffuser increased the efficiency at the intermediate flow at all rotational speeds (see figures 35 and 37). Also the operation range of the good efficiency was larger with the LSVD than with the vaneless diffuser. The LSVD was designed with the negative incidence to achieve a good operation range and efficiency (Hayami et al. 1990 and Hohlweg et al. 1993). On the other hand, the flow range was narrowed. This can be seen especially at the high flow and lower rotational speed, which is reasonable because the flow is most radial and the incidence angle positive. Also the surge line of the compressor was slightly moved to the higher flow.

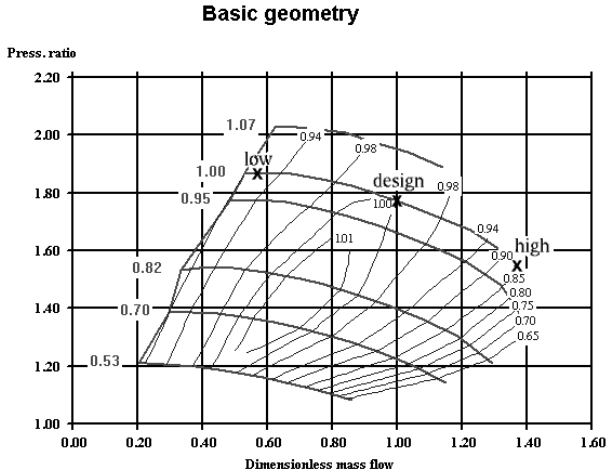

Figure 35: Performance map of the compressor with the original diffuser.

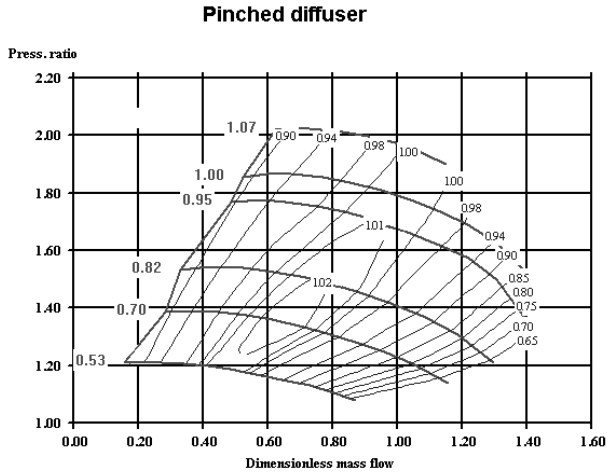

Figure 36: Performance map of the compressor with the pinched diffuser.

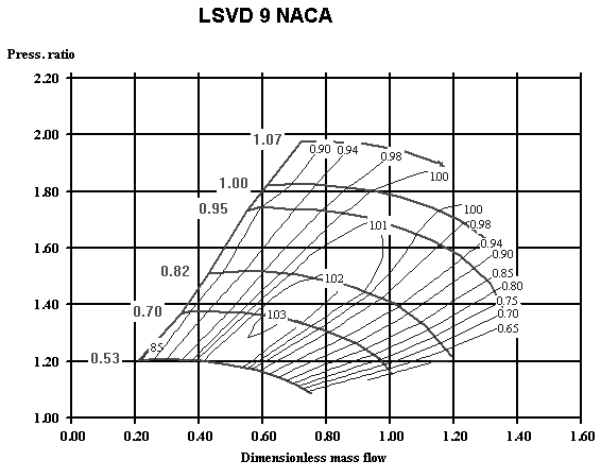

Figure 37: Performance map of the compressor with the low solidity vaned diffuser.

6.2 Isentropic efficiency of the compressor

The total-total isentropic efficiency of the compressor was measured at the same time as the performance map. The uncertainty of the efficiency measurements made for the whole stage is about ± 0.015 times efficiency of the design point in a single measurement (Sallinen 1999).

The isentropic efficiencies of the whole stage at different rotational speeds are shown in figure 38. The pinch was expected to stabilize the flow field and gain better efficiency because the flow path in the diffuser was shorter. On the other hand, the volute was expected to diminish this effect because the flow was more swirling in the volute. Better efficiencies are mainly seen at the higher flow. The higher the rotational speed, the higher the mass flow where the isentropic efficiency is seen to improve. This indicates that the area where the flow is most radial the effect of the pinch to the efficiency is beneficial. The pinch also decreased the efficiency at the higher rotational speed and at the low flow. In this area the flow is most tangential. It was expected that the pinch would increase the efficiency of the diffuser at the whole flow range. Therefore the decreased efficiency at the higher rotational speed and at the low flow can only be explained by decreased efficiency of the volute and/or the rotor. The probe measurements revealed that the impeller efficiency did not change but the performance of the volute weakened (see table 3 and figures 64 and 65).

The LSVD increased the isentropic efficiency at the intermediate flow at all rotational speeds. The largest increment was observed at the low rotational speed. The efficiency was lower at the low flow compared to the vaneless diffuser. This was the case especially at the higher rotational speed where the flow was more tangential. The efficiency was good also at the higher flow and higher rotational speed. This indicates that the LSVD had a good performance over a large variation of incidence but a very large negative or a positive incidence would drop the efficiency. The behaviour of the pinched diffuser and the LSVD was quite similar, which is reasonable because both geometries made the flow more radial in the diffuser.

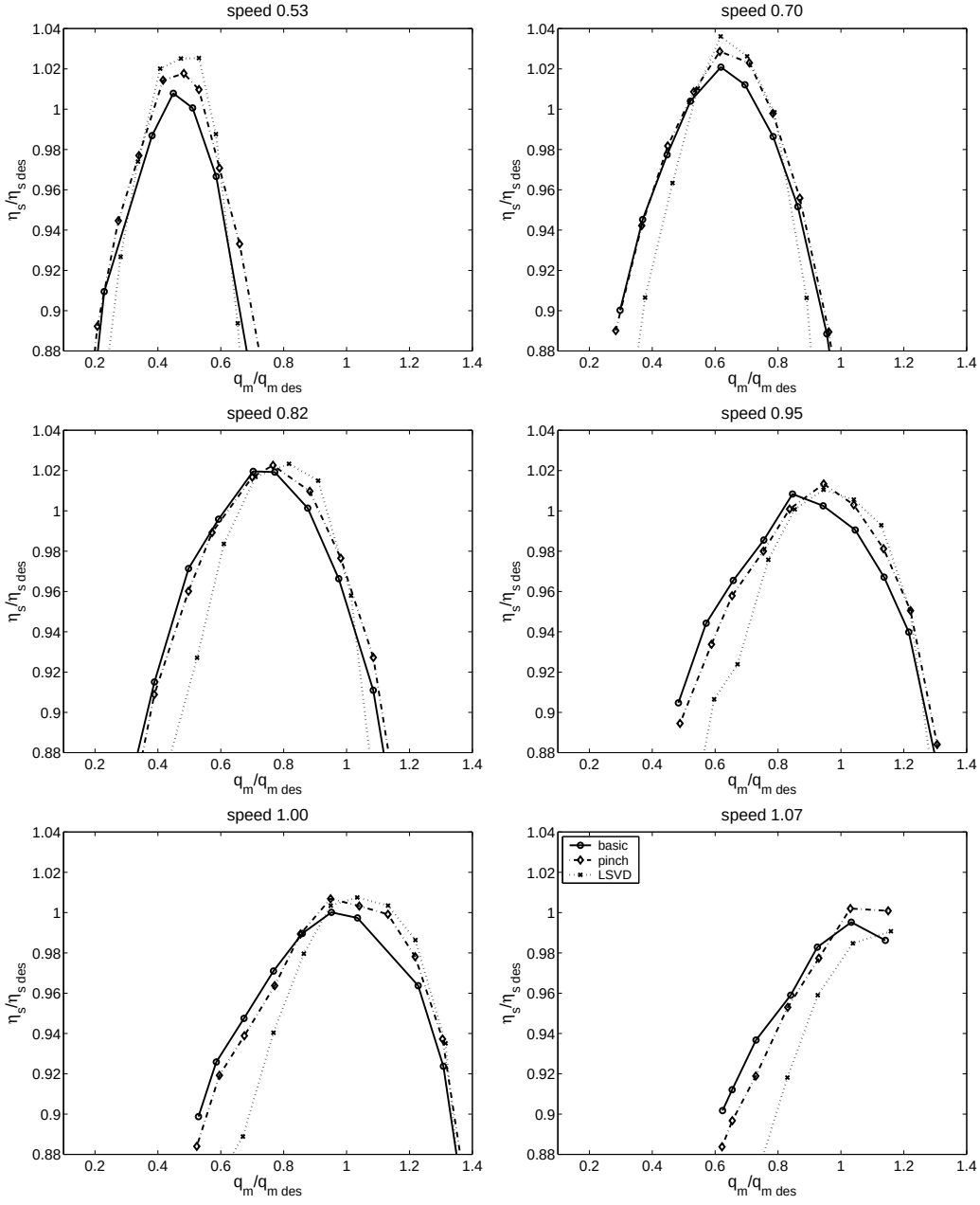

Figure 38: Isentropic efficiency at different rotational speeds

6.3 Static pressure measurements in the diffusers

The static pressure in the diffuser was measured using four pressure taps at the diffuser inlet and outlet. The pressure taps were located at the shroud wall at the diffuser inlet and at the hub wall at the diffuser outlet. Different walls at the diffuser inlet and outlet were used due to the construction of the compressor. The static pressure was also measured at three different radius ratios between the diffuser inlet and outlet. The static pressure was made non-dimensional by dividing it with the total pressure at the compressor inlet. The measurements were done with three different mass flows at the design rotation speed. The static pressure at the diffuser inlet is shown in figure 39. Figure 40 shows the static pressure at the diffuser outlet and figure 41 the static pressure as a function of the radius ratio.

The non-uniformity caused by the volute is clearly seen at the static pressure distributions in the vaneless diffusers. The static pressure decreases along the circumference at the high flow and increases at the low flow. The static pressure distribution is fairly constant along the circumference at the design flow. This can be seen at the diffuser inlet and outlet. However, the pressure rise along the circumference at the low flow is characterized with two wave patterns at the diffuser inlet. This phenomenon is most likely due to the impeller response to the static pressure non-uniformity of the volute tongue. This kind of phenomenon has also been reported by other researchers (Hagelstein et al. 1997, Fatsis et al. 1997 and Reunanen 2001). Turunen-Saaresti et al. (2002) have conducted a time-accurate simulation for the centrifugal compressor and noticed a two wave pattern of the static pressure and mass flow at the impeller blade passage during the one revolution. The pinched diffuser increased the pressure level slightly. The highest increment is seen at the design and high flow. This can be seen in the diffuser inlet and outlet.

The circumferential pressure distribution at the diffuser inlet is quite different with the low solidity vaned diffuser than with the vaneless diffuser. Lower values of the static pressure are seen at the circumferential angles $270°$ and $360°$. The steeper the decrement of these values, the lower is the low rate. However, the static pressure values at the circumferential angles $90°$ and $180°$ are almost constant. The lower values at the circumferential angles $270°$ and $360°$ might be due to the proximity of the diffuser vanes. The circumferential variation of the static pressure at the diffuser outlet is vanished with the low solidity vaned diffuser at the low flow. This might be due to the fact that the low flow operation point is at a higher volume flow with the LSVD than with the vaneless diffuser. On the other hand, the circumferential variation is slightly larger with the LSVD than with the vaneless diffuser at the design and high flow.

Figure 41 shows the radial distribution of the static pressure in the diffuser

at the circumferential angle $180°$. The effect of the pinched diffuser is seen as a higher static pressure level. The static pressure rise along the radius ratio is more rapid with the LSVD than with the vaneless diffusers. Also a higher static pressure level at the low and design flow is seen. Most of the static pressure rise at the low solidity vaned diffuser is achieved at the radius ratios between the diffuser inlet and the trailing edge of the low solidity vanes at the design and low flow. The static pressure rise is small at the vaneless space after vanes. The static pressure slightly decreases at the high flow after the leading edge of the vanes but recovers after the vanes. This indicates that the flow is detached at the cascade at the high flow.

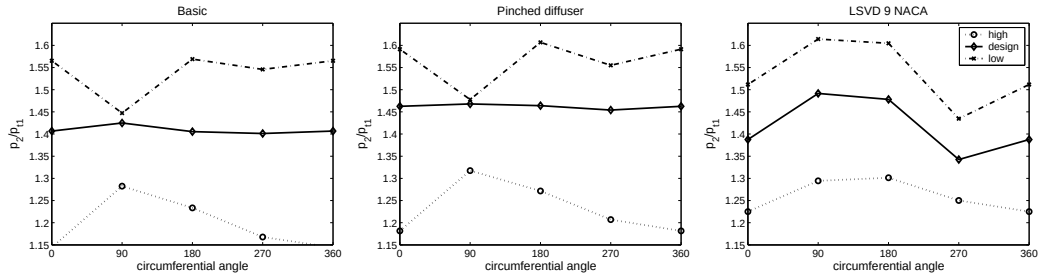

Figure 39: Static pressure distribution at the diffuser inlet $r/r_2 = 1.036$ at low, design and high flow.

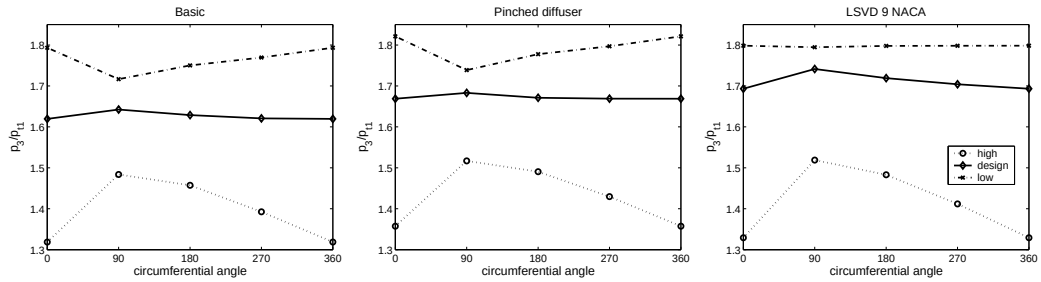

Figure 40: Static pressure distribution at the diffuser outlet $r/r_3 = 1.67$ at low, design and high flow.

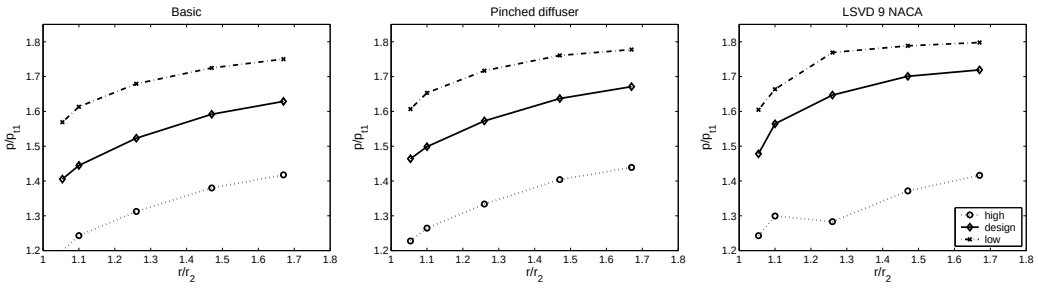

Figure 41: Static pressure distribution as a function of radius ratio at low, design and high flow.

6.4 Kiel- and Cobra-probe measurements in the diffusers

A three-hole Cobra-probe and Kiel-probes were used to obtain information about the flow entering and leaving the diffuser. The Cobra-probe was used to obtain the flow angle of the flow. Flow angle measurements were done only at the circumferential angle $194°$ and it was assumed to be constant over the circumference. However, this assumption was not correct because the flow angle changed over the circumference especially at the off-design conditions. The angle $194°$ was chosen because it represents best the overall condition over the circumference. Only one circumferential angle was measured because it would be very time consuming to make measurements at different circumferential angles using one cobra-probe.

The Kiel-probes were used to obtain total pressure and total temperature traverses across the diffuser at the inlet and the outlet.

The flow angles at the diffuser inlet with different geometries are shown in figure 42. The flow angle distribution at the diffuser inlet is more radial near the hub and more tangential near the shroud. This is due to secondary flow of the impeller blade passage. This phenomenon is stronger at the high flow. There is a reversed flow at the shroud with unpinched diffuser at the design flow. The flow angle turns to radial direction near the shroud with the pinched diffuser. The flow angle does not change near the hub. A reversed flow is not seen with the pinched diffuser. The low solidity vaned diffuser turns the flow angle to the radial at the low flow. At the design flow the change in the flow angle is similar with the LSVD and with the pinched diffuser. The flow angle is more tangential at the high flow with the low solidity vaned diffuser than with the vaneless diffuser. There is a reversed flow at the shroud at the high flow with the LSVD.

The flow angles at the diffuser outlet with different geometries are shown in figure 43. The flow angle across the span is more homogenous at the diffuser outlet than at the inlet, and the difference between the hub and the shroud has

decreased. The pinched diffuser turns the flow angle more radial near the shroud at the diffuser inlet, which is also seen at the diffuser outlet. The low solidity vaned diffuser decreased the difference in the flow angle between the hub and the shroud at the low and design flow. The flow is more radial at the low flow with the LSVD compared to the vaneless diffuser. The flow is more tangential near the hub and more radial near the shroud with the LSVD compared to the vaneless diffusers at the design and high flow. The reversed flow seen in the inlet at the shroud has disappeared in the outlet and the flow is fairly radial with the LSVD. On the other hand, the radial flow seen at the hub at the diffuser inlet has turned to tangential direction.

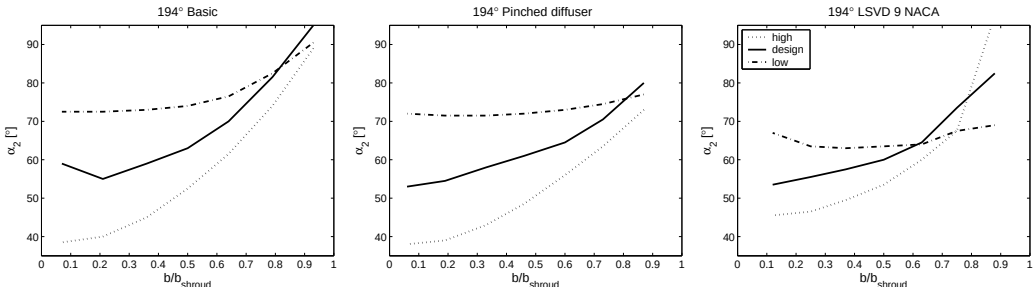

Figure 42: Flow angle distributions in the diffuser inlet at circumferential angle 194°.

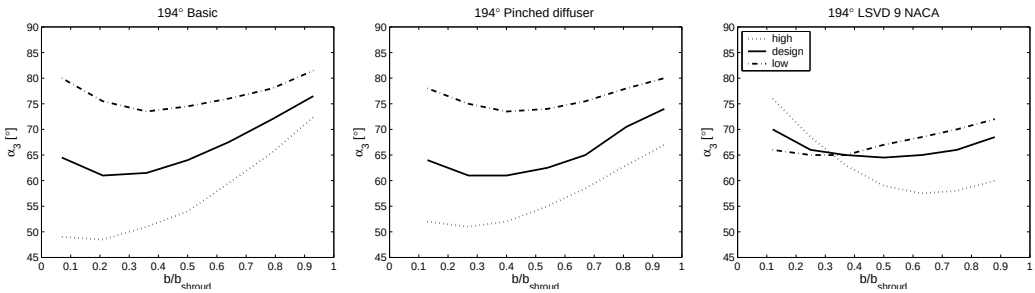

Figure 43: Flow angle distributions in the diffuser outlet at circumferential angle 194°.

The total pressure traverses at different circumferential angles and different geometries at the diffuser inlet are shown in figures 44, 45, 46 and 47. The pressures were not measured very close to the walls because of the size of the probe. The total pressure is lower near the shroud. The lower total pressure area near the shroud increases when the flow is increased. This is seen at all the measured circumferential angles and geometries. This kind of lower total pressure is not seen

at the hub, which indicates that the boundary layer is thinner there at the design and high flow. At the low flow a lower total pressure near the hub is also seen. The lower total pressure level at the low flow is seen at the circumferential angle $104°$. This is due to the observed lower static pressure (see figure 39).

The pinched diffuser decreased the lower total pressure area and increased the total pressure level near the shroud at the design and high flow. At the low flow the pinched diffuser increased the lower total pressure area near the shroud and increased the total pressure near the hub. The total pressure was also slightly higher with the pinched diffuser than with the unpinched diffuser.

The low solidity vaned diffuser increased the total pressure compared to the vaneless diffuser. The total pressure was mainly increased near the hub. The lower total pressure area near the hub at the low flow was steeper with the LSVD than with the vaneless diffuser. However, this phenomenon was not seen at the circumferential angle $14°$.

Total pressure traverses were mass flow averaged across the diffuser width to achieve one value per circumferential angle. The circumferential distribution of the total pressure at the diffuser inlet is shown in figure 48. The circumferential trend of the total pressure is similar with all geometries. The total pressure decreases along the circumference at the high flow and decreases slightly at the design flow. The lower value of the total pressure is seen at the circumferential angle $104°$ at the low flow. This kind of behaviour of the total pressure has also been noticed by e.g. Hagelstein et al. (2000) at the diffuser outlet. They explain this phenomena to be due to the static pressure perturbation caused by the volute tongue (also seen in the present measurements figure 39). The low static pressure in the beginning of the volute is transmitted to the impeller where it affects to the total pressure. This low total pressure then travels through the diffuser. Low static pressure at the diffuser outlet at the circumferential angle $90°$ corresponding to the beginning of the volute was also seen in the present measurements (see figure 40). Therefore a low total pressure is seen at the circumferential angle $104°$ at the diffuser inlet and at the circumferential angle $194°$ at the diffuser outlet (see figure 53). The effect of the pinch is minor at the low and high flow but it slightly smooths the circumferential total pressure at the design flow. The LSVD decreases the circumferential variation of the total pressure at the low and high flow but does not eliminate it. The lower values of the static pressure appear at the circumferential angles $270°$ and $360°$ with the LSVD (see figure 39). In the total pressure lower values are not seen. This indicates that either there is higher velocity in this area or the static pressure values are erroneous.

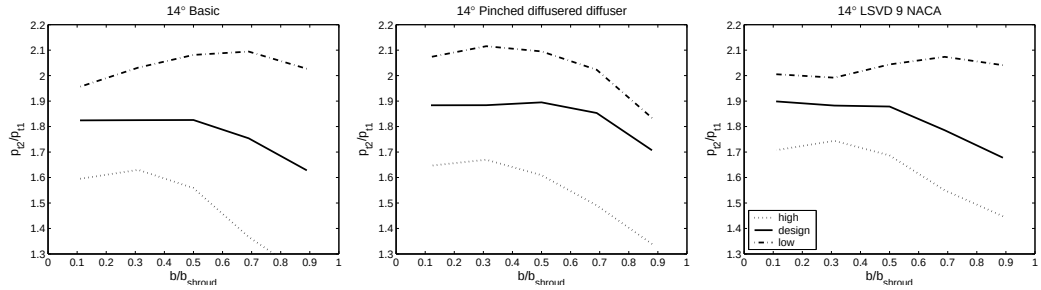

Figure 44: Total pressure traverses across the diffuser inlet at low, design and high flow at circumferential angle $14°$.

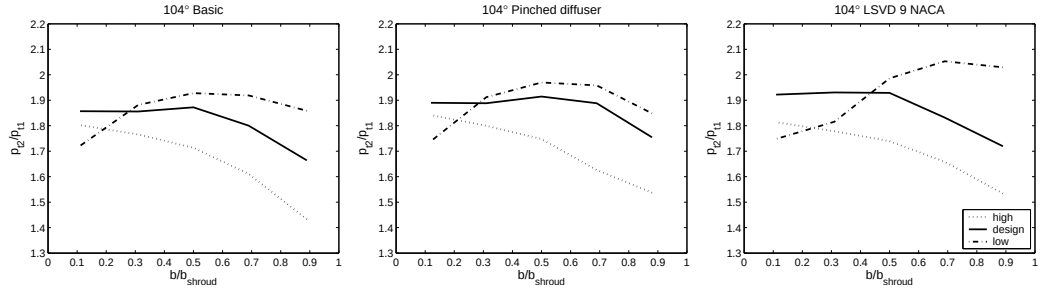

Figure 45: Total pressure traverses across the diffuser inlet at low, design and high flow at circumferential angle $104°$.

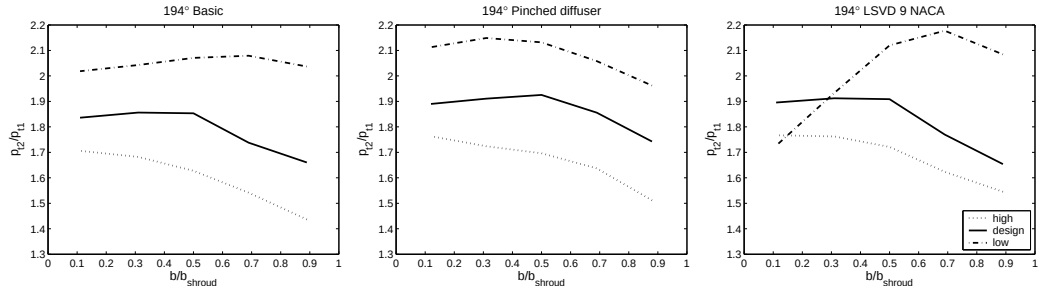

Figure 46: Total pressure traverses across the diffuser inlet at low, design and high flow at circumferential angle $194°$.

The total pressure traverses at different circumferential angles and different geometries at the diffuser outlet are shown in figures 49, 50, 51 and 52. The total pressure distribution is flatter at the outlet than at the inlet. The lower total pressure area near the hub at the low flow in the diffuser inlet is not seen at the

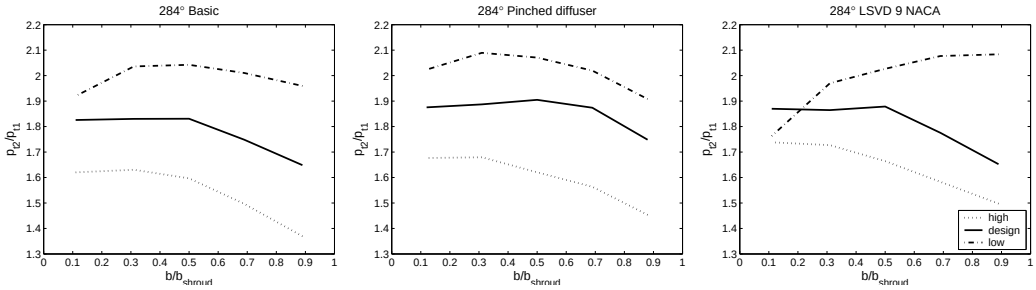

Figure 47: Total pressure traverses across the diffuser inlet at low, design and high flow at circumferential angle $284°$.

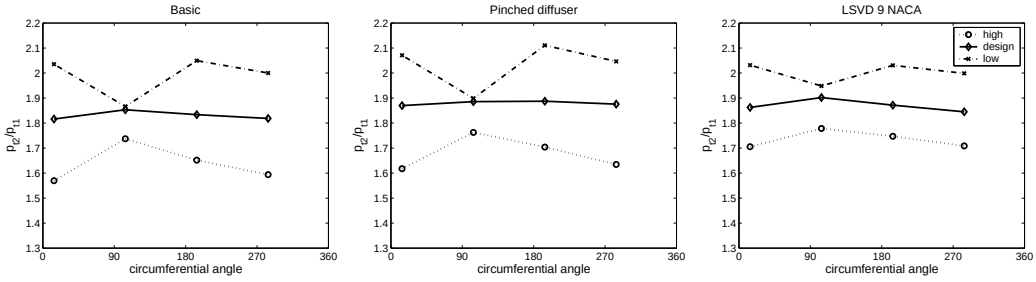

Figure 48: Circumferential distribution of the total pressure in diffuser inlet at low, design and high flow.

diffuser outlet. The total pressure is lower near the walls, which is typical. The pinched diffuser increases the total pressure level, which is also seen at the diffuser inlet. With the LSVD the total pressure is higher at the shroud than at the hub at the high flow. Also the flow angle is more radial at the shroud at the diffuser outlet with the LSVD. This indicates that at the high flow the more radial flow at the diffuser inlet near the hub (see figure 42) has detached the flow near the leading edge of the vanes and blocked the flow, and the flow was forced to move to the shroud. Therefore the higher total pressure and the more radial flow angle are observed at the diffuser outlet. The total pressure is also lower at the low flow with the LSVD than with the vaneless diffuser.

The circumferential distribution of the total pressure at the diffuser outlet is shown in figure 53. The total pressure decreases along the circumference at the high flow and is almost constant at the design flow with the vaneless diffusers. The lower total pressure value seen at the diffuser inlet at the circumferential angle $104°$ is seen at the diffuser outlet at the circumferential angle $194°$ at the low flow. This kind of behaviour was expected. This lower total pressure is almost

attenuated with the low solidity vaned diffuser. The total pressure also decreases along the circumference with the LSVD, and the highest value of the total pressure is not seen at the beginning of the volute but is seen at the circumferential angle $194°$.

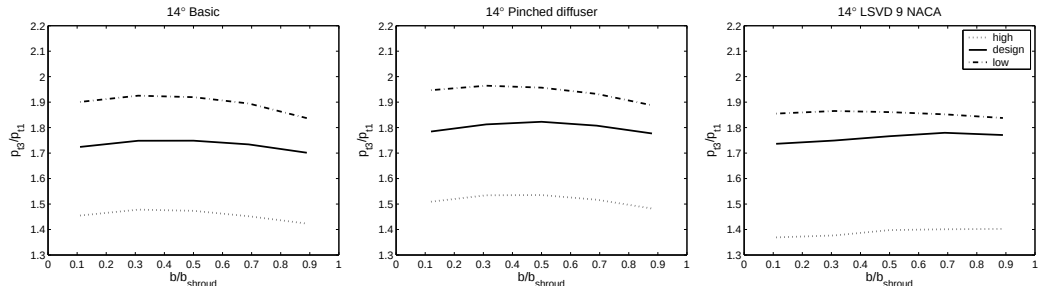

Figure 49: Total pressure traverses across the diffuser outlet at low, design and high flow at circumferential angle $14°$.

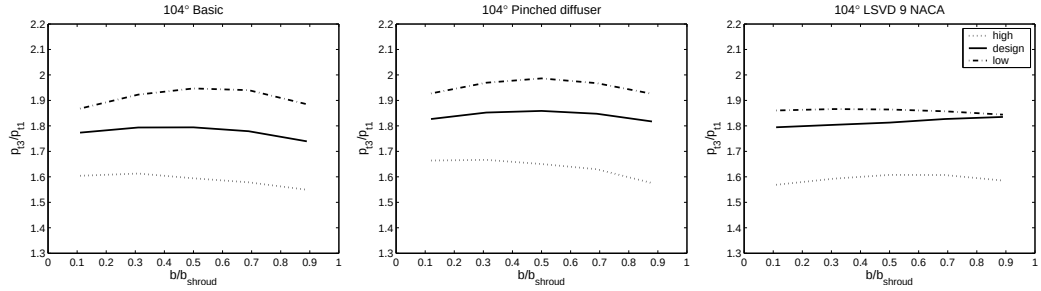

Figure 50: Total pressure traverses across the diffuser outlet at low, design and high flow at circumferential angle $104°$.

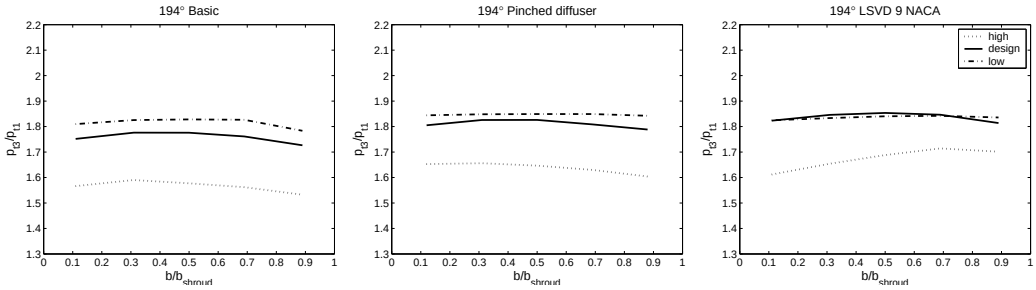

Figure 51: Total pressure traverses across the diffuser outlet at low, design and high flow at circumferential angle $194°$.

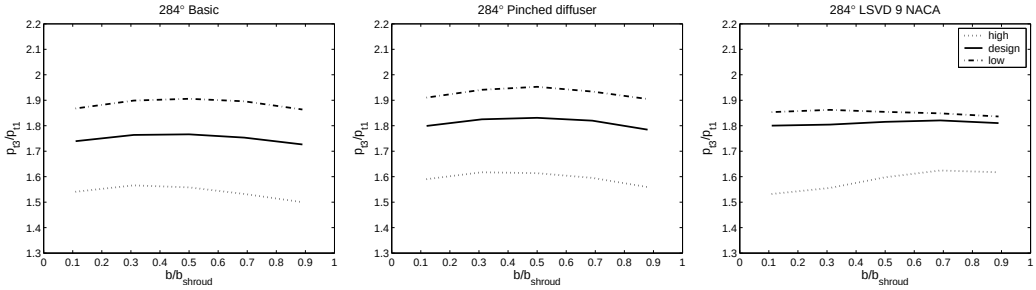

Figure 52: Total pressure traverses across the diffuser outlet at low, design and high flow at circumferential angle $284°$.

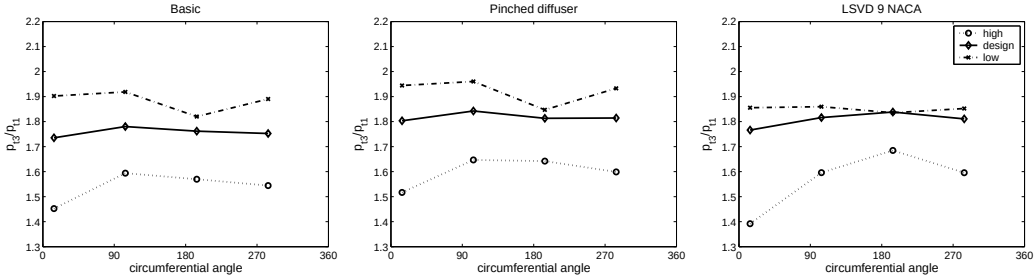

Figure 53: Circumferential distribution of the total pressure in the diffuser outlet at low, design and high flow.

Figures 54, 55, 56 and 57 show the spanwise total temperature variation at the diffuser inlet. The total temperature is higher near the shroud than near the hub. The spanwise variation of the total temperature is smallest at the low flow. The effect of the pinch and the LSVD is minor. On the other hand, the total pressure

distribution shows that the total pressure is lower at the shroud. This indicates that the efficiency is lower near the shroud than near the hub.

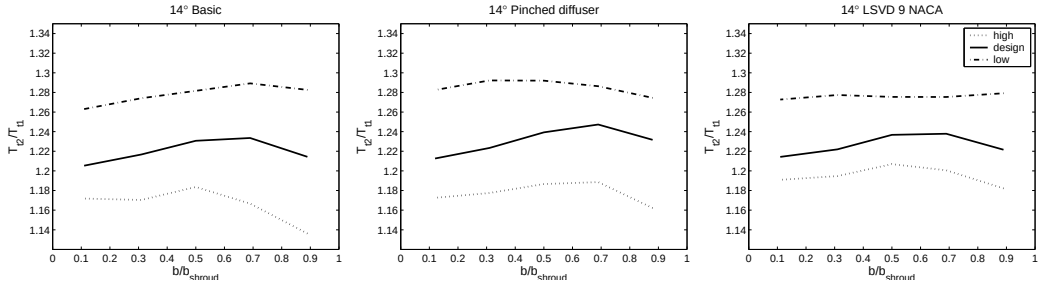

Figure 54: Spanwise total temperature distribution in the diffuser inlet at low, design and high flow at circumferential angle $14°$.

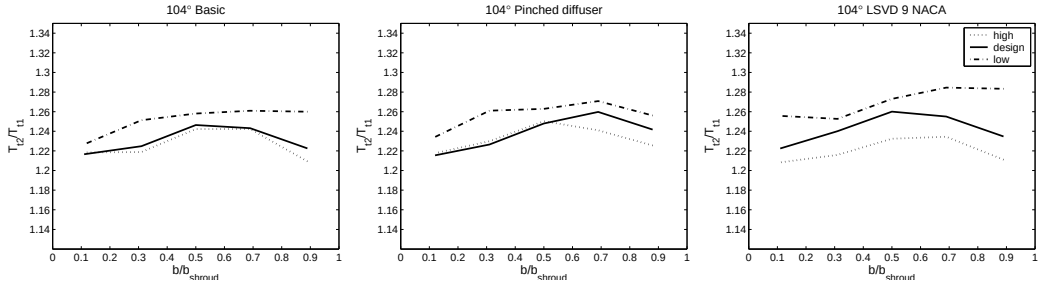

Figure 55: Spanwise total temperature distribution in the diffuser inlet at low, design and high flow at circumferential angle $104°$.

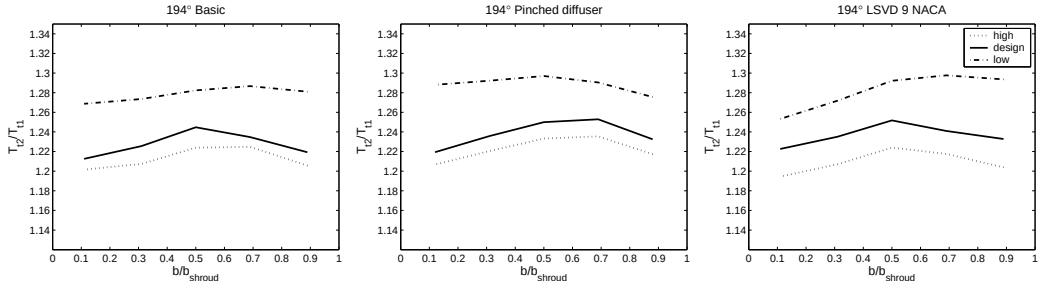

Figure 56: Spanwise total temperature distribution in the diffuser inlet at low, design and high flow at circumferential angle $194°$.

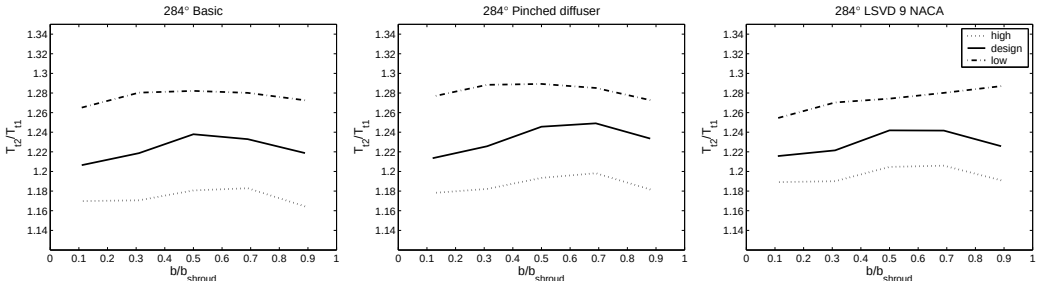

Figure 57: Spanwise total temperature distribution in the diffuser inlet at low, design and high flow at circumferential angle $284°$.

The circumferential variation of the total temperature at the diffuser inlet is shown in figure 58. The same kind of behaviour is seen as it was in the total pressure. The circumferential total temperature slightly decreases at the high flow and is constant at the design flow. At the low flow lower total temperature value is seen at the circumferential angle $104°$.

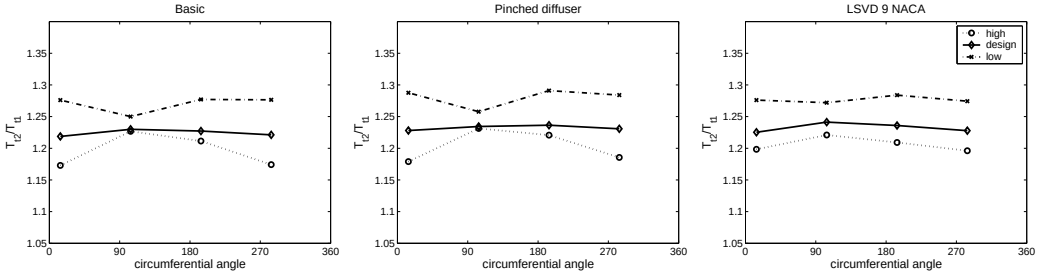

Figure 58: Circumferential total temperature distribution at the diffuser inlet at the low, design and high flow.

Figures 59, 60, 61 and 62 show a spanwise total temperature variation at the diffuser outlet. There is no large variation in the spanwise total temperature distribution. With the LSVD it can be seen that the total temperature is quite high at the high flow, even higher than at the design flow. This kind of behaviour is not seen at the total pressure, which indicates that the efficiency of the diffuser is not good.

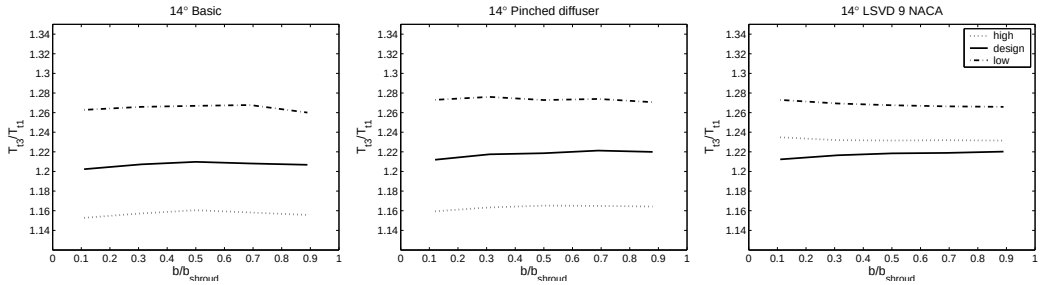

Figure 59: Spanwise total temperature distribution in the diffuser outlet at low, design and high flow at circumferential angle $14°$.

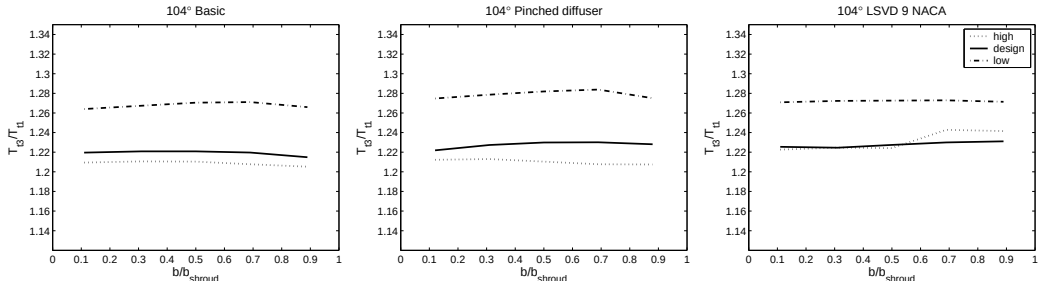

Figure 60: Spanwise total temperature distribution in the diffuser outlet at low, design and high flow at circumferential angle $104°$.

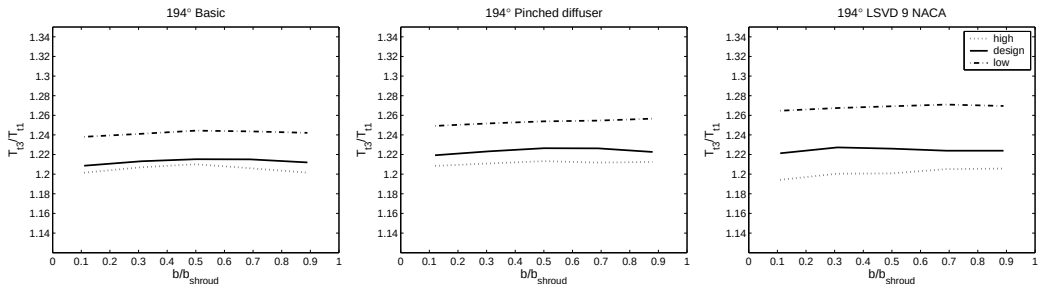

Figure 61: Spanwise total temperature distribution in the diffuser outlet at low, design and high flow at circumferential angle $194°$.

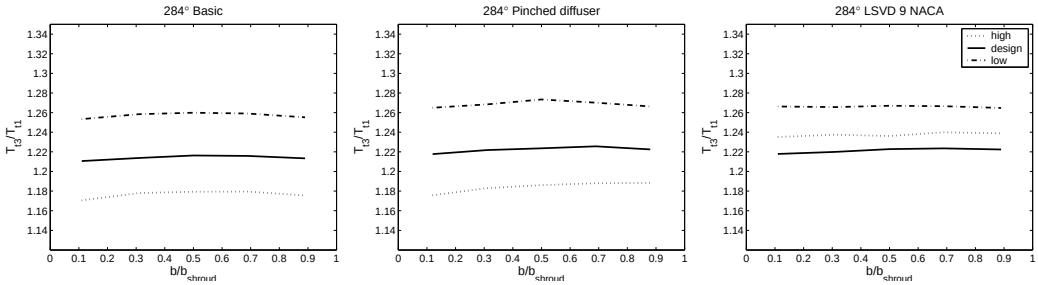

Figure 62: Spanwise total temperature distribution in the diffuser outlet at low, design and high flow at circumferential angle $284°$.

The circumferential variation of the total temperature at the diffuser outlet is shown in figure 63. The total temperature trend is similar to the one at the total pressure. The circumferential total temperature is constant at the design flow and at the high flow, and slightly smaller value is seen at the circumferential angle $194°$ at the low flow. Higher total temperature values are seen at the high flow with the LSVD.

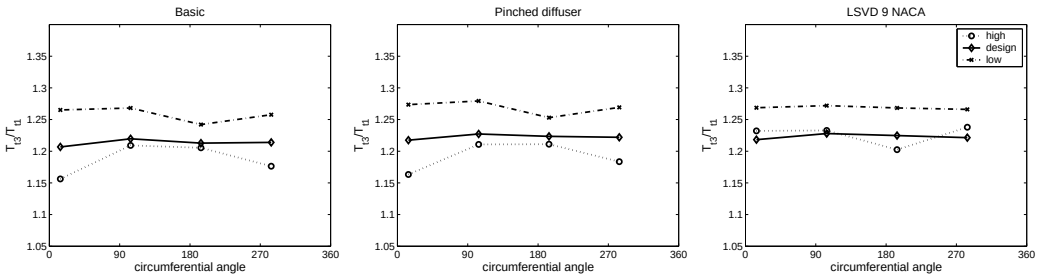

Figure 63: Circumferential total temperature distribution at the diffuser inlet at low, design and high flow.

6.5 Overall performance of the diffusers

The overall performance of the diffusers were evaluated using the static pressure recovery coefficient and the total pressure loss coefficient (see equations 34 and 35). These coefficients were calculated for the diffuser, volute and diffuser-volute combination. The total pressures p_{t2} and p_{t3} were calculated at the Kiel-probe measurements. First the mass flow weighted averaging was done for the spanwise direction to achieve one pressure value at each circumference and then these average pressures were averaged using the mass flow weighting in the circumferential

direction. The static pressures p_2 and p_3 were taken from the static pressure measurements. The static pressures were also averaged using the mass flow weighting. There is an error in the weighting because the mass flows used in the averaging were calculated in each circumferential angle using measured flow angle values at the circumferential angle $194°$. However, this approximation was done for every geometry, and so the results are comparable with each other.

The total pressure loss coefficients as a function of the volume flow are shown in figure 64 and the static pressure recovery coefficient in figure 65. It can be seen that the diffuser has a minimum total pressure loss coefficient and a maximum static pressure recovery coefficient at the design flow. With the pinched diffuser slightly lower values of the total pressure loss coefficient at the design and high flow can be seen than with the unpinched diffuser. Also the total pressure loss coefficient is almost the same at the design flow and at the high flow with the pinched diffuser. The values are almost same at the low flow with the unpinched and pinched diffuser. On the other hand, the static pressure rise coefficient is slightly higher with the unpinched diffuser than with the pinched diffuser. The total pressure loss coefficient is higher at the low and high flow with the LSVD. This is obvious because at the off-design condition incidence is large and losses occur. However, the LSVD has a higher static pressure recovery coefficient at the low flow than the vaneless diffusers. Therefore it can be concluded that at the low flow the LSVD produces a fairly good pressure rise but the losses are high. At the design flow the performance of the LSVD is better than with the vaneless diffusers.

The volute also has a minimum total pressure loss coefficient and a maximum static pressure recovery coefficient at the design flow with the vaneless diffusers. The larger value of the total pressure loss coefficient and the lower value of the static pressure recovery coefficient at the high flow can be explained due to the more radial flow at the diffuser inlet and therefore a higher swirl in the volute. The slightly worse coefficients at the low flow might be due to exit cone according to Reunanen (2001). On the other hand, the volute has a minimum total pressure loss coefficient and a maximum static pressure recovery coefficient with the LSVD at the low flow. This might be due to more radial flow at the diffuser outlet and more swirling flow in the volute, and therefore the exit cone does not have extra losses with the LSVD. The pinched diffuser increases the total pressure loss coefficient and decreases the static pressure recovery coefficient of the volute due to slightly more radial flow at the diffuser outlet at the low and design flow. At the high flow the volute has lower total pressure loss and a higher static pressure rise coefficient with the pinched diffuser than with the unpinched diffuser. The flow angle at the diffuser outlet with the pinched diffuser was slightly more tangential near the hub and slightly more radial near the shroud than with the unpinched diffuser. Therefore there might be less swirling flow in the volute with the pinched diffuser

that with the unpinched diffuser. The LSVD has the same effect on the total pressure loss and the static pressure rise coefficients of the volute as the pinched diffuser. Also the reasons are the same.

The diffuser-volute combination has a minimum total pressure loss coefficient and a maximum static pressure recovery coefficient at the design flow with all geometries. The poor performance of the LSVD at the low flow is compensated by the fairly good performance of the volute. However, the LSVD has worse performance at the high flow, which is also seen at the efficiency and probe measurements. The LSVD has the best performance at the design flow. The pinched diffuser does not have a better performance than the unpinched at the low and at the design flow. however, the efficiency measurements indicate that the pinched diffuser has a better efficiency also at the design flow. Therefore the efficiency increment has to be due to the impeller. The pinched diffuser has a better performance of the diffuser-volute combination at the high flow.

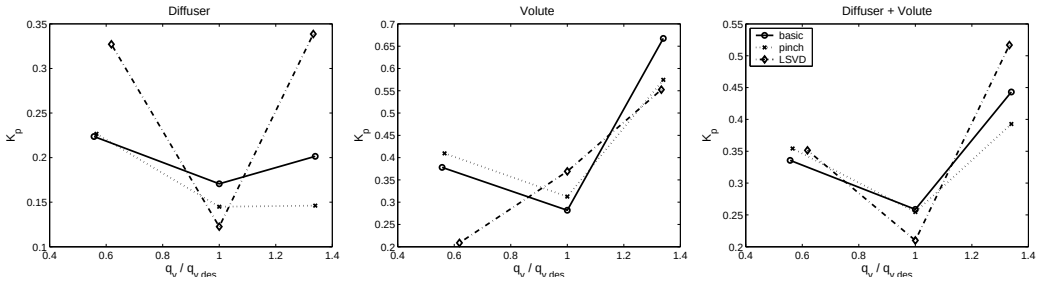

Figure 64: Total pressure loss coefficient as a function of volume flow with different geometries.

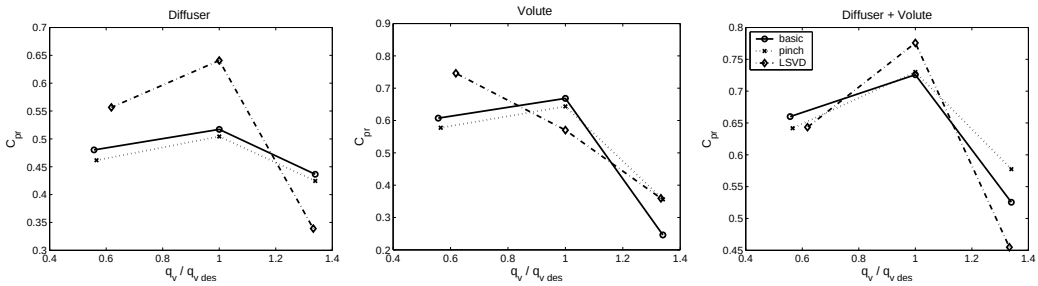

Figure 65: Static pressure recovery coefficient as a function of volume flow with different geometries.

6.6 Unsteady pressure field in vaneless diffuser

Unsteady pressure was measured in another compressor described in chapter 5.1. The measured unsteady pressure spectra at the diffuser inlet are presented in figure 66. The results of different operation points and different circumferential angles are shown. There is small variation of the pressure at the blade passing frequency (about 5050 Hz) at every circumferential angle at the operation point near the surge. The amplitude of the pressure variation is about 200 Pa. At the circumferential angle $168°$ and $348°$ there are also pressure variations at the frequency of every second blade (about 2525 Hz). The amplitude of the pressure variation is larger at the circumferential angle $168°$ than at the circumferential angle $348°$.

At the design operation point the amplitude of the pressure variations are largest at the frequency of every second blade. The amplitude is a little bit larger at the circumferential angle $168°$ than at the other circumferential angles. No clear pressure variation is seen at the blade passing frequency.

There is a larger amplitude of the pressure variations at the circumferential angle $168°$ at the operation point near the choke . The frequencies of the variations are the blade passing frequency and the frequency of every second blade. The larger pressure variation is also seen at the circumferential angle $348°$ and at the blade passing frequency. It can also be noticed that there are smaller pressure fluctuations at the multiplex frequencies of the rotational speed at every operation point. These fluctuations get larger when the flow through the compressor is increased (see figure 66).

The measured pressure spectra at the diffuser outlet are presented in figure 67. The results of different operation points and different circumferential angles are shown. The largest amplitude of the pressure variation is seen at the circumferential angle $348°$ at the operation point near the surge. However, the largest amplitude of the pressure variation at the diffuser inlet is seen at the circumferential angle $168°$ (see figure 66). The amplitude of pressure variation at the blade passing frequency at the diffuser outlet is not large. On the other hand, pressure variations at the blade passing frequency are visible at the diffuser inlet.

The largest amplitude in the pressure variation is seen at the frequency of every second blade (see figure 67) at the design operation point. This is also seen at the diffuser inlet, but the amplitude is larger.

At the operation point near the choke the largest amplitude of the pressure variation is seen at the frequency of every second blade and at the circumferential angle $168°$. This is also seen at the diffuser inlet.

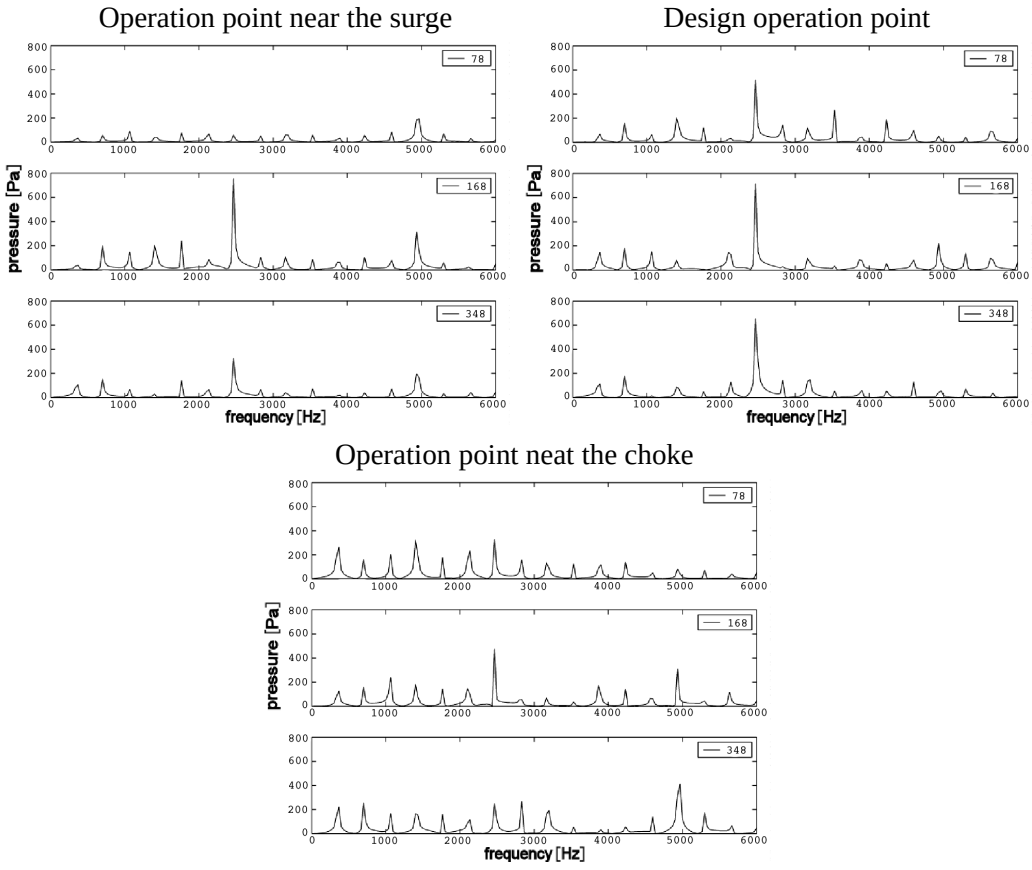

Figure 66: Measured pressure spectra at different circumferential angles in the diffuser inlet.

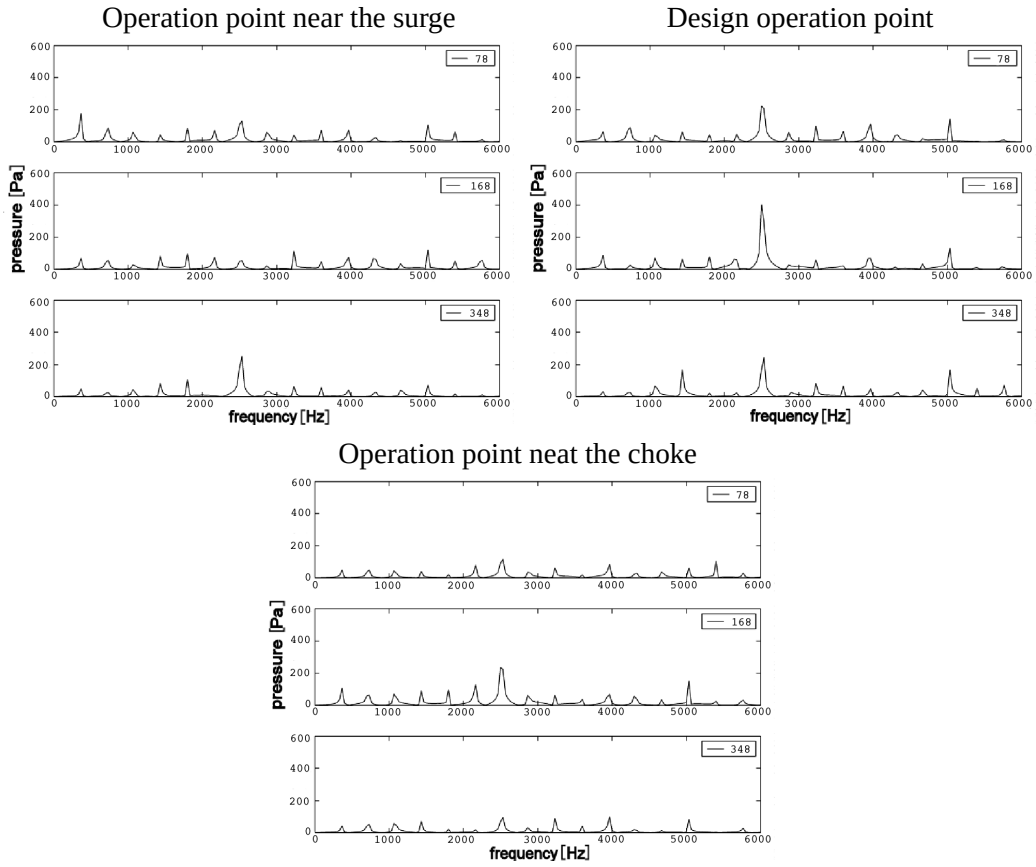

Figure 67: Measured pressure spectra at different circumferential angles in the diffuser outlet.

6.7 Concluding remarks

Three different diffuser geometries were analyzed experimentally. The flow entering the diffuser was measured using a three-hole Cobra-probe, Kiel-probes and static pressure taps. Also the temperature was measured by using thermocouples mounted on the Kiel-probes. These measurements were also conducted at the diffuser outlet. The overall performance of the compressor was analyzed.

The pinched diffuser expanded the area of good efficiency. The beneficial effect of the pinch was mostly seen at the high volume flow and lower speeds when the flow in the diffuser was most radial. The low solidity vaned diffuser increased the efficiency of the compressor at the intermediate flow at all rotational speeds. The compressor flow range was slightly narrowed at the low flow with the low solidity vaned diffuser. It was also noticed that the LSVD had a good performance over large variation of the incidence angle but the very large positive

and negative incidence dropped the efficiency.

Non-uniform circumferential static pressure was observed at the off-design conditions. The low solidity vaned diffuser was noticed to decrease this phenomenon at the low flow. The pinched diffuser increased the static pressure level at the high flow. There was a more rapid static pressure rise along the radius with the low solidity vaned diffuser than with the vaneless diffusers.

A more radial flow was observed at the diffuser with the pinched diffuser than with the unpinched diffuser. The largest change was seen at the shroud. The low solidity vaned diffuser also turned the flow more radial. On the other hand, the flow angle distribution was quite different with the LSVD, especially at the diffuser outlet.

There was lower total pressure near the walls of the diffuser. A larger low total pressure area near the hub was seen at the low flow and near the shroud at the high flow at the diffuser inlet. The spanwise variation of the total pressure decreased at the diffuser outlet compared to the diffuser inlet. The pinched diffuser slightly decreased the lower total pressure area near the shroud wall. The spanwise total pressure was also similar in the low solidity vaned diffuser. Thus, the lower total pressure value was steeper near the hub at the low flow.

The spanwise distribution of the total temperature was smooth and no large variation between different geometries was observed.

A smaller value of the total pressure at the circumferential angle 104° was seen in the diffuser inlet at the low flow. This kind of behaviour was also seen with the pinched diffuser. The LSVD slightly diminished this phenomenon. A smaller value of the total pressure was seen at the circumferential angle 194° in the diffuser outlet at the low flow.

In order to evaluate the performance of the diffusers, the total pressure loss and the static pressure rise coefficients were calculated. These coefficient were also calculated for the volute and for the volute-diffuser combination to evaluate the interaction of these parts. The pinched diffuser had slightly lower values of the total pressure loss coefficient at the design and high flows than the unpinched diffuser. The values were almost the same at the low flow. The total pressure loss coefficient was higher at the low and high flow with the LSVD. However, the LSVD had a higher static pressure recovery coefficient at the low flow than the vaneless diffusers. Therefore can it be concluded that at the low flow the LSVD produced a fairly good pressure rise, but the losses were high. The volute also had a minimum total pressure loss coefficient and a maximum static pressure recovery coefficient at the design flow with the vaneless diffusers. The larger value of the total pressure loss coefficient and the lower value of the static pressure recovery coefficient at the high flow can be explained by the more radial flow at the diffuser inlet causing a higher swirl in the volute. The pinched diffuser increased the total pressure loss coefficient and decreases the static pressure recovery coefficient due

to the slightly more radial flow at the diffuser outlet. The LSVD had the same effect at the design and high flow.

Unsteady static pressure was measured at the diffuser inlet and outlet at three different circumferential angles. It can be concluded that most of the pressure variations lay at the passing frequency of every second blade. The pressure variations did not vanish in the diffuser and were visible at the diffuser outlet. However, the amplitude of the pressure variations decreased in the diffuser. It can also be concluded that the measured pressure variations were largest in the design operation point.

7 Conclusions and recommendations

The flow field in a diffuser of a centrifugal compressor is studied experimentally and numerically. Seven different vaneless diffuser geometries and five different low solidity vaned diffuser geometries were analyzed numerically. Pinches made to the hub or to the shroud or both walls were analyzed. The pinch was 5% and 10% of the height of the unpinched diffuser. The effects of the vane shape and the number of vanes of the LSVD were analyzed. Also the whole compressor was modelled with the vaneless diffuser and a time-accurate numerical simulation was conducted in order to analyze the unsteady phenomena in the diffuser. Three different diffuser geometries were analyzed experimentally. The flow entering the diffuser was measured using a three-hole Cobra-probe, Kiel-probes and static pressure taps. Also the temperature was measured by using thermocouples mounted on the Kiel-probes. These measurements were also conducted at the diffuser outlet. The overall performance of the compressor was measured.

Several studies concerning the design and construction of different kinds of diffusers can be found in the literature. It is a known fact that the pinch is beneficial to the performance of the compressor. However, detailed analysis concerning the pinch is very scarce in the literature. In this study the effect of the pinch is handled by conducting CFD simulations and measurements with different diffuser configurations. Also studies concerning an unsteady flow field in a vaneless diffuser can be found in constrained extent in literature. In addition, the numerical study is comprehensive because the complete compressor is modelled and the time-accurate numerical analysis has been made. Obtained numerical results are then confirmed with the measured ones.

The numerical results showed that the pinch made to the hub and to the shroud wall was most beneficial to the operation of the compressor, and the pinch made to the hub wall was better than the pinch made to the shroud wall. The better efficiency of the compressor was also seen in the measurements with the pinched diffuser. The largest increment obtained in the isentropic efficiency was 2% of the design isentropic efficiency of the original geometry. The low solidity vaned diffuser with the circular arc vanes and NACA thickness distribution achieved better efficiency than the LSVD with the flatplate vanes or the LSVD with the circular arc chamber line and constant thickness distribution according to the numerical results. The experimental results showed that the LSVD increased the efficiency of the compressor, but also slightly decreased the operation range of the compressor. This was expected according to the literature survey. The maximum isentropic efficiency increment was 3% of the design isentropic efficiency of the original geometry.

The total pressure loss and the static pressure rise coefficients were used to analyze the operation of the diffusers. The measured total pressure loss coefficient

was highest at the low flow, lowest at the design flow and slightly higher at the high flow than at the design flow. The difference between the high flow and the design flow was smaller with the pinched diffuser than with the unpinched diffuser. The total pressure loss coefficient from the numerical results was highest at the low flow, moderate at the design flow and lowest at the high flow. There was a difference between the numerical and the measured results mainly because the volute was not modelled in the numerical calculations.

Unsteady phenomena were studied at the vaneless diffuser by measuring unsteady static pressure at the diffuser inlet and outlet, and by conducting time-accurate numerical simulations. The results showed that most of the pressure variations lay at the passing frequency of every second blade. It was also noticed that the pressure variations decreased in the diffuser. These pressure variations were largest at the design operation point. The time-accurate calculations showed quite a good agreement with the measured data especially at the design operation point. The amplitude of the pressure variations was over-predicted in the time-accurate simulation at the high flow.

It can be concluded from the numerical and experimental results that the pinch is beneficial to the performance of the compressor, and the pinch made to both walls was found to be the best configuration. Therefore the pinch is recommended to be utilized whenever a vaneless diffuser is used. The low solidity vaned diffuser also improved the efficiency of the compressor but narrowed the operation range. If a very wide flow range is not the main target, the low solidity vaned diffuser is a very good option to the vaneless diffuser. The effect of the LSVD and the pinch was not studied together, and it is worth studying in the future.

References

Aminemi, N. K., Engeda, A., Hohlweg, W. C., and Direnzi, G. I. (1996). Performance of low solidity and convectional diffuser systems for centrifugal compressors. 96-GT-155. International Gas Turbine and Aeroengine Congress & Exhibition, Birmingham, UK.

Amineni, N. K. and Engeda, A. (1997). Pressure recovery in low solidity vaned diffusers for centrifugal compressors. 97-GT-472. International Gas Turbine & Aeroengine Congress Exhibition Orlando, Florida.

Arnulfi, G. L., Micheli, D., and Pinamonti, P. (1995). Velocity measurements downstream of the impellers in a multistage centrifugal blower. *Journal of Turbomachinery*, 117:593–601.

ASME PTC 10 (1965). *ASME Power Test codes, compressors and exhausters*. The American Society of Mechanical Engineering.

Baldwin, B. and Lomax, H. (1978). Thin layer approximation and algebraic model for separeted turbulence flows. *AIAA Paper 78-257*.

Bonaluti, D., Arnone, A., Hah, C., and Hayami, H. (2002). Development of secondary flow field in a low solidity diffuser in a transonic centrifugal compressor stage. GT-2002-30371. Proceedings of ASME Turbo Expo, Amsterdam, The Netherlands.

Chien, K. (1982). Predictions of channel and boundary-layer flows with a low-Reynolds-number turbulence model. *AIAA Journal*, 20:33–38.

Dean, R. and Senoo, Y. (1960). Rotating wakes in vaneless diffuser. *Journal of Basic Engineering*, 82.

Dibelius, G., Radtke, F., and Ziemann, M. (1984). Experiments on friction, velocity and pressure distributions of rotating disks. pages 117–130. Proceedings of the International Centre for Heat and Mass Transfer.

DIN 1952 (1971). *Durchflußmessung mit genormten Düsen, Blenden und Venturidüsen*. Deutsches Institut für Normung e.V.

Eckardt, D. (1975). Instantaneuos measurements in the jet-wake discharge flow of a centrifugal compressor impeller. *Journal of Engineering for Power*, 97:337–346.

Engeda, A. (1995). Prediction of the effect of the diffuser width on the diffusion process in a radial vaneless diffuser. AD-vol. 49. Computational Fluids Dynamics in Aeropropulsion, ASME.

Engeda, A. (1996). Performance of different diffusers for centrifugal compressors. FED-vol. 238. Fluids Engineering Division Conferense, ASME.

Engeda, A. (1997). Design of a range of low solidity vaned diffusers for centrifugal compressor. 97-WA/PID-4. International Mechanical Engineering Congress & Exposition Dallas, Texas.

Engeda, A. (1998). Desing and investigation of four low solidity vaned diffusers to assess the effect of solidity and vane number. 98-GT-252. International Gas Turbine & Aeroengine Congress & Exhibition, Stockholm, Sweden.

Eynon, P. A. and Whitfield, A. (1997). The effect of low-solidity vaned diffusers on the performance of a turbocharger compressor. *Proc Instn Mech Engrs Part C*, 211:325–339.

Farge, T. Z., Johnson, M. W., and Maksoud, T. M. A. (1989). Tip leakage in a centrifugal impeller. *Journal of Turbomachinery*, 111:244–249.

Fatsis, A., Pierret, S., and Van den Braembussche, R. (1997). Three-dimensional unsteady flow and forces in centrifugal impellers with circumferential distortion of the outlet static pressure. *Journal of Turbomachinery*, 119:94–102.

Hagelstein, D., Hillewaert, K., Van den Braembussche, R. A., Engeda, A., Keiper, R., and Rautenberg, M. (2000). Experimental and numerical investgation of the flow in a centrifugal compressor volute. *Journal of Turbomachinery*, 122:22–31.

Hagelstein, D., Van den Braembussche, R., Keiper, R., and Rautenberg, M. (1997). Experimental investigation of the circumferential static pressure distortion in centrifugal compressor stages. 97-GT-50. ASME Paper.

Hathaway, M. D., Chriss, R. M., Wood, J. R., and Strazisar, A. J. (1993). Experimental and computational investigation of the nasa low-speed centrifugal compressor flow field. *Journal of Turbomachinery*, 115:527–542.

Haupt, U., Rautenberg, M., and Abdel-Hamid, A. N. (1988). Blade excitation by broad-band pressure fluctuations in a centrifugal compressor. *Journal of Turbomachinery*, 110:129–137.

Hayami, H., Senoo, Y., and Utsunomiya, K. (1990). Application of a low-solidity cascade diffuser to transonic centrifugal compressor. *Journal of Turbomachinery*, 112:25–29.

Herrig, L. J., Emery, J. C., and Erwin, J. R. (1958). Systematic two-dimensional cascade test of NACA 65-series compressor blades at low speeds. NACA-TR-1368.

Hillewaert, K. and Van den Braembussche, R. A. (1999). Numerical simulation of impeller-volute interaction in centrifugal compressors. *Journal of Turbomachinery*, 121:603–608.

Hoffren, J. (1992). Time-accurate schemes for a multi-block Navier-Stokes solver. Technical Report Report A-14, Helsinki University of Technology, Laboratory of Aerodynamics.

Hohlweg, W. C., Direnzi, G. L., and Aungier, R. H. (1993). Comparison of convectional and low solidity vaned diffusers. 93-GT-98. International Gas Turbine and Aeroengine Congress and Exposition Cincinnati, Ohio.

ISO 5389 (1992). *Turbocompressors - Performance test code*. International Stardardization Organization.

Jansen, W. (1964). Rotating stall in a radial vaneless diffuser. *Journal of Basic Engineering*, 86:750–758.

Japikse, D. (1986). *Advanced Experimental Techniques in Turbomachinery*. Consepts ETI, Inc.

Japikse, D. and Goebel, J. H. (1979). Turbocharger compressor performance evaluation and critical flow field measurements. *SAE Paper No. 790315*.

Jin, D., Hasemann, H., Haupt, U., and Rautenberg, M. (1994). The flow and rotation characteristics of a centrifugal compressor during surge. 94-GT-154. International Gas Turbine and Aeroengine Congress and Exposition The Hague, The Netherlands.

Justen, F., Ziegler, K. U., and Gallus, H. E. (1999). Experimental investigation of unsteady flow phenomena in a centrifugal compressor vaned diffuser of variable geometry. *Journal of Turbomachinery*, 121:763–771.

Kim, W. J. and Engeda, A. (1997). Comparison of pressure recovery and overall performance of different diffusers for centrifugal compressors. FEDSM97-3029. Fluids Engineering Division Summer Meeting, ASME.

Koumoutsos, A., Tourlidakis, A., and Elder, R. I. (2000). Computational studies of unsteady flows in a centrifugal compressor stage. *Proc Instn Mech Engrs Part A*, 214:611–633.

Krain, H. (1980). Experimental and theoretical investigations on the internal flow in a centrifugal compressor. Proc No. 282-1. AGARD Conference.

Krain, H. (1981). A study on centrifugal impeller and diffuser flow. *Journal of Engineering for Power*, 103:688–697.

Krain, H. (1988). Swirling impeller flow. *Journal of Turbomachinery*, 110:122–128.

Kunz, R. F. and Lakshminarayana, B. (1992). Three-dimensional Navier-Stokes computation of turbomachinery flows using an explicit numerical procedure and a coupled $k-\epsilon$ turbulence model. *Journal of Turbomachinery*, 114:627–642.

Kupferschmied, P., Köppel, P., Roduner, C., and Gyarmathy, G. (2000). On the development and application of the fast-response aerodynamic probe system in turbomachines - part 1: The measurement system. *Journal of Turbomachinery*, 122:505–516.

Larjola, J. (2000). Optimizing compressor design by using high speed turbo compressors. Conference in applied techniques to optimize nutrient removal and aeration efficiency, Helsinki, Finland.

Larjola, J., Backman, J., Esa, H., Pitkänen, H., P.Sallinen, and Honkatukia, J. (2000). Centrifugal compressor design and testing in finnish high speed technology. International Mechanical Engineering Congress & Expo, Orlando, Florida.

Lee, Y.-T., Luo, L., and Bein, T. W. (2001). Direct method for optimization of a centrifugal compressor vaneless diffuser. *Journal of Turbomachinery*, 123:73–80.

Liberti, J.-L. D., Wilmsen, B., and Engeda, A. (1996). The effect of the vaneless diffuser width on the performance of a centrifugal compressor. FED-vol. 237, pages 797–803. Fluids Engineering Division Conference, ASME.

Lombard, C. K., Bardina, J., Venkatapathy, E., and Oliger, J. (1983). Multi-dimensional formulation of CSCM - an upwind flux difference eigenvector split method for compressible Navier-Stokes equations. Paper 83-1895-CP, pages 649–664. 6th AIAA Computational Fluid Dynamics Conference.

Ludtke, K. (1983). Aerodynamic tests on centrifugal process compressors - the influence of the vaneless diffusor shape. *Journal of Engineering for Power*, 105:902–909.

Menter, F. R. (1994). Two-equation eddy-viscosity turbulence models for engineering applications. *AIAA Journal*, 32:1598–1605.

Pinarbasi, A. and Johnson, M. W. (1994). Detailed flow measurements in a centrifugal compressor vaneless diffuser. *Journal of Turbomachinery*, 116:453–461.

Pinarbasi, A. and Johnson, M. W. (1995). Off design reynolds stress tensor measurements in a centrifugal compressor vaneless diffuser. *Journal of Turbomachinery*, 117:602–610.

Rai, M. (1986). A relaxation approach to patched-grid calculations with the Euler equations. *Journal of Computational Physics*, 66:99–131.

Rautaheimo, P., Salminen, E., and Siikonen, T. (1999). Numerical simulation of the flow in the NASA low-speed centrifugal compressor. Technical Report Report No. 119, Helsinki University of Technology, Laboratory of Applied Thermodynamics.

Reunanen, A. (2001). *Experimental and Numerical Analysis of Different Volutes in a Centrifugal Compressor*. PhD thesis, Lappeenranta University of Technology.

Roe, P. L. (1981). Approximate Riemann solvers, parameter vectors and difference schemes. *Journal of Computational Physics*, 43:357–372.

Sallinen, P. (1999). Additional information to report "compressor testing facility", uncertainty calculation. Technical Report Internal Report, Lappeenranta University of Technology, Department of Energy Technology.

Senoo, Y. (1984). Low solidity cascade diffusers for wide flow range centrifugal blowers. Lecture Series 1984-07. von Karman Institute for Fluid Dynamics.

Senoo, Y., Hayami, H., and Ueki, H. (1983). Low solidity tamdem cascade diffusers for wide range centrifugal blowers. 83-GT-3. ASME paper.

Senoo, Y. and Kinoshita, Y. (1977). Influence of inlet flow conditions and geometries of centrifugal vaneless diffusers on critical flow angle for reverse flow. *Journal of Fluids Engineering*, 99:98–103.

Shum, Y. K. P., Tan, C. S., and Cumpsty, N. A. (2000). Impeller-diffuser interaction in centrifugal compressor. 2000-GT-0428. Proceedings of ASME Turbo Expo, Munich, Germany.

Siikonen, T. (1995). An application of Roes flux-difference splitting for the $k - \epsilon$ turbulence model. *International Journal for Numerical Methods in Fluids*, 21:1017–1039.

Siikonen, T., Rautaheimo, P., and Salminen, E. (2001). *Finflo User Guide, Version 3.3*. Helsinki University of Technology, Laboratory of Applied Thermodynamics.

Sorokes, J. M., Borer, J. C., and Koch, J. M. (1998). Investigation of the circumferential static pressure non-uniformity caused by centrifugal compressor discharge volute. 98-GT-326. International Gas Turbine & Aeroengine Congress & Exhibition, Stockholm, Sweden.

Sorokes, J. M. and Koch, J. M. (2000). The influence of low solidity vaned diffusers on the static pressure non-uniformity caused by a centrifugal compressor discharge volute. 2000-GT-0454. Proceedings of ASME Turbo Expo, Munich, Germany.

Sorokes, J. M. and Welch, J. P. (1992). Experimental results on a rotatable low solidity vaned diffuser. 92-GT-19. ASME paper.

Speziale, C., Sarkar, S., and Gantski, T. (1991). Modelling the pressure-strain correlation of turbulence: an invariant dynamical systems approach. *Journal of Fluid Mechanics*, 227:245–272.

Turunen-Saaresti, T. (2001). Radiaalikompressorin spiraalivirtauksen numeerinen mallinnus (in finnish),[numerical simulation of the flow in the volute of the centrifugal compressor]. Master's thesis, Lappeenranta University of Technology, Department of Energy Technology.

Turunen-Saaresti, T., Reunanen, A., and Larjola, J. (2002). Time-accurate simulation of the centrifugal compressor. GT-2002-30382. Proceedings of ASME Turbo Expo, Amsterdam, The Netherlands.

Van den Braembussche, R. A., Frigne, P., and Roustan, M. (1980). Rotating non-uniform flow in radial compressors. Proc No. 282. AGARD Conference.

VDI 2045 (1991). *Durchflußmessung mit Drosselgeräten, Blenden und Düsen für Berondere Anwendugen (Measurement of Fluid Flow with Primary Devices, Oriface Plates and Nozzles for Special Applications)*. Verein Deutscher Ingenieure.

VDI 2045 Part 1 (1993). *Abnahme- und Leistungsversuche an Verdichtern, Versuchsdurchführung und Garantievergleich (Acceptance and Performance Test on Turbo Compressors and Displacement Compressors, Test Procedure and Comparison with Guaranteed Values)*. Verein Deutscher Ingenieure.

VDI 2045 Part 2 (1993). *Abnahme- und Leistungsversuche an Verdichtern, Grundlagen und Beispiele (Acceptance and Performance Test on Turbo Compressors and Displacement Compressors, Theory and examples)*. Verein Deutscher Ingenieure.

Yingkang, Z. and Sjolander, S. (1987). Effects of geometry on the performance of radial vaneless diffuser. *Journal of Turbomachinery*, 109:550–556.

Ziegler, K. U., Gallus, H. E., and Niehuis, R. (2003a). A study on impeller-diffuser interaction: Part i - influence on the performance. *Journal of Turbomachinery*, 125:173–182.

Ziegler, K. U., Gallus, H. E., and Niehuis, R. (2003b). A study on impeller-diffuser interaction: Part ii - detailed flow analysis. *Journal of Turbomachinery*, 125:183–192.